KELVIN-HELMHOLTZ INSTABILITY AND MAGNETIC RECONNECTION AT THE EARTH'S MAGNETOSPHERIC BOUNDARY

A

DISSERTATION

Presented to the Faculty

of the University of Alaska Fairbanks

in Partial Fulfillment of the Requirements

for the Degree of

DOCTOR OF PHILOSOPHY

By

Xuanye Ma, B.S.

Fairbanks, Alaska

December 2012

UMI Number: 3537847

UMI®

Dissertation Publishing

ProQuest®

KELVIN-HELMHOLTZ INSTABILITY AND MAGNETIC RECONNECTION AT THE EARTH'S MAGNETOSPHERIC BOUNDARY

By

Xuanye Ma

RECOMMENDED:

Advisory Committee Chair

Chair, Department of Physics

APPROVED:

Dean, College of Natural Science and Mathematics

Dean of the Graduate School

12/21/12

Date

Abstract

Magnetic reconnection and Kelvin-Helmholtz (KH) instability are the two most important mechanisms for plasma transport across the Earth's magnetospheric boundary layer. Magnetic reconnection is considered as the dominant process for southward interplanetary magnetic field (IMF), and the KH instability is suggested to play an important role for northward IMF.

It is interesting to note that this plasma entry is associated with a dramatic entropy increase, which indicates the existence of strong nonadiabatic heating during the entry process. Observations indicate a plasma entropy increase by two orders of magnitude during the transport from solar wind into the Earth's magnetosphere. Therefore, it is important to examine whether magnetic reconnection can provide sufficient nonadiabatic heating to explain the observed plasma properties and to identify plasma conditions that allow strong nonadiabatic heating. This thesis demonstrates that the ent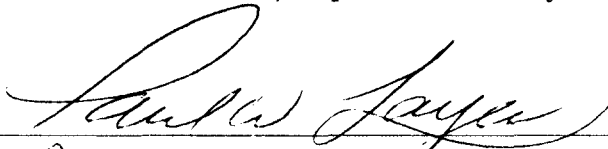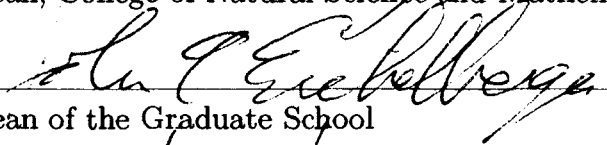ropy can indeed strongly increase during magnetic reconnection provided that the plasma beta, i.e., the ratio of thermal to magnetic energy density is small.

A realistic three-dimensional configuration of the Earth's magnetopause for southward IMF conditions includes large anti-parallels magnetic components with a fast perpendicular shear flow. Thus, it is expected that KH modes and magnetic reconnection operate simultaneously and interact with each other. This thesis provides a systematic study on this interaction between reconnection and KH modes by means of three-dimensional MHD and Hall MHD numerical simulations. It is demonstrated that both reconnection and nonlinear KH waves change the other modes onset condition by changing the width of the transition layer. It is shown that dynamics of the system can be strongly modified by a guide field or Hall physics.

In the presence of plasma flow, magnetic reconnection is also associated with the generation of field-aligned currents (FACs), which play a critical role in the coupling between the magnetosphere and ionosphere. This thesis also examines systematically the generation of FACs. It is demonstrated that such currents are generated either by a guide magnetic field, by shear flow, or by the inclusion of Hall physics already

in two-dimensional magnetic reconnection.

Table of Contents

List of Figures

List of Tables

Acknowledgements

First I would like to thank Professor Antonius Otto, my thesis advisor, for his great intellect, outstanding knowledge in our field and beyond, constant encouragement, advice, support, and extreme patience towards my work, particular in correcting my grammar. I have been extremely fortunate to study space physics under his guidance during the past four years. Besides the thesis project, he also shows me how to systematically approach to a more general question in daily life, which is a very important lesson to me.

My sincere appreciation also goes to Professor David Newman, whose comments improve my thesis. And I believe that he is the best classical electrodynamics teacher I have ever seen. I would also like to thank Professors Dirk Lummerzheim, Chung-Sang Ng, and Hui Zhang for their invaluable comments and suggestions on my thesis. Especially, I would like to thank Professor Hui Zhang for her special method to check English grammar by using google.

I am also very grateful for Professors Huigen Yang, Desheng Han, and Dr. Zejun Hu at Polar Research Institute of China. As a person, who was born in a warm place, I could hardly imagine the life in the Alaska before I came here. Without their encouragements, I might change my decision to study at University of Alaska Fairbanks. My gratitude also extends to Professors Chuxin Chen and Huinan Zheng, who opened the door of Space Physics for me when I was studying at University of Science and Technology of China. And I would also like to thank Professors Katariina Nykyri, Dr. Chih-Ping, Wang for their helpful discussions.

My special thanks go to RJ Stevens, Dr. Eric Adamson and their family, who helped me to get used to the life in the Alaska and taught me all kinds of American culture. I would also like to thank my friends at UAF, Srikamal Soundararajan, Tapas Bhattacharya, Min-Shiu Hsieh, Sun-Hee Lee, Christina Chu, Carl Andersen, Peter Peterson, Julia P Hennig, Wei Dang, Jiaqi Huang, Qingjia Li, Dr. Yuning Fu, Wenyu Gong, and Dr.Yun Wang, for their help during my graduate study.

Finally, I would like to thank my family for their understanding and support.

Chapter 1

Introduction

1.1 Background on Magnetospheric Physics

At a distance of 1.5×10^{11} m (1 AU) from the Earth, the sun, as the biggest power factory in our solar system, releases energy at 3.846×10^{26} W·s^{-1}, which corresponds to 4.3×10^{9} kg · s^{-1} according to the mass–energy equivalence [*Kallenrode*, 2004]. Theoretical models suggest a powerful fusion reactor at the core of the sun operating at a temperature of 1.5×10^{7} K and generating energy through fusion of 5×10^{9} kg·s^{-1} of hydrogen to form helium [*Kivelson and Russell*, 1995]. Above the core are the radiative diffusion region, the convection region, and the atmosphere. The solar atmosphere consists of three layers: the photosphere, the chromosphere, and the corona [*Kivelson and Russell*, 1995]. Due to strong magnetic fields and the large pressure gradient between the corona and interstellar space, the ionized solar plasma and a remnant of the solar magnetic field are driven outward, which generates the solar wind. The first stationary expansion solar wind model was developed by *Parker* [1958]. It takes the solar wind about 4 days [*Kivelson and Russell*, 1995] to travel from the sun to the Earth. The typical solar wind density at 1 AU is several particles per centimeter cubed with a temperature of 1.2×10^{5} K, and its highly supersonic speed is about 450 km·s^{-1} nearly along the radial direction [*Kivelson and Russell*, 1995]. Without the Earth's magnetospheric protection, high energy particles in the solar wind can easily penetrate into the Earth's atmosphere.

The Earth's magnetosphere is a large low density plasma cavity generated by the geomagnetic field and the solar wind plasma [*Otto*, 2010; *Kallenrode*, 2004; *Kivelson and Russell*, 1995]. The geomagnetic field is caused by internal dynamo mechanisms in the outer core of the Earth. Near the Earth's surface, the magnetic field can be well described by a magnetic dipole moment, which is tilted at an angle of 11 degrees with respect to the rotational axis and has a magnetic moment of about 8×10^{15} T · m^{3}. The actual solar wind velocity is superfast at 1 AU, meaning it is faster than the fast mode speed $V_f = \sqrt{c_s^2 + V_A^2}$, where c_s is the ion acoustic speed and

V_A is the Alfvén speed (see Section 1.2). This is the fastest wave velocity with which information can propagate in a large scale plasma. Therefore, a bow shock is formed in the front of the Earth's magnetosphere [Burgess et al., 2012] similar to sonic shocks caused by supersonic jets, and the magnetosheath is the shocked solar wind plasma. The shocked solar wind compresses the dayside portion of the geomagnetic field and generates a tail which is many hundreds of Earth's radii ($R_E = 6.4 \times 10^6$ m) long. Although, most of the shocked solar wind particles are deflected by the geomagnetic field at the magnetopause, which is the actual boundary between the solar wind and the magnetospheric plasma, the magnetopause is not a "plasma proof" shield. The real interaction between the solar wind and magnetosphere is much more complex and important. Just inside of the magnetopause are the cusp and mantle regions. The cusp is the region where dipolar field lines converge, and the mantle region represents a boundary to the magnetotail usually filled with solar wind plasma but with a stretched magnetospheric magnetic field. Further inside is the magnetotail, which is the long tail-like extension of the magnetosphere on the nightside of the magnetosphere. The inner magnetosphere is the region where the magnetic field is dominated by the dipole component, and relative magnetic field changes are small, typically inside of 8 to $10R_E$ radial distance [Otto, 2010]. The transition region between the fully ionized magnetosphere and the neutral atmosphere is the ionosphere.

Figure 1.1 presents the magnetospheric boundary layers and currents. Early models of the magnetosphere consider the magnetopause as an almost impenetrable boundary, which separates the magnetosphere entirely from the magnetosheath by a tangential discontinuity, since the plasma (electron and ion) transport across the magnetic field lines is very slow. In this model the entire geomagnetic field is closed inside the magnetosphere. However, early ionospheric and satellite observation demonstrated that the actual geomagnetic field is not confined to the magnetosphere but threads out into interplanetary space. In fact, the solar wind plasma has access to the Earth's magnetosphere along the open magnetic field at its boundary. This boundary layer is often divided into the low-latitude boundary layer (LLBL), the en-
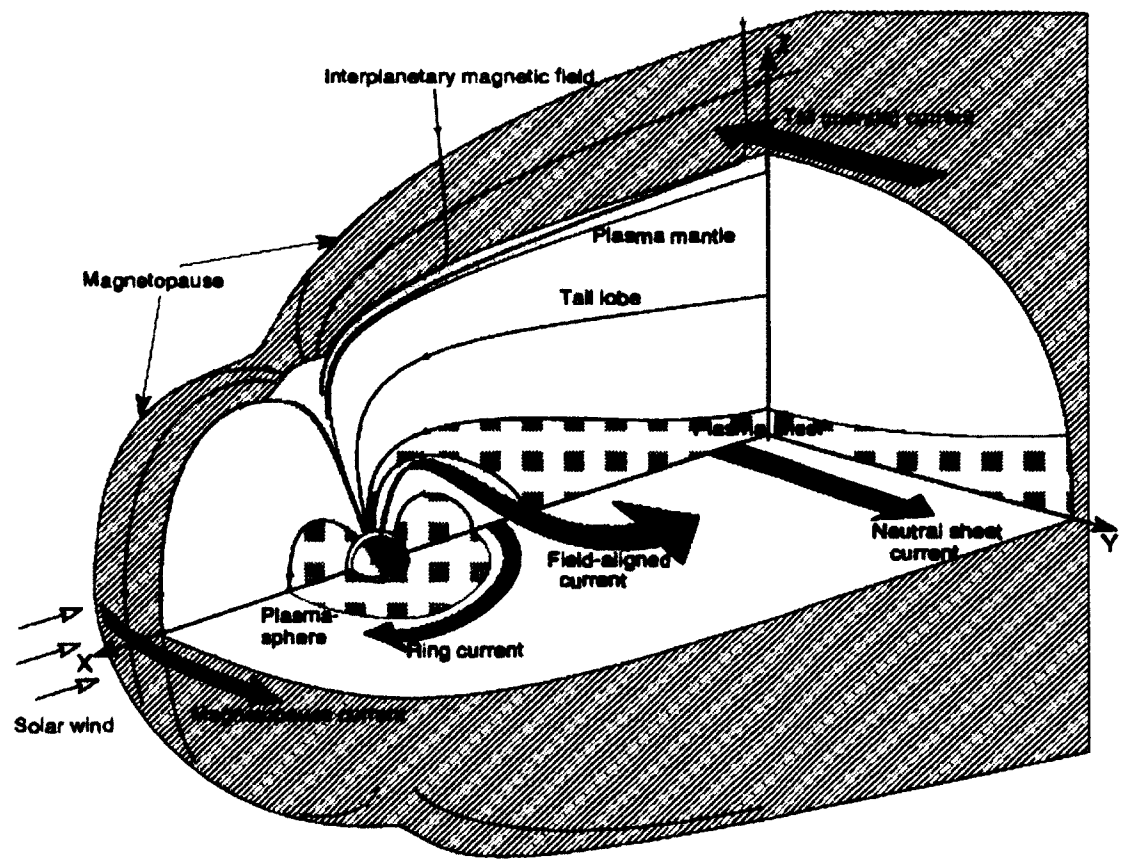
Figure 1.1: Magnetospheric boundary layers and currents [*Otto*, 2010].

try layer near the polar cusps and the plasma mantle (PM) along the high-latitude magnetotail [*Sibeck et al.*, 1999]. The formation of the LLBL, or the mechanism of the plasma transport from the solar wind into the Earth's magnetosphere is a critical problem in the magnetosphere physics, and is still not fully resolved. Several processes have been proposed to account for this transport, i.e., magnetic reconnection (tearing mode), Kelvin-Helmholtz (KH) instability, finite Larmor radius effects, diffusion, impulsive penetration, and direct cusp entry [*Sibeck et al.*, 1999]. Among them, magnetic reconnection and KH instability are considered as two of the most important processes. I will introduce these two processes in Section 1.3 and 1.4. Before that, a background on magnetohydrodynamics (MHD) helps to understand the underlying physics and plasma properties for these physics processes, which will be discussed in Section 1.2.

1.2 Basic Equations and Their Properties

1.2.1 MHD Equations and Normalization

A very rigorous way with the least assumptions to treat space plasma physics is through kinetic theory [*Lifshitz and Pitaevskii*, 1981]. However, the typical spatial and temporal scales of a space plasma are often much larger than kinetic scales. Therefore, small scale fluctuations are usually not taken into account, and a kinetic treatment of large scale plasma processes is not feasible for analysis and numerically not possible with current computer resources. Neglecting those small scale fluctuations through spatial and temporal averages, yields the magnetohydrodynamic (MHD) equations, a fluid approach to describe the self-consistent plasma interaction with the electric and magnetic fields. The MHD equations are given by [*Krall et al.*, 1974]:

$$\frac{\partial \rho}{\partial t} + \nabla \cdot (\rho \mathbf{V}) = 0, \tag{1.1}$$

$$\frac{\partial \rho \mathbf{V}}{\partial t} + \nabla \cdot (\rho \mathbf{V}\mathbf{V}) = -\nabla p + \mathbf{j} \times \mathbf{B}, \tag{1.2}$$

$$\frac{\partial \mathbf{B}}{\partial t} = -\nabla \times \mathbf{E}, \tag{1.3}$$

$$\frac{m_e m_i}{e^2 \rho} \left[\frac{\partial \mathbf{j}}{\partial t} + \nabla \cdot (\mathbf{V}\mathbf{j} + \mathbf{j}\mathbf{V}) \right] - \frac{M}{e\rho} \nabla p_e + \frac{m_i}{e\rho} \mathbf{j} \times \mathbf{B} + \eta \mathbf{j} = \mathbf{E} - \mathbf{V} \times \mathbf{B}, \tag{1.4}$$

$$\frac{1}{\gamma - 1} \left(\frac{\partial p}{\partial t} + \nabla \cdot p\mathbf{V} \right) = -p\nabla \cdot \mathbf{V} + \eta j^2, \tag{1.5}$$

$$\mu_0 \mathbf{j} = \nabla \times \mathbf{B}, \tag{1.6}$$

where ρ is the plasma density, $\mathbf{V}$ is the plasma velocity, p is the thermal pressure, $\mathbf{j}$ is the current density, $\mathbf{B}$ is the magnetic field, $\mathbf{E}$ is the electric field, $m_e = 9.1094 \times 10^{-31}$ kg is the electron mass, $m_i = 1.6726 \times 10^{-27}$ kg is the ion mass, $e = 1.6022 \times 10^{-19}$ C is the elementary charge, $M = m_e + m_i \approx m_i$, η is the resistivity, $\gamma = 5/3$ is the ratio of specific heats, and $\mu_0 = 4\pi \times 10^{-7}$ H $\cdot$ m^{-1} is the vacuum permeability, e.g., [Huba et al., 2006].

For convenience, I normalize these equations to the typical values, i.e., $B = B_0 \widehat{B}$, $\rho = \rho_0 \widehat{\rho}$. For all typical values see Table 1.1. The actual choice of the normalization values L_0, B_0, etc., depends on the physical system under consideration. I will later introduce such typical parameters for the Earth's magnetospheric boundary for the particular applications in this thesis. The normalized equations are as follows, where I have omitted the "$\wedge$" for the normalized quantities for convenience.

Table 1.1: Physical quantities and typical values

Physical quantity f	Typical value f_0
length scales L	L_0
mass density ρ	$n_0 m_i$
magnetic field $\mathbf{B}$	B_0
velocity $\mathbf{V}$	$V_A = B_0 \left(\mu_0 \rho_0\right)^{-1/2}$ (Alfvén speed)
time t	$T_A = L_0/V_A$ (Alfvén time)
pressure p	$P_0 = B_0^2 / \left(2\mu_0\right)$
electronic current density $\mathbf{j}$	$J_0 = B_0 / \left(\mu_0 L_0\right)$
electronic field $\mathbf{E}$	$E_0 = V_0 B_0$
resistivity η	η_0

$$\frac{\partial \rho}{\partial t} + \nabla \cdot (\rho \mathbf{V}) = 0, \tag{1.7}$$

$$\frac{\partial \rho \mathbf{V}}{\partial t} + \nabla \cdot (\rho \mathbf{V}\mathbf{V}) = -\nabla \left(\frac{1}{2}p\right) + \mathbf{j} \times \mathbf{B}, \tag{1.8}$$

$$\frac{\partial \mathbf{B}}{\partial t} = -\nabla \times \mathbf{E}, \tag{1.9}$$

$$\frac{l_e^2}{\rho} \left[\frac{\partial \mathbf{j}}{\partial t} + \nabla \cdot (\mathbf{V}\mathbf{j} + \mathbf{j}\mathbf{V})\right] - \frac{l}{\rho}\nabla \hat{p}_e + \frac{l}{\rho}\mathbf{j} \times \mathbf{B} + \eta \mathbf{j} = \mathbf{E} + \mathbf{V} \times \mathbf{B}, \tag{1.10}$$

$$\frac{1}{\gamma - 1}\left(\frac{\partial p}{\partial t} + \nabla \cdot p\mathbf{V}\right) = -p\nabla \cdot \mathbf{V} + 2\eta j^2, \tag{1.11}$$

$$\mathbf{j} = \nabla \times \mathbf{B}, \tag{1.12}$$

where $l_e = \lambda_e L_0^{-1}$, $l = \lambda_i L_0^{-1}$, $\hat{p}_e = p_e P_0^{-1}$, $\lambda_e = c/\omega_e$ is the electron inertia scale, $\lambda_i = c/\omega_i$ is the ion inertia scale, c is the speed light, $\omega_e = \sqrt{(ne^2)/(\epsilon_0 m_e)}$ is the electron frequency, and $\omega_i = \sqrt{(ne^2)/(\epsilon_0 m_i)}$ is the ion frequency. For a constant resistivity, the normalized η^{-1} is the Lundquist number $R = \eta_0^{-1}\mu_0 L_0 V_A$.

Equation (1.7) is the continuity equation, where the second term is the divergence of the mass density flux. Equation (1.8) is the momentum equation. On the left-hand

side of the equation is the inertia term, the first term on the right-hand side is the pressure gradient, and the second term is the magnetic force. Equation (1.9) is the induction equation from the Maxwell equations and Equation (1.10) is general Ohm's law. The second term on the right-hand side of Equation (1.10) is the convection term. The first term on the left-hand side of Equation (1.10) is the electron inertia term, which is important only when the typical length is comparable to the electron inertia scale ($l_e \sim \mathcal{O}(1)$). The second term is electron pressure term and the third term is the Hall term. Both become important when typical length scales are comparable to the ion inertia scale ($l \sim \mathcal{O}(1)$). However, the electron pressure can often be ignored in the magnetosphere where $p_e \ll P_0$. The last term is the resistive diffusion term. In most of space environments, the plasma is collisionless. Therefore, the resistivity is negligible almost everywhere. Note, that a possible exception is the diffusion region of magnetic reconnection, as explained later. Equation (1.11) is the pressure or thermal energy equation. Equation (1.12) is Ampere's law, where the displacement current is neglected because the maximum wave speeds for my application are much smaller than the speed of light.

1.2.2 MHD Equations and Conservation Laws

The continuity equation implies that total mass is conserved. By combining the continuity equation and the momentum equation, I obtain a conservative form of the momentum equation

$$\frac{\partial (\rho \mathbf{V})}{\partial t} = -\nabla \cdot \left[\rho \mathbf{V V} + \frac{1}{2} \left(p + B^2 \right) \mathbf{I} - \mathbf{B B} \right], \tag{1.13}$$

where $\mathbf{I}$ is the unit tensor. The divergence on the right hand side implies that the total momentum of a system with closed boundaries is conserved. Especially, for an equilibrium without curved magnetic field lines, this equation implies total pressure balance.

If I ignore all the terms on the right-hand side of general Ohm's law, and combine it with the induction equation, I can eliminate the electric field and obtain an equation

for the evolution of the magnetic field:

$$\frac{\partial \mathbf{B}}{\partial t} = \nabla \times (\mathbf{V} \times \mathbf{B}).$$

(1.14)

This equation reveals a very important property of the plasma, which is so-called "frozen-in" condition [*Kallenrode*, 2004]. The frozen-in condition implies that the magnetic flux through a closed contour which moves with the plasma is constant. Equivalently this also implies that two fluid plasma parcels that are connected by a magnetic field line (line along the magnetic field vectors) are always connected by a magnetic field line. This provides a way to identify a magnetic field line through the plasma elements. Note, that the inclusion of Hall physics leads to the separation of ion and electron velocity. With the relation

$$\mathbf{V}_e = \mathbf{V} - \frac{l}{\rho}\mathbf{j},$$

(1.15)

Ohm's law including the Hall term becomes

$$\mathbf{E} = -\mathbf{V}_e \times \mathbf{B},$$

(1.16)

which demonstrates that the frozen-in condition now applies to the electrons only.

Using the frozen-in condition in the plasma, a magnetic flux tube can be associated with physical properties such as volume or mass. Therefore, to discuses the overall quantity in a flux tube is meaningful. For example, the volume of a closed magnetic flux tube (magnetosphere or magnetic mirror) is given by

$$V = \int \left(\iint ds \right) dl,$$

(1.17)

where s is the flux tube cross section varying along the flux tube, dl is infinitesimal length along magnetic field. For a "sufficiently thin" flux tube the cross section of the tube varies as

$$s \sim B^{-1}.$$

(1.18)

This leads a definition of the differential flux tube volume

$$V_{ft} = \int \frac{dl}{B}.$$

(1.19)

This concept can also be used to evaluate the total number of particles on a differential flux tube through

$$N_{ft} = \int n dV = \int n s dl \sim \int \frac{\rho}{B} dl. \tag{1.20}$$

Provided that the frozen-in condition applies and that the flux tube has well defined "end points" at which no mass is lost ($V_\parallel = 0$), the continuity equation can be used to show that the mass of this flux tube is conserved. With a similar motivation, I can also define the flux tube entropy

$$H_{ft} = \int \frac{p^{1/\gamma}}{B} dl. \tag{1.21}$$

Using the pressure equation it is possible to show that $p^{1/\gamma}$ satisfies a continuity equation such that the flux tube entropy is also a conserved flux tube property for the same provisions as for flux tube mass conservation. Those physical quantities are very useful in the space physics. In the next section, I will show an important example when the frozen-in condition is violated.

Finally, combing the continuity equation and thermal energy equation, I can derive an equation for $p\rho^{-\gamma}$ which is a measure of local plasma entropy

$$\frac{d}{dt}\left(\frac{p}{2\rho^\gamma}\right) = (\gamma - 1)\frac{\eta j^2}{\rho^\gamma}, \tag{1.22}$$

where $d/dt = \partial/\partial t + \mathbf{V} \cdot \nabla$. This equation shows that resistive Ohmic heating is the only (nonadiabatic) source for an increase of entropy $S = p/(2\rho^\gamma)$ and S is conserved along a fluid path in the absence of resistive heating consistent with the properties of entropy. Note, that the factor 1/2 arises from my normalization. One can also combine all the equations (Equation (1.7) - (1.12)), to derive an energy conservation equation, which will be discussed in Chapter 3.

1.3 Magnetic Reconnection

Magnetic reconnection is a process in which plasma is transported across a separatrix surface [*Otto*, 2012]. Figure 1.2 shows a typical magnetic reconnection configuration. The magnetic field lines that cross in the center are called separatrices and the point

where they cross is called an X-point or X-line (when the three-dimensional aspect is emphasized). At $t = t_1$, particles p_1 and p_2 are connected by the same magnetic field line l_1, while particles p_3 and p_4 are connected by the same magnetic field line l_2. l_1 and l_2 are anti-parallel and approach each other. At $t = t_2$, reconnection takes place at the X point, where l_1 and l_2 are connected. All those four particles are convected to the position of the X-line which implies that the magnetic field line on which they are located is now the new separatrix. At $t = t_3$, those four particles are now in the outflow. Particle p_1 and p_4 are connected by the same magnetic field line l_3, while particle p_2 and p_3 are connected by the same magnetic field line l_4.

The key point of this magnetic reconnection is the localized diffusion, violating of the frozen-in condition in a very small vicinity of the X-line which is called the diffusion region. There are three important properties of this process.

1. Magnetic reconnection changes the magnetic topology, which allows fast mixing of plasma of different origin [*Dungey*, 1961; *Otto*, 1999]. This property is important for the solar wind plasma access to the Earth's magnetosphere at the LLBL for southward interplanetary magnetic field (IMF) conditions. For northward IMF conditions, magnetic reconnection may occurs at the cusp regions [*Adamson et al.*, 2012], or it may be driven by the KH instability [*Otto and Fairfield*, 2000].

2. Magnetic reconnection converts a large amount the magnetic energy (stored energy) into the bulk kinetic energy (plasma acceleration) and thermal energy in a short time, which is important for the acceleration of plasma in the magnetosphere (bursty bulk flows, plasmaoids, magnetic flux transfer events), and which potentially explain solar coronal heating and heating of magnetospheric plasma. [*Birn and Priest*, 2007].

3. As an irreversible process, magnetic reconnection changes both the local and total entropy. One of the outstanding compelling problems of space physics is the strong nonadiabatic heating of the solar corona but also albeit on a smaller
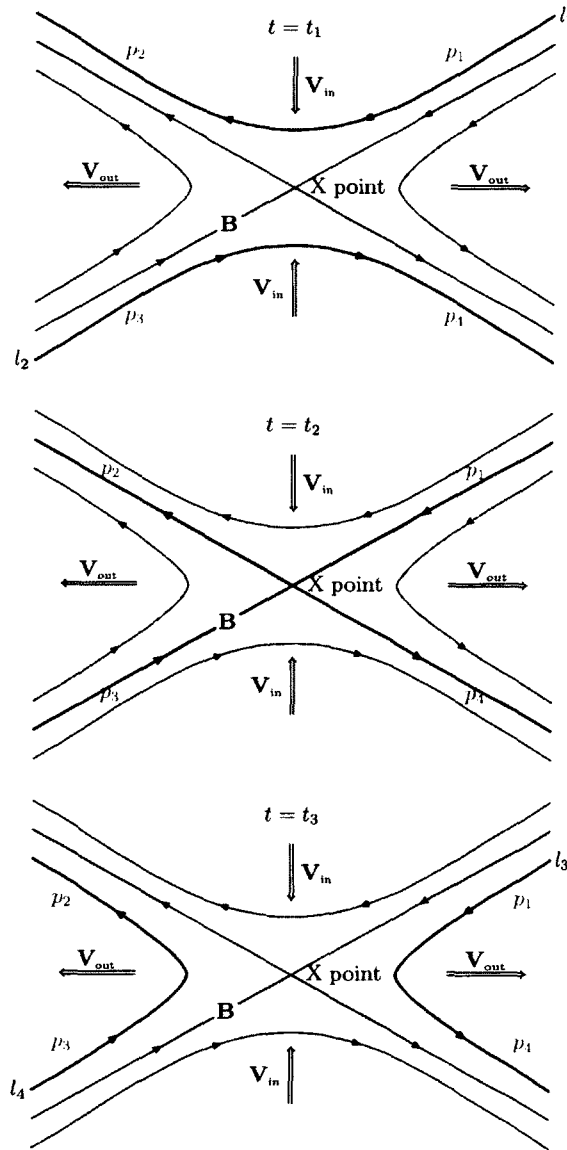
Figure 1.2: Sketch of the magnetic reconnection geometry and the associated plasma and magnetic flux transport.

scale of magnetospheric plasma. In Chapter3, I will discuss more about this property.

Historical, the concept of magnetic reconnection was first introduced by *Giovanelli* [1946, 1947] to explain solar flares. *Dungey* [1961] applied this concept to introduce the concept of an open magnetosphere. The first stationary two-dimensional magnetic reconnection model was proposed by *Sweet* [1958] and *Parker* [1957]. In their model, the magnetic flux is convected into the diffusion region at an inflow region speed

$$v_i \sim v_{Ai} R^{-1/2},$$ (1.23)

where $R = \mu_0 L_0 v_{Ai} \eta_0^{-1}$ is the Lundquist number, v_{Ai} is the inflow Alfvén speed. In two-dimensional steady-state models the electric field E in the invariant direction is uniform in space. Thus, the Alfvén Mach number

$$M_{Ai} = \frac{v_i}{v_{Ai}} = \frac{v_i B_i}{v_{Ai} B_i} = \frac{E}{v_{Ai} B_i},$$ (1.24)

provides a quantitative measure of the rate of the flux magnetic transport (also called the "reconnection rate"), normalized by the typical electric field $v_{Ai} B_i$. In terms of this number, the Sweet-Parker reconnection rate is

$$r = M_{Ai} \sim R^{-1/2}.$$ (1.25)

However, in a space plasma environment the Lundquist numbers are always large. Therefore, this magnetic reconnection model is too slow to explain the real physical phenomena in the space environment. To resolve this problem, *Petschek* [1964] first pointed out that a much larger reconnection rate would be possible if the diffusion region were much shorter. Figure 1.3 illustrates the Petschek reconnection geometry. In his model, a tiny diffusion region is bound by two pairs of slow shocks, the outflow region plasma is strongly accelerated and heated by the slow shocks. The maximum reconnection rate in this model is about

$$r \sim \frac{\pi}{8 \ln R},$$ (1.26)
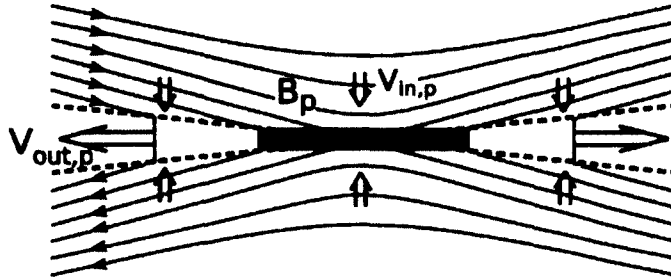
Figure 1.3: Illustration of the diffusion region and the attached slow shocks in Petschek's reconnection model.

which is much faster than for the Sweet-Parker model. Another important property of Petscheck reconnection is a fairly weak dependence on the macroscopic length scale L_0. For Lundquist number ranging from 10^2 to 10^{20}, the Petscheck reconnection rate various only between 0.09 and 0.01, which is in reasonable agreement with observations of macro plasma transport for most space plasma systems [$Otto$, 2012].

The above stationary models are based on the MHD frame work. Thus, resistivity is the only source to break down the frozen-in condition. However, in a space environment, plasma is usually considered as a superconductor. Thus, to facilitate magnetic reconnection in MHD, one has to make an ad hoc assumption for the resistivity or include more physics, i.e., an electron pressure tensor, electron inertia, or explicit kinetic processes and instabilities. The latter options not only require the inclusion of complex additional physics but also the resolution of kinetic length scales in large scale plasma models, which for most applications requires computer resources far beyond today's capabilities.

Here I only consider the resistive term. Assuming a width of the current layer of δ, the current density can be approximated by

$$j = en\left(v_i - v_e\right) = \frac{B}{\mu_0 \delta}, \tag{1.27}$$

where v_i and v_e is the ion and electron speed, respectively. Normalized by the typical

value, Equation (1.27) can be rewritten as

$$\frac{v_i - v_e}{v_A} = \frac{\lambda_i}{\delta},$$ (1.28)

which indicates that thin current layers require large drift speeds of the current carriers. As a reminder, λ_i is the ion inertia scale. However, large drift velocities are expected to generate micro-instabilities when this velocity significantly exceeds the ion thermal speed v_{th}. The turbulent interaction of the waves of the instability with the current carrying particles will slow the particle to conditions sub-critical for the instability [Otto, 2012]. The overall effect is equivalent to a resistivity. Assuming a critical velocity for the onset of micro-instabilities of $v_c = \alpha c_s$, where $c_s = \sqrt{(\gamma p)/(2\rho)}$ is the ion acoustic speed, implies that α is of order unity when the ion inertia scale is comparable to the normalization length L_0. In reality, α is determined by the onset conditions for current driven turbulence in a strong current. Since the exact choice has minor influence on the macroscopic dynamics, it is used in my numerical model as a free parameter to adjust magnetic reconnection onset condition. For example, In the three-dimensional simulations, three resistivity models are applied, which are given by:

Model 1: $\eta_1 = \eta_0 \sqrt{j^2 - j_c^2} H (j - j_c) + j_b,$ (1.29)

Model 2: $\eta_2 = \eta_0 \sqrt{j - j_c} H (j - j_c) + j_b,$ (1.30)

Model 3: $\eta_3 = \eta_0 \left(j^2 - j_c^2\right) H (j - j_c) + j_b,$ (1.31)

where $H(x)$ represents a step function, $j_c = \rho v_c = \alpha\sqrt{\gamma \rho p/2}$ the critical electric density, and j_b the background resistivity. Therefore, the onset current layer width is given by

$$\delta = \lambda_i v_A / v_c \sim \lambda_i \left(\alpha\beta\right)^{-1},$$ (1.32)

where β is the plasma beta $2\mu_0 p/B^2$. At the magnetopause $\beta \approx 0.1 \sim 1$, but near the X-point the plasma β can be higher, which indicates that the diffusion region is at least on the ion inertia scale. Thus it is potentially important to include Hall

physics into a model of magnetic reconnection at the magnetopause. Although Hall physics does not violate the frozen-in condition, the frozen-in condition outside of the diffusion region applies to electrons, the inclusion of the Hall term achieves much higher reconnection rates than MHD [*Otto*, 2001; *Ma and Bhattacharjee*, 2001]. The Hall reconnection rate is comparable to the rate obtained by other plasma descriptions which include additional physics, i.e., electron pressure and kinetic models [*Birn et al.*, 2001].

Observational evidence of magnetopause reconnection was first presented by *Russell and Elphic* [1978]. By using ISEE satellite data, they found many events with a bipolar signature in the magnetic field component normal to the magnetopause boundary (B_N). Another feature is an enhanced magnetic field strength at the center of the event [*Russell and Elphic*, 1978]. They called these structures as flux transfer events (FTEs) and assumed they represented magnetic flux ropes in which magnetic flux connecting magnetosheath and magnetosphere is caused by localized patchy reconnection.

1.4 The Kelvin-Helmholtz Instability

The Kelvin-Helmholtz (KH) instability is one of the most important instabilities in geophysics. It occurs in the presence of a large shear flow across a thin boundary layer. It can be easily found in our physical environment, such as water ripples on a lake surface and waving flags generated by wind, or the vortices at the confluence of two rivers. It is also found that the KH instability can be observed in such space areas as the solar corona, the ionosphere, and astrophysical objects (M82) [*Foullon et al.*, 2011; *Birk et al.*, 1999]. The well known application of KH instabilities are the surface waves at the Earth's magnetospheric boundary. Figure 1.4 illustrates KH vortices close to the equatorial plane at the duskside magnetopause for northward IMF conditions [*Hasegawa et al.*, 2004]. The thickness of the magnetospheric boundary is around 100 to 1000 km, which is comparable to the ion inertia scale. The magnetospheric boundary provides a good candidate for the occurrence of KH instability because of

the high velocity on the solar wind side and a stagnant flow on the magnetospheric side of the boundary.

The KH instability is highly efficient to mix material and momentum from both sides of a shear flow boundary. Therefore, its macroscopic effect is equivalent to diffusion and viscosity. At the magnetospheric boundary, *Axford* [1964] suggested the KH instability as a possible mechanism for viscous coupling between the solar wind and the Earth's magnetosphere.

Chandrasekhar [1961] studied the KH instability as one among several interchange instabilities. He assumed an incompressible homogeneous plasma on the two sides of a discontinuous tangential flow including a homogeneous tangential magnetic field and calculated the growth rate of the KH instability q:

$$q = \sqrt{\alpha_1 \alpha_2 \left[(\mathbf{V_1} - \mathbf{V_2}) \cdot \mathbf{k} \right]^2 - \alpha_1 (\mathbf{V_{A1}} \cdot \mathbf{k})^2 - \alpha_2 (\mathbf{V_{A2}} \cdot \mathbf{k})^2}, \qquad (1.33)$$

where the indices refer to the two sides of the shear flow layer, $\alpha_i = \rho_i/(\rho_1 + \rho_2)$, $\mathbf{k}$ is the wave vector of the perturbation, and $\mathbf{V_{Ai}} = \mathbf{B_i}/\sqrt{\rho_i}$ is the Alfvén velocity. Important properties implied by the dispersion relation in Equation (1.33) are:

1. In the absence of a magnetic field, the KH instability is always operating as long as there is a nonzero shear flow $\mathbf{V_1} - \mathbf{V_2} \neq 0$. The growth rate is proportional to the $\mathbf{k}$ vector, indicating that the fastest growth is for the smallest wavelengths.

2. The magnetic field can entirely stabilize the mode if there is a sufficiently large magnetic field component along the $\mathbf{k}$ vector. In order words, the kinetic energy of the shear flow has to be large enough to overcome the magnetic tension force.

3. If the magnetic field is perpendicular to the $\mathbf{k}$ vector, it does not affect the KH instability growth rate. Therefore, this magnetic field can be treated as an additional pressure.

It is worth mentioning that the vortices generated by the KH instability are moving at the velocity $\bar{\mathbf{V}} = \alpha_1 \mathbf{V_1} + \alpha_2 \mathbf{V_2}$. Thus it is convenient to perform a Galilean
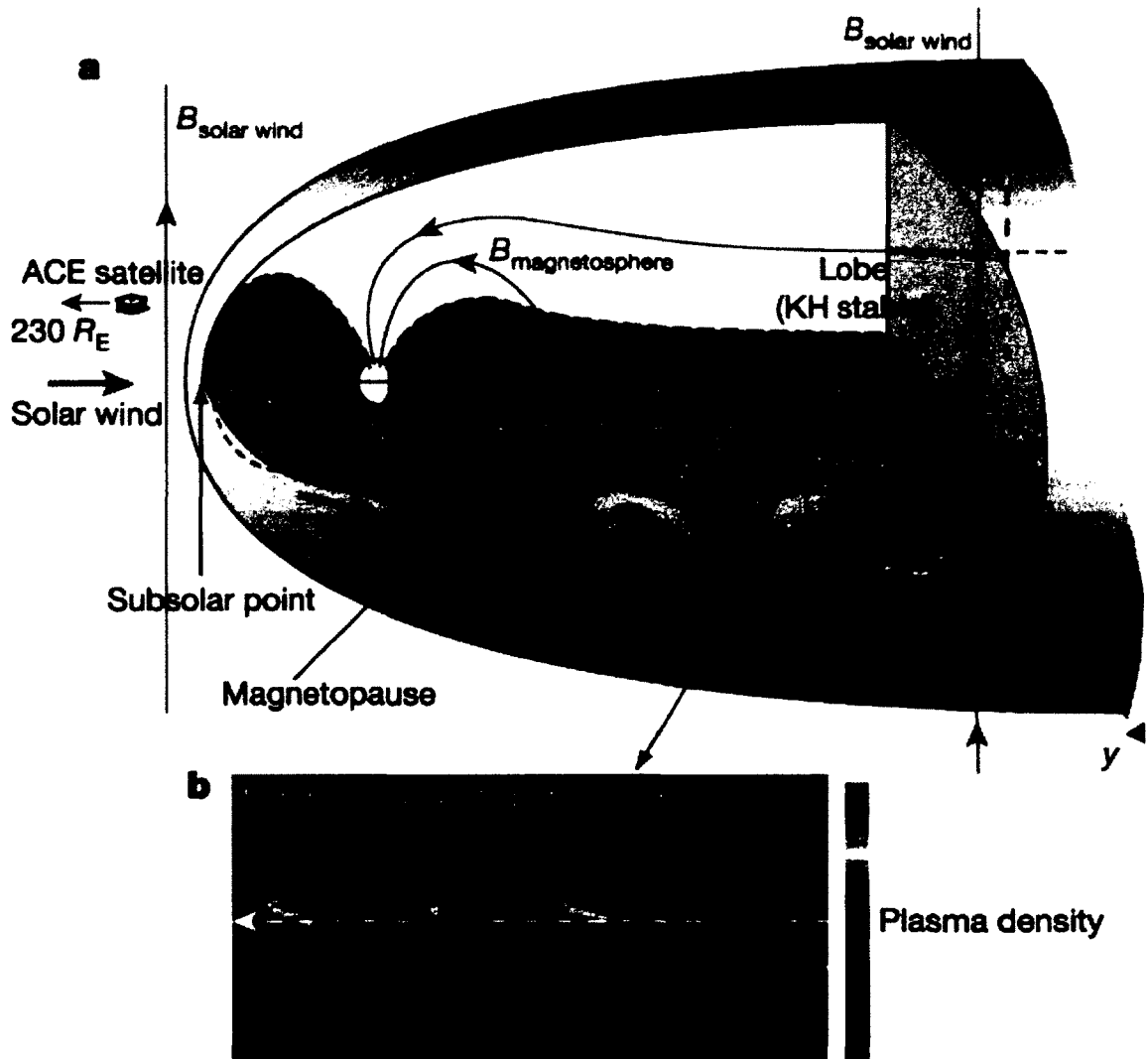
Figure 1.4: (a) Cartoon of the magnetosphere, showing the KH vortices at the dusk-side magnetopause. (b) Vortex structure resulting from a three-dimensional numerical simulation of the MHD KH instability under a magnetosphere-like geometry, with the plasma sheet sandwiched between the two lobes [*Hasegawa et al.*, 2004].

transformation and use a frame in which the KH vortex is stationary. Hereafter, most of the results are based on this frame.

Although the most important properties of the KH instability are illustrated above, the basic assumptions have some important limitations. It is expected that compressibility will stabilize the system. KH instability can not operate if the initial velocity on the two sides is larger than a critical value [*Pu and Kivelson*, 1983; *Miura and Pritchett*, 1982]. The assumption of incompressibility assumption assumes an infinite ion-acoustic speed. In order to generate the flow in and around the vortices, the system must pass the information on the obstacle downstream. However, a supersonic flow prevents this information transport such that the instability cannot operate anymore.

The assumption of an infinitely thin shear flow layer implies a width of the shear layer which is small compared to the wavelength. This is often violated because the fastest growth mode is always the smallest typical length scale in the system. Therefore, the fastest mode always has a wavelength which is comparable to 2π times the width of the shear flow layer. Using two-dimensional MHD simulations, *Miura and Pritchett* [1982] have shown that the fastest growth rate requires $ka \approx 0.5 \sim 1$, where a is the half width of shear flow, and KH instability will be switched off when $ka > 2$.

The KH instability as an efficient transport of energy and momentum across the plasma boundary have been demonstrated by a number of two-dimensional MHD simulations [*Miura*, 1982, 1984, 1987, 1992, 1996; *Miura and Pritchett*, 1982]. However, as an ideal instability, the KH instability does not violate the "frozen-in" condition. Nevertheless, more recent two- and three-dimensional simulations for northward IMF conditions have demonstrated the formation of very thin current layers in the non-linear vortices of KH waves. In resistive MHD, these current layers force magnetic reconnection to operate which allows the plasma to cross the magnetospheric boundary [*Otto and Fairfield*, 2000; *Nykyri and Otto*, 2001, 2004; *Otto*, 2008]. Figure 1.5 illustrates two types of magnetic reconnection driven by KH waves. The first type

occurs in the case where the magnetic field components along the **k** vector of KH instability are anti-parallel across the velocity shear layer (anti-parallel case). The second type occurs for flow shear strong enough to produce well developed large size KH vortices and strongly stretched field lines therein (strong KH instability case) [*Nakamura et al.*, 2006, 2008]. It is often reported in numerical simulations that the fastest modes (also usually short wavelength modes) are the first to reach a saturation state. A merging of neighboring vortices to form a longer wavelength mode has often been observed in simulations [*Nakamura and Fujimoto*, 2008]. Another property is a periodic increase and decrease of density by the KH waves, which modulates the local ion acoustic speed. Once the ion acoustic speed is below the bulk velocity, a fast shock can be formed [*Miura*, 1984; *Wu*, 1986]. It is demonstrated that the net plasma transport due to reconnection inside KH vortices is unaltered in a Hall-MHD approximation and the Hall-MHD growth rates are about 20% larger than the corresponding MHD growth rates [*Nykyri and Otto*, 2004].

The KH instability at the magnetopause has been widely confirmed by means of the satellite observation [*Fairfield et al.*, 2000; *Hasegawa et al.*, 2004; *Hwang et al.*, 2011]. A good example is the event on March 24, 1995 [*Fairfield et al.*, 2000]. "For several hours the Geotail spacecraft remained near the dusk-side magnetotail boundary some 15 R_E behind the Earth while the solar wind remained very quiet with a very steady 11 nT northward magnetic field. Geotail experienced multiple crossings of a boundary between a dense, cold, rapidly flowing magnetosheath plasma and interior region characterized by slower tailward velocities and lower but substantial densities and somewhat hotter ions. The crossings recurred with a roughly three minute periodicity, and all quantities were highly variable in the boundary region, especially the B_z component showed strong short-duration fluctuations in which B_z could even reach negative values. The observation also suggests direct entry of plasma through the boundary as the source of high densities in the plasma sheet" [*Fairfield et al.*, 2000]. *Otto and Fairfield* [2000] used two-dimensional MHD simulations to show that the fluctuations can be explained by the KH instability if the **k** vector of the in-

T=50[D/V0]   T=75   T=125   T=200

density

Y

0   X   15D   MA=2.5, D=2,α=-1.0   0.9   1.1

type-I RX   ~1/3λKH

(a)   (b)   (c)   (d)
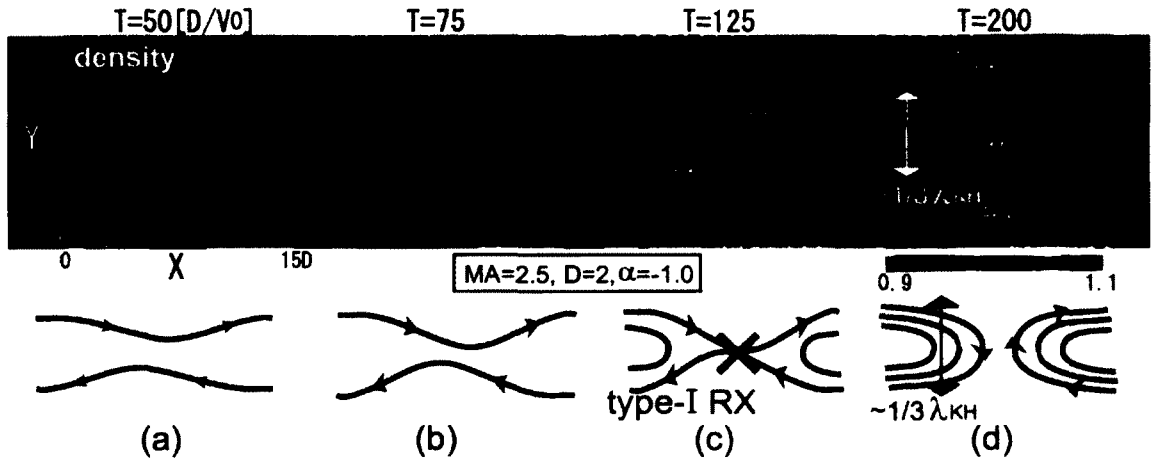
(a) First type reconnection driven by KH mode. (Top) Density contours and flow vectors for ion and magnetic field lines. (Bottom) Sketch of the evolution of magnetic field lines. The cross shows the reconnection site.

T=80[D/V0]   T=105   T=115   T=180

density

Y

Injection

0   X   15D   MA=7.0, D=2,α=0.0   0.95   1.05

Injection

type-II RX

(a)   (b)   (c)   (d)
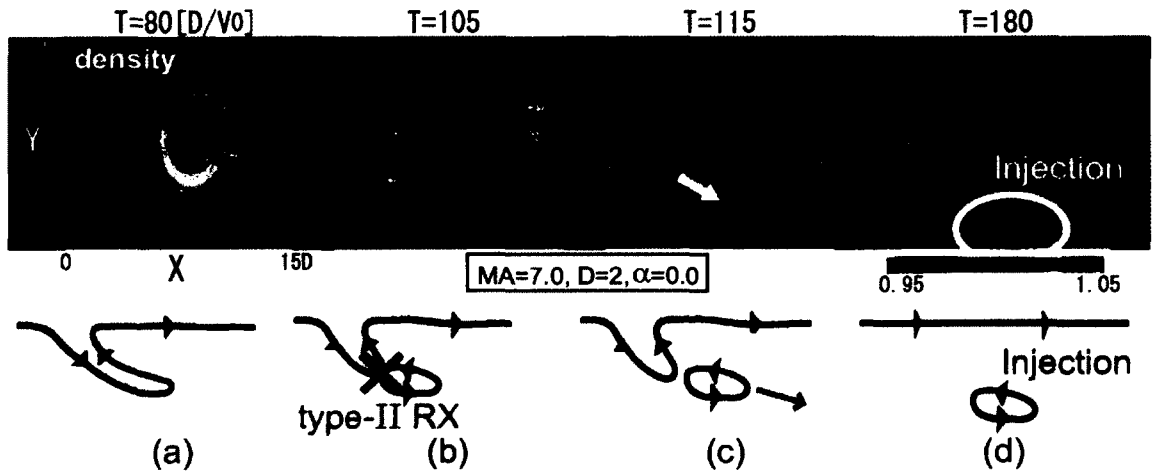
(b) Second type reconnection driven by KH mode. (Top) Density contours and flow vectors for ion and magnetic field lines. (Bottom) Sketches of the evolution of magnetic field lines. The blue crosses show the reconnection sites, and the blue arrows show the motions of the magnetic islands.

Figure 1.5: Two different types of magnetic reconnection driven by KH mode [*Nakamura et al.*, 2008].

stability has a component along the magnetic field direction. "The results suggest an average KH wavelength of about $5\,R_E$, with a vortex size of close to $2\,R_E$ for an average repetition time of 2.5 min. The growth time for these waves implies a source region of about $10 \sim 16\,R_E$ upstream from the location of the Geotail spacecraft. The simulations also indicate a considerable mass transport of magnetosheath material into the magnetosphere by magnetic reconnection in the KH vortices" [*Otto and Fairfield*, 2000].

Recently, *Hwang et al.* [2011] presented the first in situ observation of nonlinearly developed KH waves during southward IMF. "The analysis revealed a mixture of less-developed and more-developed KH waves that shows inconsistent variations in scale size and magnetic perturbations consistent with the expected evolution of KH structures. A coherence analysis implied that the observed KH waves under southward IMF appear to be irregular and intermittent. These irregular and turbulent characteristics are more pronounced than previously reported KH waves events for preferentially northward IMF conditions" [*Hwang et al.*, 2011].

1.5 Motivation and Outline of the Thesis

As mentioned before, both magnetic reconnection and Kelvin-Helmholtz instabilities at the Earth's magnetopause have been studied by numerous authors in the past half-century. However, there are still some major important open questions in this area, among them the problems outlined below.

1.5.1 Entropy Changes Associated with Magnetic Reconnection

As mentioned before, entropy is a conserved quantity in the ideal MHD. However, many observations indicate that the plasma in the magnetosphere is strongly heated and has an entropy that is orders of magnitude higher than its solar wind origin. Only a small fraction of this nonadiabatic heating is explained by the Earth's bow shock, such that the high entropy of magnetospheric plasma is still a fundamentally important and unresolved issue. Figure 1.6 summarizes observed values of the typical

entropy $S = p\rho^{-\gamma}$ in the solar wind and magnetosphere. In the magnetosphere, satellite observations show that ions in the Earth's plasma sheet become cold and dense during prolonged periods of northward IMF, which has been attributed to the massive transport of the solar wind or magnetosheath ions into the plasma sheet [*Fujimoto et al.*, 1997]. There are two components of plasma in this cold dense plasma sheet, a hot distribution, which is considered a remnant of the original plasma sheet plasma, and a cold distribution, which is believed to be of magnetosheath origin [*Wang et al.*, 2007]. The typical flank magnetosheath ion density and temperature for fast solar wind conditions are about 5 cm^{-3} and 50 eV. For slow solar wind conditions, the ion density and temperature are about 8 cm^{-3} and 10 eV [*Borovsky and Cayton*, 2011]. Density and temperature for the cold plasma component are about 0.5 cm^{-3} and 500 eV [*Wang et al.*, 2007], which yield an entropy increase of about 1 $\sim$ 2 orders of magnitude compared to the magnetosheath. To determine which process can provide sufficient nonadiabatic heating may also shed light on a better understanding of the plasma transport at the magnetopause. The problem is reminiscent to the problem of coronal heating, where, again, the entropy is orders of magnitude higher than in the solar photosphere and chromosphere.

A prime candidate for the observed nonadiabatic heating is magnetic reconnection, which requires the violation of the ideal MHD by local dissipation. This is particularly attractive because it is very clear that magnetic reconnection plays a major role for the plasma transport from the magnetosheath into the magnetosphere. Therefore, the idea to resolve the problems of nonadiabatic heating and of the plasma transport is very appealing. Furthermore, entropy is the quantity to describe irreversible processes, and has not been systemically examined in magnetic reconnection. Thus in Chapter 3, I investigate systematically any entropy increase through different magnetic reconnection configurations in the framework of MHD and Hall MHD by using one- and two-dimensional numerical simulations.

23
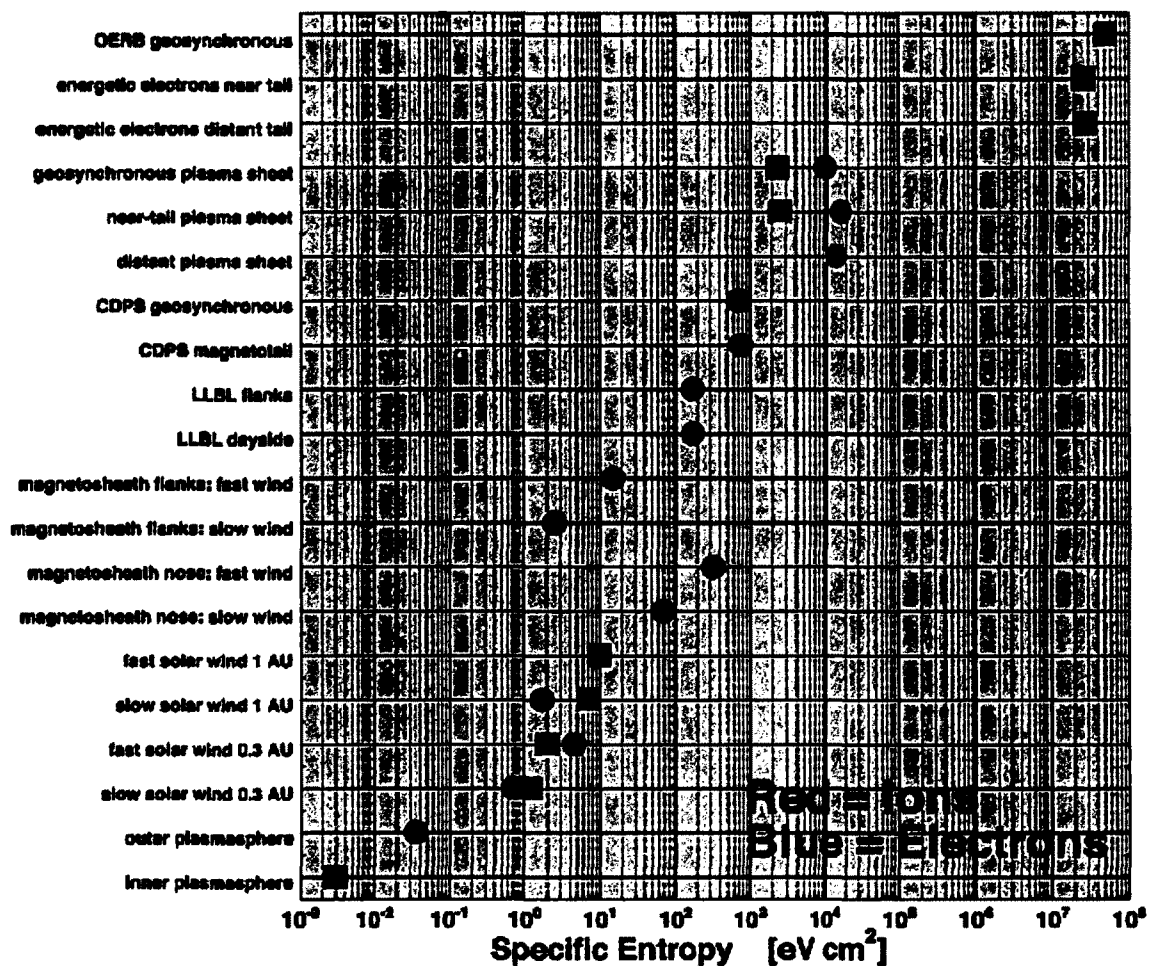
Figure 1.6: Typical entropy $S = p\rho^{-\gamma}$ values in the solar wind and magnetosphere [*Borovsky and Cayton*, 2011].

1.5.2 Field-Aligned Currents Formation in Magnetic Reconnection

Field-aligned currents (FACs) represent the current component along the magnetic field direction. Figure 1.7 is a schematic of combined FACs and ionospheric current systems. More than 100 years ago Kristian Birkeland hypothesized the existence of currents in the upper ionosphere, which are not all closed in the upper atmosphere but have currents connected to interplanetary space. Now it is well known that these currents not only exist but also play a critical role in the coupling between the magnetosphere and ionosphere. The coupling implies the existence of forces on the plasma and therefore requires the presence of currents to communicate such forces between the magnetosphere and the ionosphere. Thus, it is highly important to understand the plasma processes that generate FACs.

At the magnetopause, it is believed that FTEs represent magnetic flux ropes that connect the magnetosheath magnetic field and the geomagnetic field. Associated with these events are observations of transient acceleration and auroral emissions in the dayside polar ionosphere which are believed to be related to FTEs. If this is the case, FACs must have been generated during the reconnection process that formed the flux ropes. Therefore, FACs are key to understanding the ionospheric response to the interaction between the solar wind and the magnetosphere. In the Earth's magnetotail, the occurrence of substorms, which involves magnetic reconnection, increases the Birkeland currents (FACs), accelerates particles along field lines, and causes the aurora to brighten. Thus FACs are critical to the magnetosphere-ionosphere coupling (For more detail, see Chapter 4). These two examples clearly hint that magnetic reconnection may generate the FAC; however, the mechanism is not fully understood. Several studies examine the formation of FACs associated with magnetic reconnection and KH waves. However, most of these studies invoke three-dimensional reconnection whereas guide magnetic field or velocity shear should be very efficient to generate FACs in two dimensions. In fact, several of the three-dimensional results can probably be attributed to two-dimensional mechanisms. This problem is also relevant to better understand the formation of FACs in the shear flow geometry necessary for
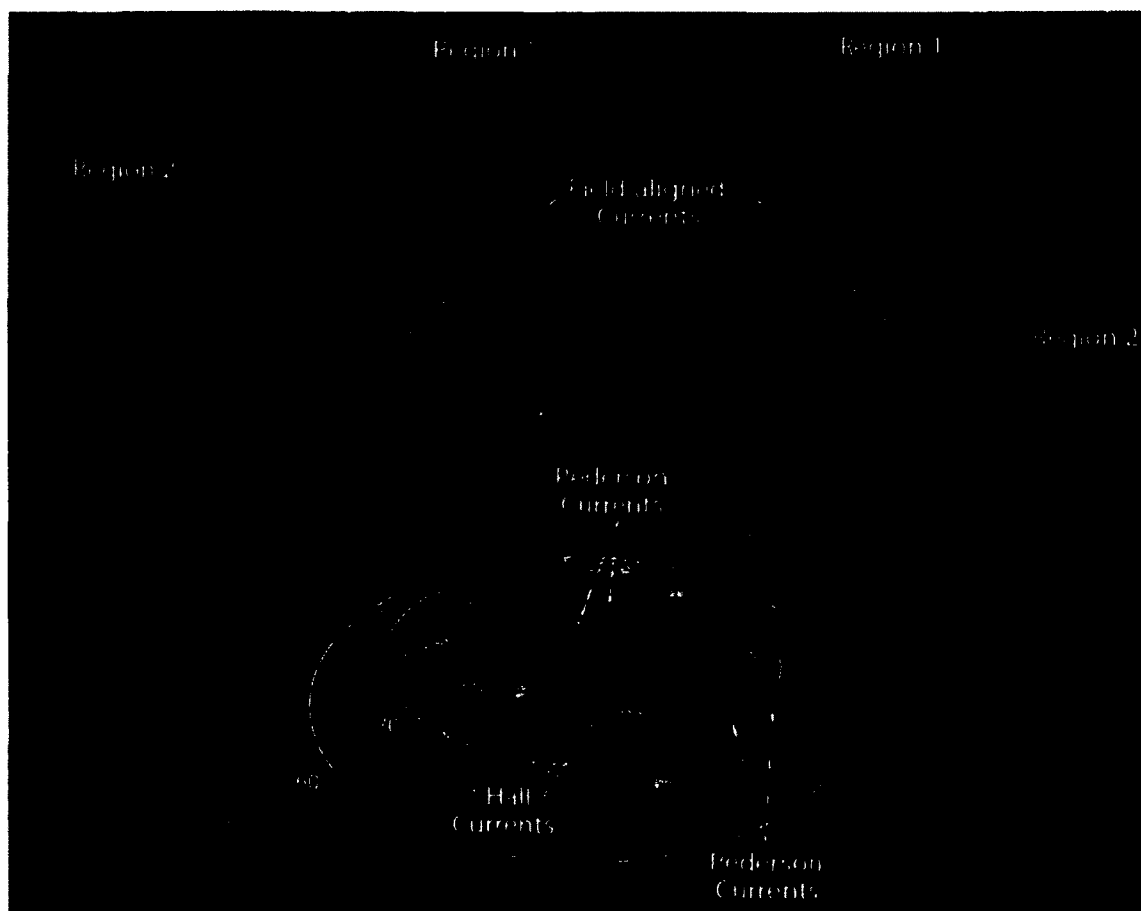
Figure 1.7: A schematic of combined FACs and ionospheric current systems [*Le et al.*, 2010].

the formation of KH waves. It has been demonstrated that the FACs generated by the velocity shear are critical for the coupling of KH and current sheet instabilities to the ionosphere [*Lysak and Song*, 1996]. In Chapter 4, I systemically examine FAC generation in two-dimensional magnetic reconnection.

1.5.3 Interaction Between Kelvin-Helmholtz Instability and Magnetic Reconnection

Magnetopause magnetic reconnection is considered the dominant process for southward IMF conditions at the Earths magnetopause. However, a shear flow, perpendicular to the reconnection plane, is always present due to the solar wind velocity. Therefore, it is expected that KH modes and magnetic reconnection operate simultaneously and interact with each other. It is important to note that magnetic reconnection and KH waves cannot simultaneously occur in two-dimensional configurations. Figure 1.8 illustrates the role of reconnection versus the role of KH instability for $\mathbf{k} \parallel \mathbf{B}$ and parallel to the velocity shear direction condition. Flow shear modifies magnetic reconnection by generating a configuration similar to a density asymmetry with a nonzero B_y in the outflow region when $|\mathbf{V}| < |\mathbf{V}_A|$ [*La Belle-Hamer et al.*, 1995]. When the shear flow value is larger than the inflow Alfvén speed ($|\mathbf{V}| > |\mathbf{V}_A|$), magnetic reconnection is switched off by KH modes [*Chen et al.*, 1997]. In cases where the directions of magnetic shear and velocity shear are not aligned, the k vectors for the respective instabilities are not aligned. Therefore, a configuration where both instabilities are permitted to operate simultaneously is necessarily three-dimensional. Several two-dimensional simulation studies were carried out considering either configurations where only reconnection can operate or where only the KH mode can operate. Thus to fully understand this interaction process, a fully three-dimensional MHD or Hall MHD simulations is required. The case of largely parallel magnetic field (for northward IMF conditions) has been investigated in three dimensions by *Takagi et al.* [2006] and *Otto* [2008]. However, southward IMF has only been considered in a global simulation study with limited resolution [*Hwang et al.*, 2011]. This study

also has not examined any details of the KH-reconnection interaction. There are also no studies to consider the effect of Hall physics in three-dimensions, although it is of potential importance because of the thin current layers that are caused by nonlinear KH waves. Therefore, Chapter 5 and 6 examine the three-dimensional interaction of KH waves and magnetic reconnection. A significant uncertainty is presented by the spectrum and type of the initial perturbations that cause the instabilities to grow. Generally, it is more likely that the evolution of KH waves is faster because the mode represents an ideal instability which implies always fast growth on the time scale of ideal MHD. In comparison, fast magnetic reconnection requires first a thin current layer and then develops on the time scale of the Petschek rate. However, the details are more complicated because large scale KH waves also have a slower evolution than short wavelength modes. To cover these possibilities, I consider first a situation with perturbations that favor KH growth over reconnection in Chapter 5 and then consider a scenario with perturbations that favor the evolution of magnetic reconnection as the primary process in Chapter 6.

Since all these studies are based on numerical simulation, an introduction of the numerical method is provided in Chapter 2. In Chapter 7, I summarize the results and discuss remaining problems and future work.
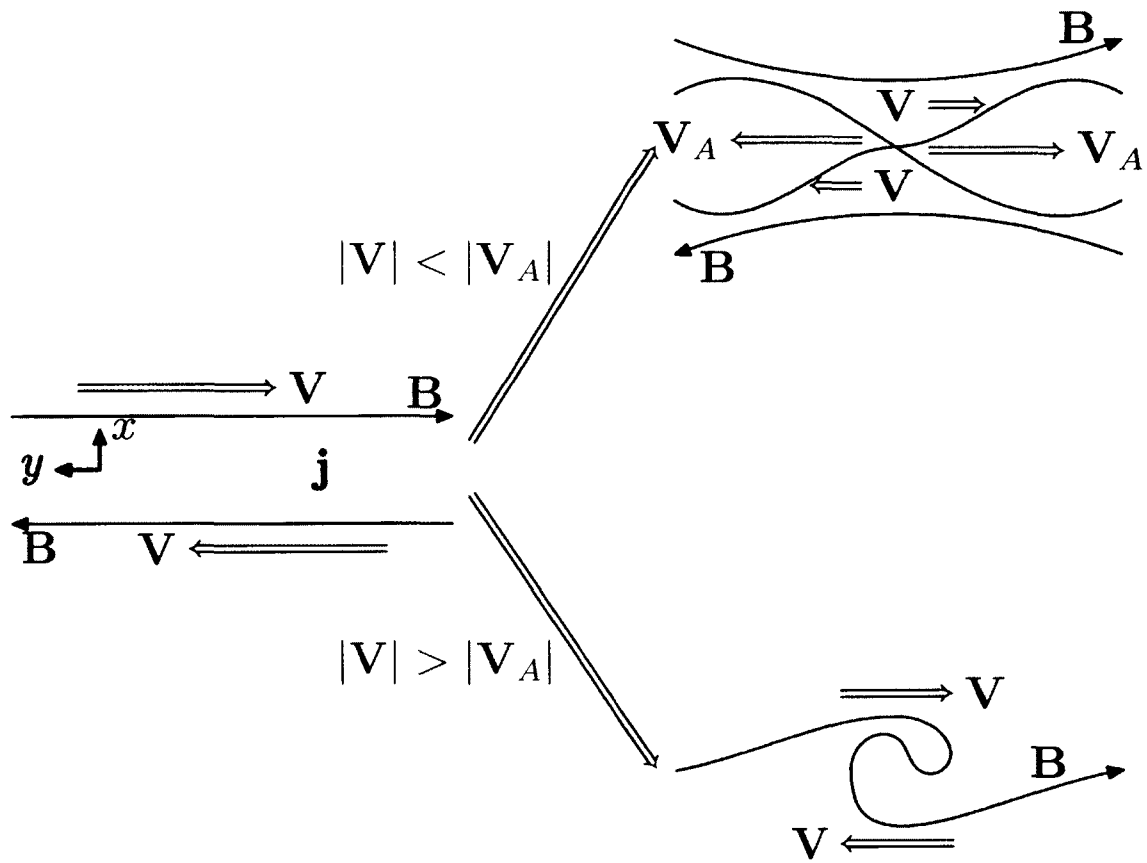
Figure 1.8: For $\mathbf{k} \parallel \mathbf{B}$, magnetic reconnection operates only when $|\mathbf{V}| < |\mathbf{V}_A|$.

Chapter 2
Numerical Methods
2.1   Numerical Integration of the MHD and Hall MHD Equations

In this thesis, I use a leapfrog scheme to solve the full set of normalized resistive Hall MHD equations [*Otto*, 1990]:

$$\frac{\partial \rho}{\partial t} = -\nabla \cdot (\rho \mathbf{V}), \tag{2.1}$$

$$\frac{\partial \rho \mathbf{V}}{\partial t} = -\nabla \cdot \left[\rho \mathbf{V}\mathbf{V} + \frac{1}{2}\left(p - B^2\right)\mathbf{I} + \mathbf{B}\mathbf{B} \right], \tag{2.2}$$

$$\frac{\partial \mathbf{B}}{\partial t} = \nabla \times \left[\left(\mathbf{V} - l\frac{\mathbf{j}}{\rho} \right) \times \mathbf{B} - \eta \mathbf{j} \right], \tag{2.3}$$

$$\frac{\partial h}{\partial t} = -\nabla \cdot (h\mathbf{V}) + \frac{\gamma - 1}{\gamma} h^{1-\gamma} \eta j^2, \tag{2.4}$$

$$h = (p/2)^{1/\gamma}, \tag{2.5}$$

$$\mathbf{j} = \nabla \times \mathbf{B}, \tag{2.6}$$

where all the notations have the same meaning as in Chapter 1.

The leapfrog scheme is given by introducing centered differences in both time and space. Figure 2.1 shows an example of the numerical integration of the continuity equation in one dimension using a finite differences leapfrog scheme. For instance the discretized continuity equation becomes with $\rho V_x = F$,

$$\frac{\rho_i^{n+1} - \rho_i^{n-1}}{2\Delta t} = -\frac{F_{i+1}^n - F_{i-1}^n}{2\Delta x}, \tag{2.7}$$

which as an algorithm becomes

$$\rho_i^{n+1} = \rho_i^{n-1} - \frac{\Delta t}{\Delta x}\left(F_{i+1}^n - F_{i-1}^n\right). \tag{2.8}$$

Equation (2.8) is consistent with the continuity equation with a truncation error of $\mathcal{O}\left(\Delta t^2, \Delta x^2\right)$. Note, that a Taylor expansion of the discretized terms implies that a first order error in Δx corresponds to a second order derivative of ρ, i.e., to diffusion and the second order error to a third order derivative in ρ. Therefore, the achieved

accuracy implies low diffusion (no second order derivative error) and that the leading error term corresponds to numerical dispersion. The property of low numerical diffusion is an important advantage for magnetic reconnection simulation, because resistive diffusion is critical to magnetic reconnection, but whose magnitude is often small $\mathcal{O}(0.01 \sim 0.1)$. Thus a low numerical diffusion is required to avoid physical diffusion being masked by numerical diffusion. This also implies that the leading error term generates numerical dispersion and oscillations close to the grid scale. To overcome these, a small numerical viscosity has been applied on the grid scale in the simulation code.
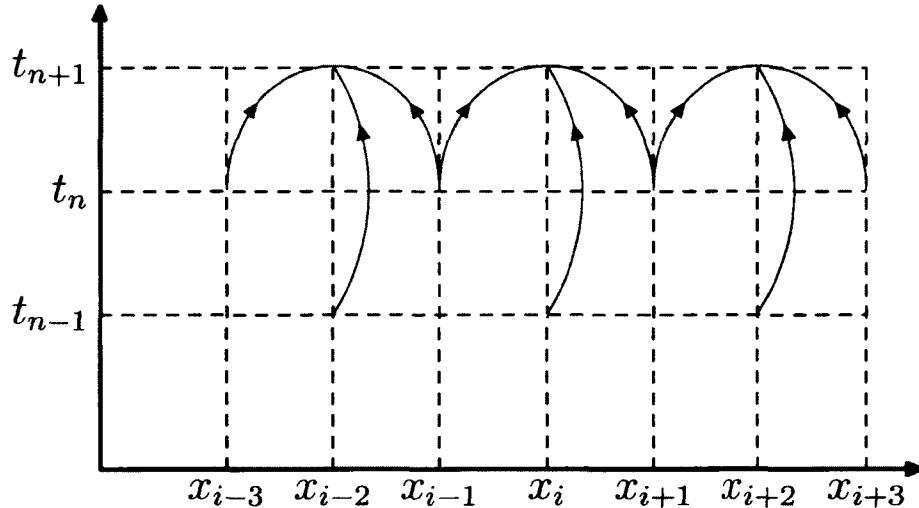
Figure 2.1: Leapfrog scheme.

Equation (2.8) shows that the update of ρ_i^{n+1} is independent of the information at grid point $x = x_i$ at $t = t_n$. Thus, the update of all orange points does not require any information of the blue points at all. In fact, the scheme can be executed (and is executed) without any information from the blue points at all integration steps without losing any accuracy. It is only required to integrate every other grid point

initially by a simple time step and to execute another simple time step integration at the very end of the numerical integration to bring all grid points to the same time level. However, the inclusion of the Hall term requires the information of $\mathbf{B}_i^n$, which can be obtained either by taking the average of the neighbor points at $t = t_n$ or by using a Lax integration scheme (forward differences in time and centered differences in space). The second method is more stable than the first method in the three-dimensional simulation. Therefore, this is applied in my code.

To avoid numerical instabilities, the time step $\Delta t_n = t_{n+1} - t_n$ is limited by the Courant–Friedrichs–Lewy (CFL) condition [Courant et al., 1967]:

$$\Delta t_n < \min \left(\left| \frac{x_i^n - x_{i-1}^n}{V_i^n} \right| \right) , \tag{2.9}$$

where V_i^n is the group velocity for the system at the grid point $x = x_n$ at $t = t_n$. In other words, the CFL condition (2.9) requires the numerical scheme to resolve the transport of information along neighboring grid points. For the MHD equations, the fastest wave mode (the fast mode) is a non-dispersive wave, whose group velocity is $V_f = \sqrt{c_s^2 + V_A^2}$, where c_s is the ion acoustic speed and V_A is the Alfvén speed. Thus for a three-dimensional cube with N^3 grid points, the computational effort is proportional to $\mathcal{O}(N^4)$. However, the whistler wave introduced by the Hall physics is a dispersive wave ($V = \partial \omega / \partial k \sim k \sim \Delta x^{-1}$). Thus for same Δx, the computational effort increases significantly and scales with $\mathcal{O}(N^5)$.

2.2 Initial and Boundary Conditions

2.2.1 Two-dimensional Configurations

In all of the simulations, the initial equilibriums is always a modified one-dimensional Harries sheet. The initial equilibrium for the two-dimensional configurations is illustrated in Figure 2.2. I assume the x direction normal to the current layer (boundary), y is direction along the boundary, and z is along the invariant direction. The simulation domain is a box with $|x| \leq L_x$, and $0 \leq y \leq L_y$. This choice is used in the two-dimensional studies presented in Chapter 3 and 4. The initial equilibrium is a

one-dimensional current sheet, which is given by

$$B_x = 0, \tag{2.10}$$

$$B_y = \tanh(x), \tag{2.11}$$

$$B_z = B_g, \tag{2.12}$$

$$V_x = 0, \tag{2.13}$$

$$V_y = 0, \tag{2.14}$$

$$V_z = V_{zi} \tanh(x), \tag{2.15}$$

$$p = p_\infty + 1 - B_y^2, \tag{2.16}$$

$$\rho = \rho_0 + \delta\rho \tanh(x), \tag{2.17}$$

where the parameters B_g, V_{zi}, and $\delta\rho$ are used to introduce a guide field, flow shear, and density asymmetry. In this study, magnetic reconnection is triggered by the localized resistivity model

$$\eta = \eta_0 \exp(-t/t_0) / [\cosh(x)\cosh(y)] + \eta_b, \tag{2.18}$$

where $\eta_0 = 0.05$, $t_0 = 3$, and $\eta_b = 0.002$ is a background resistivity to smooth the numerical dispersion.

Free boundary conditions ($\partial_n = 0$, where ∂_n is the partial derivative in the direction normal to the boundary) are applied to the x maximum and minimum boundary and y maximum boundary. The y minimum boundary is determined by symmetry properties of the (Hall) MHD equations [*Otto et al.*, 2007].

2.2.2 Three-dimensional Configurations

The initial equilibrium for the three-dimensional configurations is illustrated in Figure 2.3. I assume x normal to the current layer (boundary), z is chosen along the anti-parallel magnetic field components on the two sides of the current layer, and
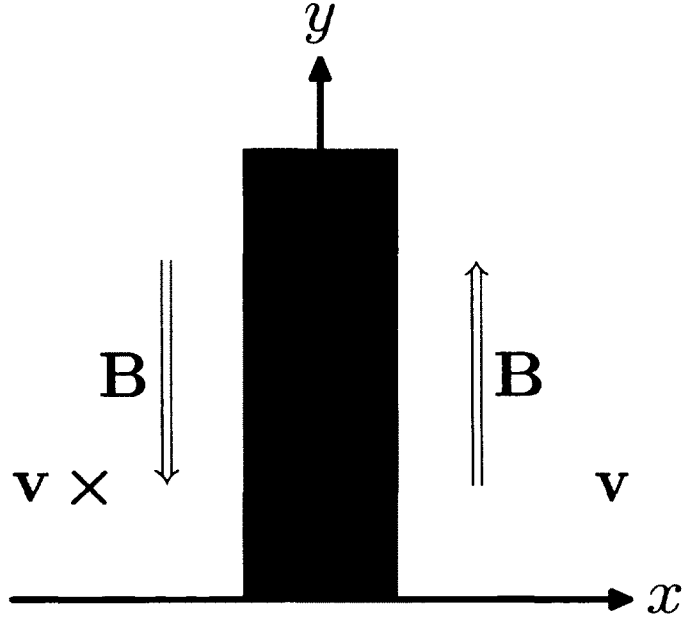
Figure 2.2: Harries sheet in two-dimensional configurations.

y completes the right-handed coordinate system. The simulation domain is a volume with $|x| \leq L_x$, $|y| \leq L_y$, and $|z| \leq L_z$. The initial equilibrium is a modified one-dimensional Harries sheet. For example, in the three-dimensional simulations (Chapter 5 and 6), it is given by

$$B_x = 0, \tag{2.19}$$

$$B_y = B_{y0}, \tag{2.20}$$

$$B_z = -B_{z0}\tanh(x), \tag{2.21}$$

$$V_x = 0, \tag{2.22}$$

$$V_y = -V_{y0}\tanh(x), \tag{2.23}$$

$$V_z = 0, \tag{2.24}$$

$$p = p_\infty + 1 - B_z^2, \tag{2.25}$$

$$\rho = \rho_0 + \delta\rho\tanh(x), \tag{2.26}$$

where B_{z0} is the anti-parallel magnetic field component, p_∞ is the inflow plasma thermal pressure, ρ_0 is the average plasma density, and $\delta\rho$ the plasma density difference between magnetosphere and magnetosheath. B_y represents the guide field and V_{y0} is the magnitude of the shear flow.
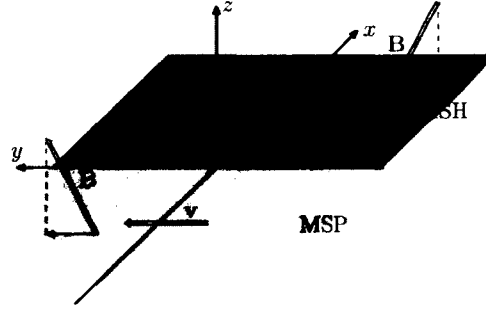
Figure 2.3: Harries sheet in three-dimensional configurations.

In order to select the KH mode as the primary process, the system is triggered by a KH type perturbation in Chapter 5, which is chosen as

$$\delta\mathbf{v} = [\nabla\Psi\,(x,y) \times \hat{\mathbf{e}}_z]\,f_1\,(z)\,, \tag{2.27}$$

where

$$\Psi\,(x,y) = -\,(\delta v/n)\cos\,(ky)\tanh\,(kx)\,, \tag{2.28}$$

$\delta v = 0.2$, n is the number of the KH modes in the system, and $k = n\pi L_y^{-1}$ is wave number. The function f_1 is given by

$$f_1\,(z) = \frac{1}{2}\left[\tanh\left(\frac{z+z_0}{d}\right) - \tanh\left(\frac{z-z_0}{d}\right)\right]\,, \tag{2.29}$$

which is chosen to localize the perturbation in the region where $z < |z_0|$. Note, that this perturbation is not a normal mode, i.e., a solution of the linearized equation, but the spectrum of the perturbation has a dominant contribution to the normal mode with the chosen wave number.

In order to select magnetic reconnection as the primary process in Chapter 6, the system is triggered by a magnetic perturbation which is chosen as

$$\delta \mathbf{B} = [\nabla A\,(x,z) \times \hat{\mathbf{e}}_y]\, f_2\,(y)\,, \tag{2.30}$$

where

$$A\,(x,z) = \delta B \cosh^{-2}(x) \cosh^{-2}(z/2)\,, \tag{2.31}$$

$\delta B = 0.5$. The function f_2 is given by

$$f_2\,(y) = \frac{1}{2}\tanh^{-1}\left(\frac{y_0}{d}\right)\left[\tanh\left(\frac{y+y_0}{d}\right) - \tanh\left(\frac{y-y_0}{d}\right)\right]\,, \tag{2.32}$$

which is chosen to localize the perturbation in the region where $y < |y_0|$. The relatively large magnetic perturbation is justified because large perturbations are common in the magnetosheath and a large perturbation accelerates the evolution of reconnection as the primary instability in this study.

The simulations use periodic boundary conditions along the y direction, which is the direction of the dominant $\mathbf{k}$ vector of the KH modes. Free boundary $\partial_x = 0$ conditions are applied in the x direction. However, the simulation box is chosen sufficiently wide that these boundary effects can be ignored. An artificial friction term $-\nu\,(z)\,[\rho\mathbf{V} - \rho\,(0)\,\mathbf{V}\,(0)]$ is added on the right-hand side of the momentum equation (2.2), where $\rho\,(0)$, and $\mathbf{V}\,(0)$ are the initial plasma density and velocity, respectively. The friction coefficient is localized near the z boundary and given by

$$\nu\,(z) = \frac{\nu_0}{2}\left[2 - \tanh\left(\frac{z+z_\nu}{dz_\nu}\right) + \tanh\left(\frac{z-z_\nu}{dz_\nu}\right)\right]\,, \tag{2.33}$$

$\nu_0 = 1$, $z_\nu = 0.75 L_z$, and $dz_\nu = 3$. This form of the friction term introduces a magnetic line tying on either side of magnetopause close to the z boundaries to mimic the fact that the magnetosheath magnetic field lines are moving with the solar wind, and that magnetospheric magnetic field footprints stick to the Earth's ionosphere (i.e., at large distances from the equatorial plane).

2.3 Numerical Method for Reconnected Flux and Reconnection Rate

2.3.1 Two-dimensional Configurations

Considering two-dimensional magnetic reconnection as illustrated in Figure 2.4, the magnetic field **B** can be represented as

$$\mathbf{B} = \nabla \times (A_z \hat{\mathbf{e}}_z) + B_z \hat{\mathbf{e}}_z = \nabla A_z \times \hat{\mathbf{e}}_z + B_z \hat{\mathbf{e}}_z, \tag{2.34}$$

where A_z is z component of the vector potential. The X $(x_1(t), y_1(t))$ and O $(x_0(t), y_0(t))$ points are the positions where $B_x = B_y = 0$. The reconnected flux is the magnetic flux between these two points, i.e.,

$$\Phi = \int_{y_0}^{y_1} B_x dy = A_z(x_0, y_0) - A_z(x_1, y_1). \tag{2.35}$$

The reconnection rate is defined as the rate with which the amount of magnetic flux changes:

$$r = \frac{d\Phi}{dt} = \frac{d}{dt}[A_z(x_0, y_0) - A_z(x_1, y_1)]. \tag{2.36}$$

This reconnection rate can be determined directly by applying the induction equation, since the electric field along z direction is given by

$$E_z = -\frac{dA_z}{dt} = V_y B_x - V_x B_y + \eta j_z. \tag{2.37}$$

At the X and O point $B_x = B_y = 0$, such that the reconnection rate is given by

$$r = \eta(x_0, y_0) j_z(x_0, y_0) - \eta(x_1, y_1) j_z(x_1, y_1). \tag{2.38}$$

Note, that Equation (2.36) and (2.38) provide two independent means to measure the reconnection rate, which can be used as a simple test to examine the influence from numerical diffusion.

O point (x_0, y_0)
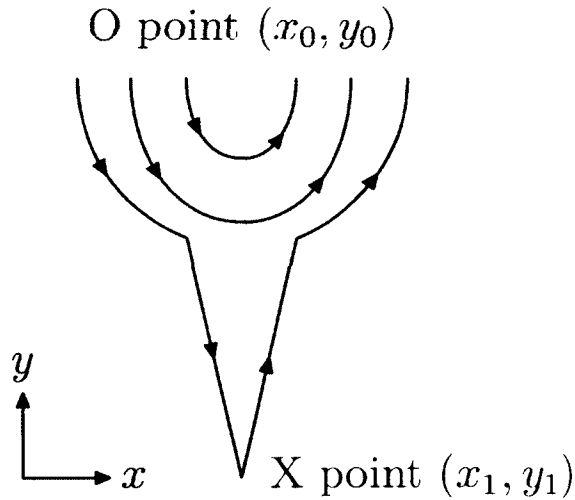
Figure 2.4: Two-dimensional magnetic reconnection.

2.3.2 Three-dimensional Configurations

Figure 2.5 presents a sketch of the three-dimensional reconnection process. To identify the reconnected (open) magnetic flux, field lines are traced from the top boundary ($z = L_z$). The open or reconnected field lines from the top boundary on the magnetosheath side ($x > 0$) extend toward the equatorial plane, and connect to the field lines on the magnetosphere side, which extend back to the top boundary because the field magnetospheric field has the opposite direction along z. Thus, all open field lines started from the top boundary on the magnetosheath side ($x > 0$) have endpoints also at the top boundary on the magnetosphere side ($x < 0$). By integrating all of the positive (or negative) open flux (along z) at the top boundary, one can obtain the total reconnected flux

$$\Phi = \frac{1}{2} \int_{\text{open}} |B_z (x, y, L_z)| \, dxdy, \tag{2.39}$$

where the integral is taken over the open flux at the top boundary plane. Note, that this method requires a sufficient density of field line integrations for good accuracy. The total reconnection rate is given by the time derivative of this magnetic flux.

In order to compare this rate with the two-dimensional reconnection theory, the reconnection rate is normalized to the system size $2L_y$, such that the normalized reconnection rate r or reconnection rate per unit distance is defined by

$$r = \frac{1}{2L_y}\frac{d\Phi}{dt}.$$

(2.40)

I also remark that the net rate of change of magnetic flux through a closed contour is the line integral of the tangential electric field along the closed contour. However, this method is not applicable here because this net change is zero for the $x = 0$ plane because the same amounts of reconnected magnetic flux are connected to the northern and southern hemisphere and therefore cancel. Another measure for the rate of the total flux reconnection is given by the maximum of the integrated parallel electric field in the system. While this is a rigorous measure, it is difficult to determine in a numerical system because this maximum is assumed for one (singular) magnetic field line. Even a very small deviation from this singular field line can yield a significant difference of the integrated electric field and therefore produce a large uncertainty of the actual reconnection rate.
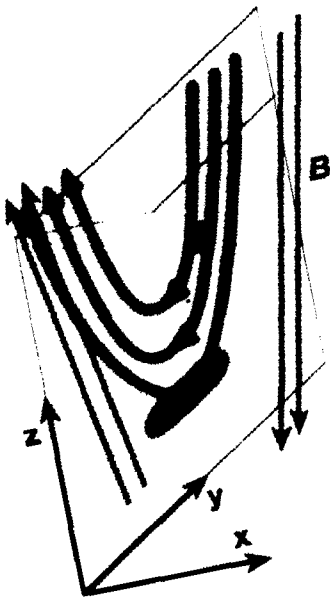
Figure 2.5: Sketch of three-dimensional reconnection process.

Chapter 3
Nonadiabatic Heating in Magnetic Reconnection
3.1 Introduction

Magnetic reconnection is a fundamentally important process in space physics, because it converts the stored magnetic energy into the kinetic energy, and it changes the magnetic topology such that plasma can be transported across magnetic boundaries [*Dungey*, 1961; *Parker*, 1957; *Sweet*, 1958]. It occurs in the presence of sufficiently large anti-parallel magnetic field components. At the dayside magnetopause, magnetic reconnection is the prime mechanism for a transfer of magnetic flux and energy into the magnetosphere during periods of southward interplanetary magnetic field (IMF). During times of northward IMF, magnetic reconnection occurs at higher latitudes. The concept of magnetic reconnection is based on the breakdown of the so-called "frozen-in" condition. In Petschek's reconnection model [*Petschek*, 1964] the frozen-in condition breaks in a tiny diffusion region, which is bound by in- and outflow regions. The in- and outflow regions are separated by two pairs of slow shocks (see Figure 3.1), where the plasma is mostly accelerated by the $\mathbf{j} \times \mathbf{B}$ force and magnetic energy is converted into bulk and thermal energy.

This energy conversion is one of the most important aspects of magnetic reconnection. This process can also be considered as a nonadiabatic process, which can be characterized by so-called "specific entropy" $S = p/\rho^{\gamma}$, where p is the plasma thermal pressure, ρ is the plasma density, and $\gamma = 5/3$ is the ratio of specific heats [*Birn et al.*, 2006, 2009]. Hereafter, I simply refer to this quantity as entropy. Note, that a value of $\gamma = 5/3$ corresponds to three degrees of freedom for the motion of charged particles. In the MHD description, entropy is an invariant in the absence of Ohmic or viscous heating and shocks. Nevertheless, in the context of magnetic reconnection, the breakdown of ideal MHD by local dissipation also implies a breakdown of the entropy conservation. A significant entropy increase in Petschek's model is provided by the two pairs of slow shocks bounding the outflow regions. These represent the major entropy sources, as will be demonstrated in this study for different types of
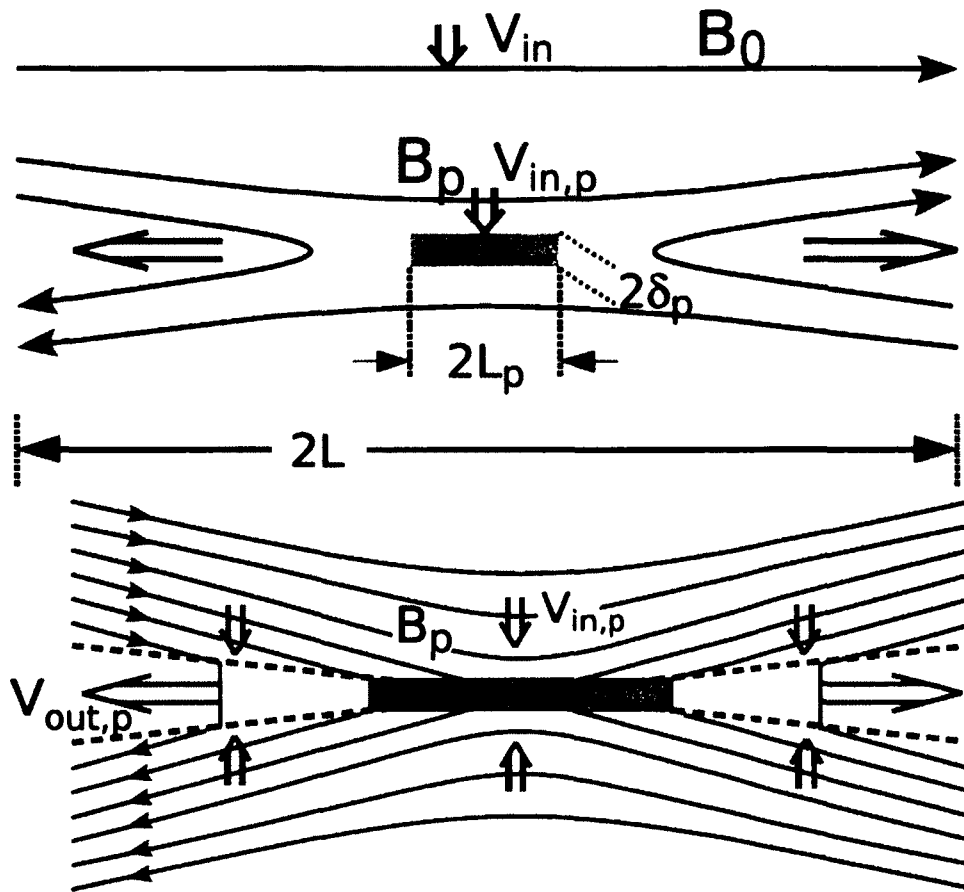
Figure 3.1: Illustration of the Petschek reconnection geometry. Top: Length scales assumed in Petschek's model; Bottom: Illustration of the diffusion region and the attached slow shocks [*Otto*, 2012].

reconnection geometries.

It is believed that magnetic reconnection is the dominant process for southward IMF conditions. For northward IMF conditions, reconnection driven by nonlinear Kelvin-Helmholtz (KH) modes at the low-latitude boundary layer (LLBL) and high-latitude reconnection become more important [*Scholer and Treumann*, 1997]. On the other side, satellite observations show that ions in the Earth's plasma sheet become cold and dense during prolonged periods of northward IMF, which has been attributed to the massive transport of the solar wind or magnetosheath ions into the plasma sheet [*Fujimoto et al.*, 1997]. There are two components of plasma in this cold dense plasma sheet, a hot distribution, which is considered a remnant of the original plasma sheet plasma, and a cold distribution, which is believed to be of magnetosheath origin [*Wang et al.*, 2007]. The typical flank magnetosheath ion density and temperature for fast solar wind conditions are about 5 cm^{-3} and 50 eV. For slow solar wind conditions, the ion density and temperature are about 8 cm^{-3} and 10 eV [*Borovsky and Cayton*, 2011]. Density and temperature for the cold plasma component are about 0.5 cm^{-3} and 500 eV [*Wang et al.*, 2007], which yield an entropy increase of about $1 \sim 2$ orders of magnitude compared to the magnetosheath. Therefore, the plasma entry process is accompanied with strong nonadiabatic heating. One may expect that this nonadiabatic heating is mainly caused by magnetic reconnection, because reconnection is believed to be the prime mechanism for this entry process. However, studies by *Birn et al.* [2006, 2009] demonstrated that entropy appears more or less unchanged after reconnection. This raises the important question, whether magnetic reconnection can provide any significant nonadiabatic heating? Directly related is the issue of any specific conditions, for which significant nonadiabatic heating may occur.

Here I present a systematic study of the entropy changes in magnetic reconnection based on analytical theory and numerical MHD simulation. The numerical methods are introduced in Section 3.2. In Section 3.3, I discuss entropy sources in different sub-regions in a Petschek type reconnection geometry. For applications to the actual magnetospheric boundary, the influence of a guide field, the asymmetry, and the shear

flow are discussed in Section 3.4. Section 3.5 presents a summary and discussion.

3.2 Numerical Model

The MHD description is suitable for the magnetospheric boundary on scales larger than the ion inertia length. However, after reconnection onset, the thin diffusion region develops to typical length scales comparable to the ion and electron inertia scale. In this study, I solve the full set of the one- and two-dimensional normalized resistive MHD and Hall MHD equations as introduced in Chapter 2, except using the energy equation instead of the entropy equation. By combing Equation (2.1)-(2.4), one can derive the energy equation:

$$\frac{\partial w}{\partial t} = -\nabla \cdot \left\{ \left[w + \frac{1}{2}\left(p + B^2\right)\right]\mathbf{V} - \left[(\mathbf{V} - \mathbf{u})\cdot\mathbf{B}\right]\mathbf{B} + \eta\mathbf{j}\times\mathbf{B} - B^2\mathbf{u}\right\}, \qquad (3.1)$$

where $w = \left[\rho v^2 + B^2 + p/\left(\gamma - 1\right)\right]/2$ is the total energy density of the plasma, and $\mathbf{u} = l\left(\mathbf{j}/\rho\right)$. One should keep in mind, in this normalization, the unit-less entropy is $S = p/\left(2\rho^\gamma\right)$. The difference between the energy equation and the entropy equation will be discussed in Section 3.3.1.1.

I present the results from four selected two-dimensional simulations to study the entropy enhancement for typical magnetic reconnection configurations using a symmetric reference case and including characteristic variations in terms of the magnetic field, plasma flow, and symmetry of the configuration. The simulation domain is a rectangular box with $|x| \leq 20$, and $0 \leq y \leq 80$, and is resolved by using 323×353 grid points with a non-uniform grid in the both directions. To sufficiently resolve the diffusion region, the best resolution is set to 0.025 and 0.1 in the x and y direction in the diffusion region. Free boundary conditions ($\partial_n = 0$, where ∂_n is the partial derivative in the direction normal to the boundary) are applied to the x maximum and minimum boundary and y maximum boundary. The y minimum boundary is determined by symmetry properties of the (Hall) MHD equations [*Otto et al.*, 2007].

The initial equilibrium is a one-dimensional modified Harries sheet given by

$$B_x = 0, \tag{3.2}$$

$$B_y = \tanh(x), \tag{3.3}$$

$$B_z = B_g, \tag{3.4}$$

$$V_x = 0, \tag{3.5}$$

$$V_y = 0, \tag{3.6}$$

$$V_z = V_{zi} \tanh(x), \tag{3.7}$$

$$p = p_\infty + 1 - B_y^2, \tag{3.8}$$

$$\rho = \rho_0 + \delta\rho \tanh(x), \tag{3.9}$$

where the parameters B_g, V_{zi}, and $\delta\rho$ are used to introduce a guide field, flow shear, and density asymmetry. The values of all parameters are listed in Table 3.1. To trigger Petschek type magnetic reconnection (except case B), I use a localized resistivity given by

$$\eta = \eta_0 \left[1 - \exp\left(-t/\tau\right)\right] \cosh^{-1}(x) \cosh^{-1}(y) + \eta_b, \tag{3.10}$$

where $\eta_0 = 0.05$, $\tau = 5$, and $\eta_b = 0.002$.

Case A is the reference case. At the real magnetopause, the magnetosheath density is about ten times larger than the magnetospheric density. Therefore, to investigate this asymmetry effect is of importance. In the simulation (case B), I set $p_\infty = 0.025$, $\rho_0 = 1.5$, and $\delta\rho = 0.5$, which yields to $\rho_{\mathrm{MSP}} : \rho_{\mathrm{MSH}} = 1 : 2$, where ρ_{MSP} refers to the magnetosphere ($x < 0$) density, and ρ_{MSH} is the magnetosheath ($x > 0$) density. I only localized the resistivity along the y direction, because the diffusion region may move along the x direction:

$$\eta = \eta_0 \left[1 - \exp\left(-t/\tau\right)\right] \cosh^{-1}(y) + \eta_b. \tag{3.11}$$

At dayside magnetopause, a guide field or a large perpendicular shear flow is always present. These configurations are investigated in the cases C and D.

Table 3.1: Values of the simulation parameters

Case	ρ_0	$\delta\rho$	B_g	V_{zi}	p_∞
A	1	0	0	0	0.1
B	1.5	0.5	0	0	0.025
C	1	0	1	0	0.1
D	1	0	0	0.5	0.1

3.3 Symmetric Petschek Reconnection

Figure 3.2 shows the thermal pressure p (left panel) in Case A, at $t = 150$. In the inflow region, the pressure is about 0.1 (the reddish region in Figure 3.2), which yields an initial inflow region plasma beta β of 0.1. In the outflow region, the pressure increases to about unity (the greenish region in Figure 3.2). Black lines are magnetic field lines (contours for the z component of the vector potential). The strongly bend magnetic field lines in the transition region between inflow and outflow region indicate the existence of a large current density. Black arrows represent the flow velocity $\mathbf{V}$. The inflow velocity only has a normal component (x direction) with a relatively small magnitude, and it carries flux into the outflow region. The fast jetting plasma in the outflow region reaches the inflow Alfvén speed, which indicates that reconnection is well developed. There are three sub-regions can be identified in the outflow region. The diffusion region is located at the origin ($x = y = 0$), and it is barely visible in Figure 3.2, which is consistent with the assumption of a small diffusion region in Petschek's model. The steady outflow region is bounded by a pair of slow shocks, at $y < 50$ in Figure 3.2. And the non-steady bulge region is at $y > 50$ in Figure 3.2.

3.3.1 The Dominant Entropy Source: Slow Shocks at the Steady Outflow Region

The transition between the inflow and the outflow region is almost one-dimensional, because the angle of the shocks with the y axis is small, and the transition represents
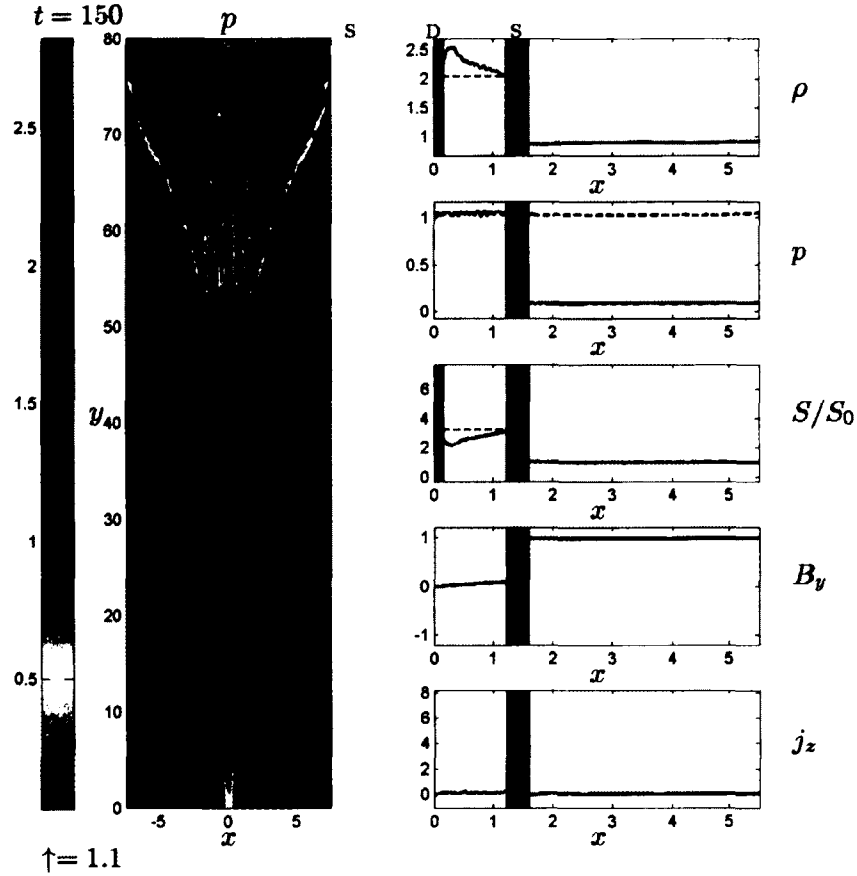
Figure 3.2: The left panel shows the thermal pressure p at $t = 150$. Black lines are the magnetic field lines (contours for the z component of the vector potential), and black arrows indicate the flow velocity $\mathbf{V}$. The five panels on the right side show the profiles of the plasma density ρ, thermal pressure p, normalized entropy S/S_0, magnetic field B_y component, and current density j_z component, which are taken from the blue line in the left panel. The red dashed lines are the results from the Rankine-Hugoniot (RH) relations. The black dashed line is the total pressure $p + B^2$. The slow shock and density depletion layer are shaded in gray and labeled S and D, respectively.

the matching of the two asymptotic plasma conditions of the inflow regions by MHD waves and discontinuities (the so-called "Riemann problem" [*Lin and Lee*, 1993]). I take a cut where it is indicated by the blue line in the left panel of Figure 3.2, and present the results on the right side of Figure 3.2. Due to the symmetry, I only show the $x \geq 0$ part of the cut. The five panels on the right side show the profiles of the plasma density ρ, thermal pressure p, normalized entropy S/S_0, the y component of the magnetic field B_y, and the z component of the current density j_z, here $S_0 = 0.05$ is the inflow region entropy. The depletion of the density in the vicinity of the y axis, (shaded in gray and labeled as D in Figure 3.2) is a contact discontinuity and its cause will be discussed in the Section 3.3.2. The large current density is consistent with the switch off of the magnetic field, which indicates that these are the slow switch-off shock layers. These shock layers are shaded in gray and labeled S in Figure 3.2. The plasma density ρ, thermal pressure p, and entropy S strongly increase through the shock layers, while the total $p + B^2$ (black dashed line in the pressure plot) remains constant across the shock layers.

The properties of the slow switch-off shock can be described by the so-called "Rankine-Hugoniot (RH) relations", which are inferred from Equation (2.1) - (2.3), and (3.1) with homogeneous assumption for both upstream and downstream. Here I list the compression ratio, the ratio of down- and upstream pressure and the corresponding ratio of the entropy for slow switch-off shocks:

$$\frac{\rho_d}{\rho_u} = 1 + \frac{1}{\gamma\beta + \gamma - 1}, \tag{3.12}$$

$$\frac{p_d}{p_u} = \frac{\rho_d}{\rho_u}\left(1 + \frac{\gamma - 1}{\gamma\beta}\right), \tag{3.13}$$

$$\frac{S_d}{S_u} = \left(\frac{\rho_d}{\rho_u}\right)^{1-\gamma}\left(1 + \frac{\gamma - 1}{\gamma\beta}\right), \tag{3.14}$$

where the index d and u indicate the down-steam and upstream, respectively, $\beta = p_u/B_u^2$ is the upstream plasma beta. Figure 3.3 presents the compression ratio ρ_d/ρ_u, the ratio of down- and upstream pressure p_d/p_u, and the corresponding ratio of the

entropy S_d/S_u as a function of β by using dash-dotted, dashed, and solid lines, respectively. Note that all the ratios increase with decreasing plasma beta β, and the maximum plasma compression is 2.5, which means that the plasma entropy can increase significantly if the upstream plasma beta β is sufficiently small. For $\beta < 10^{-2}$, the entropy ratio between out- and inflow regions S_d/S_u is greater than 20.

To compare the theoretical results with the two-dimensional simulation results, I labeled the downstream results from the RH relations by red lines in Figure 3.2. It shows that right after slow shock (downstream region), all quantities are consistent with the theoretical results, although, density increases further deeper into the outflow region. This is possibly because that fluid elements deeper in the outflow region have entered much closer to the diffusion region at a location or time when the slow shock had not been fully developed. I carry out a one-dimensional simulation of the Riemann problem. This has the advantage of much higher resolution and short execution times. In this study, one-dimensional simulations are also used to compare the influence of different forms of the energy equation which closes the MHD equations.

3.3.1.1 Difference between energy equation and entropy equation

The slow shock transition can be simulated in a one-dimensional configuration by adding a small constant B_n component in the Harries sheet. Figure 3.4 presents the results from the one-dimensional simulation with the Hall parameter $l = 0$ (switch-off the Hall effect), and the upstream plasma beta $\beta = 0.1$. The three panels show the density ρ (top), the thermal pressure p (middle), and the entropy S (bottom). The dashed and dash-dotted lines are the simulation results by using the entropy equation and energy equation, respectively. As a reference, the theoretical results from the RH relations (Equation (3.12)-(3.14)) are labeled by the solid lines. For convenience, I transformed the system to the shock frame. Thus $x > 0$ is the upstream (inflow region) and $x < 0$ is the downstream (outflow region). Figure 3.4 shows that energy conservation yields correct jump relations, however, using the entropy equation generates an artificial density enhancement and an insufficient entropy increase.

Slow switch-off shock ratio of density, pressure, and entropy
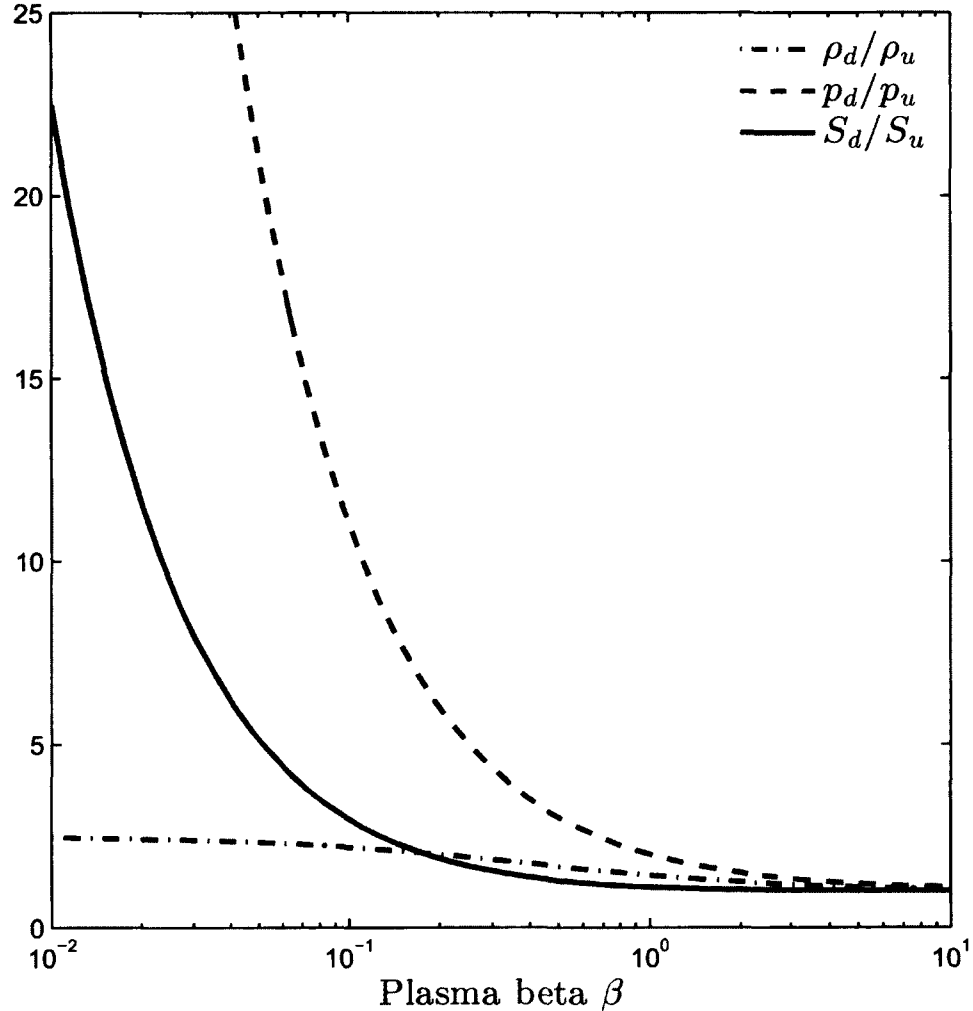
Figure 3.3: The ratio of downstream and upstream density ρ_d/ρ_u (dot-dash line), pressure p_d/p_u (dash line) and entropy S_d/S_u (solid line) as a function of plasma beta (β) for the slow switch-off shock.

Clearly energy and entropy conservations generate different shock properties in ideal MHD. The entropy increase through the shock is due to the energy conservation and does not require explicit Ohmic heating. However, the entropy equation main-
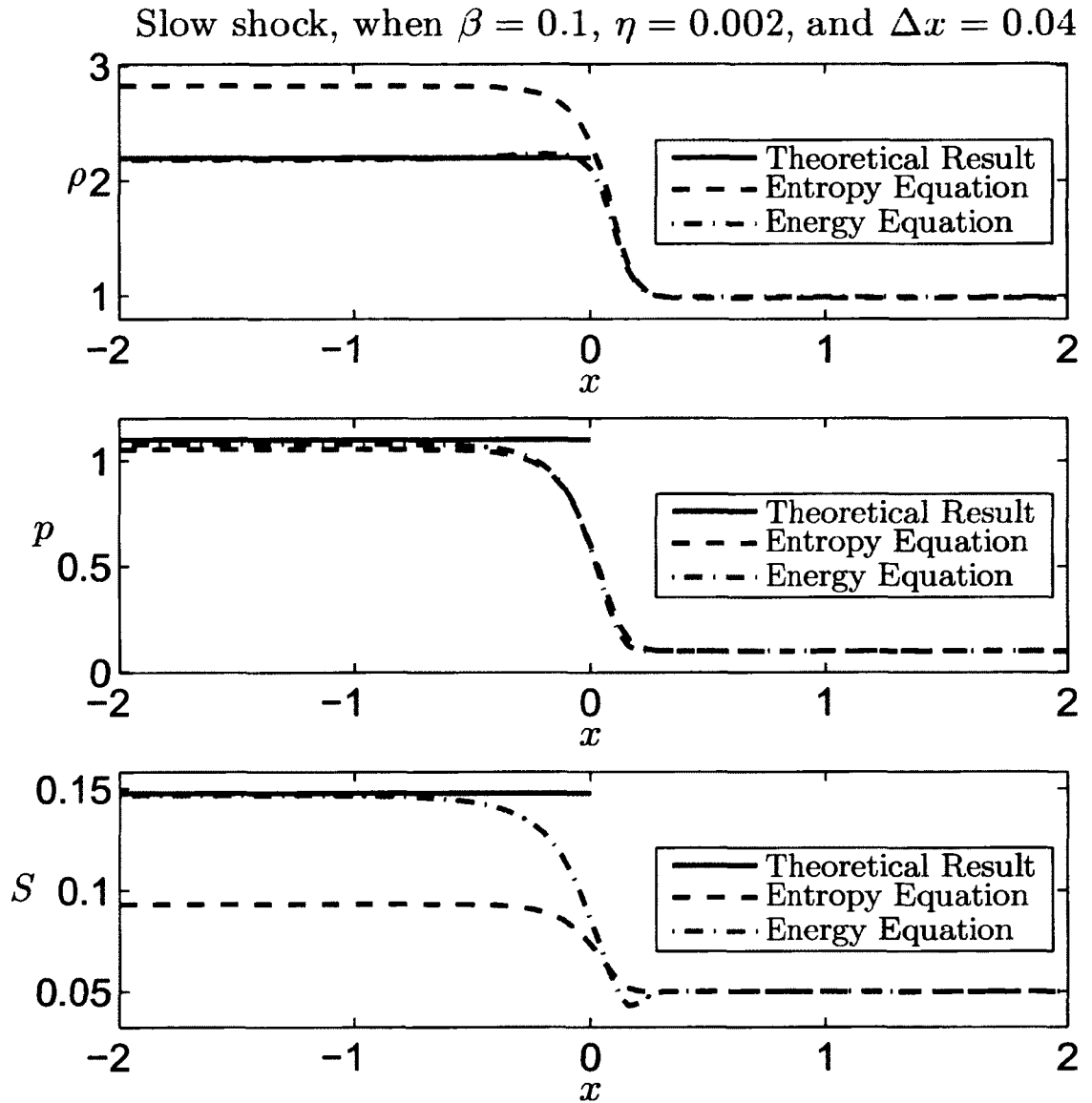
Figure 3.4: MHD slow shocks with upstream plasma beta $\beta = 0.1$, and $\Delta x = 0.04$. The three panels show the density ρ (top), the thermal pressure p (middle), and the entropy S (bottom). The dashed and dash-dotted lines are the simulation results by using the entropy equation and energy equation, respectively. As the reference, the theoretical results from the RH relations are indicated by the solid lines.

tains the entropy conservation and the resulting "slow shock equivalent" discontinuity is violating energy conservation. For resistive MHD ($\eta \neq 0$), the entropy equation allows entropy to increase through Ohmic heating. This can be shown clearly by combining the entropy equation and the continuity equation, which yields to

$$\frac{dS}{dt} = \frac{d}{dt}\left(\frac{p}{2\rho^\gamma}\right) = (\gamma - 1)\frac{\eta j^2}{\rho^\gamma}, \tag{3.15}$$

where $d/dt = \partial_t + \mathbf{V} \cdot \nabla$. Equation (3.15) indicates that a correct approximation to the slow shock solution is possible in the presence of sufficient Ohmic heating, which requires a very high resolution of the boundary between in- and outflow region in a numerical simulation. One can estimate the width of this resistivity layer δ by integrating both sides of Equation (3.15)

$$\Delta S = (\gamma - 1)\frac{\eta j^2}{\rho^\gamma}\Delta t, \tag{3.16}$$

where $\Delta S = S_d - S_u \approx S_d = p_d\rho_d^{-\gamma}/2 = \rho_d^{-\gamma}/2$, $\rho = \rho_d$, $j \approx B/\delta = 1/\delta$, $\Delta t = \delta/v_n$, and $v_n = v_{An} \approx B_n/\sqrt{\rho_u} = B_n$, which yields

$$\delta = 2(\gamma - 1)\eta/B_n. \tag{3.17}$$

I have tested this hypothesis for the cases of $\eta = 0.002$ and 0.001, $\beta = 0.1$ and $B_n = 0.025$. Figure 3.5 shows the compression ratio ρ_d/ρ_u (top) and entropy ratio S_d/S_u (bottom) as a function of the grid separation Δx in the one-dimensional slow shock simulation by using the entropy equation. The solid lines indicate the theoretical results from the RH relations. A result from the energy equation by using resistivity $\eta = 0.002$ is labeled by stars. The circle and square markers are the results by using resistivity $\eta = 0.002$ and 0.001, respectively. Figure 3.5 shows that the results from the entropy equation converge to the theoretical results for increasing resolution as indicated by my estimate for the required width of the current layer. However, a much higher resolution (32 times higher) has to be used for the simulation employing the entropy equation. Therefore, the use of the energy equation appears much more appropriate for simulations involving shocks.
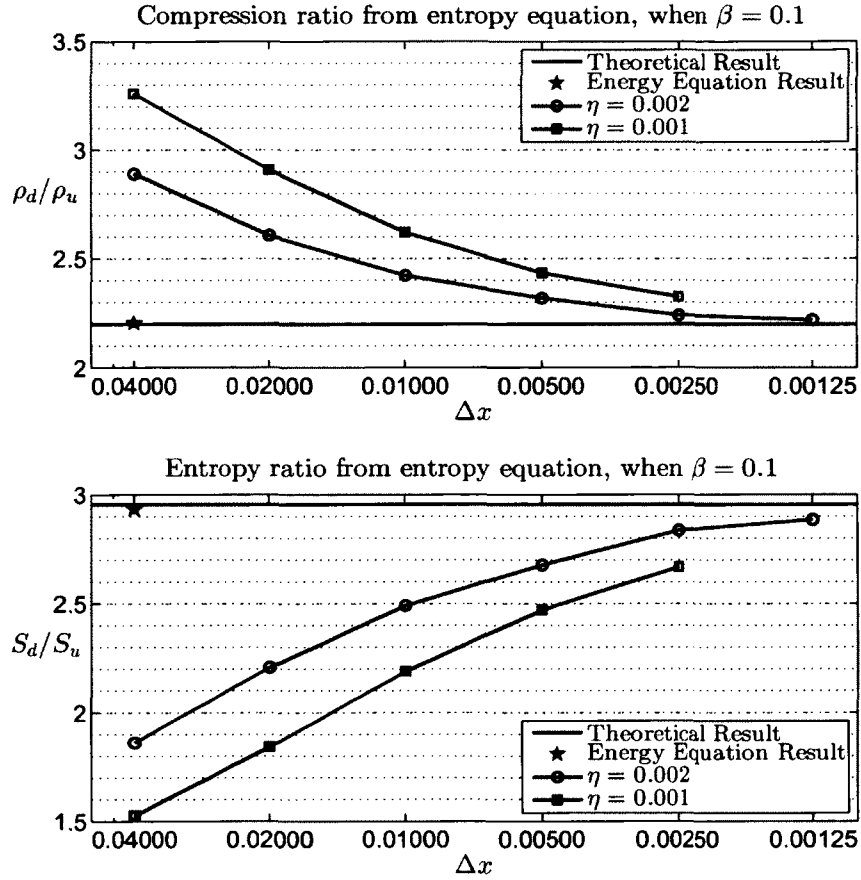
Figure 3.5: The compression ratio ρ_d/ρ_u (top) and entropy ratio S_d/S_u (bottom) as a function of the grid separation Δx from the one-dimensional slow shock simulation by using the entropy equation. The solid lines indicate the theoretical results from the RH relations. A result for the energy equation by using resistivity $\eta = 0.002$ is labeled by a star. The circle and square markers are the results by using resistivity $\eta = 0.002$ and 0.001, respectively.

3.3.1.2 Hall physics

Figure 3.6 presents the results from Hall MHD simulations by using energy equation with the resolution $\Delta x = 0.02$. The top four panels show the plasma density ρ, thermal pressure p, entropy S, and current density j from the case, in which the Hall parameter is $l = 0.6$ (ion inertia scale is 0.6 of the typical length) and the upstream plasma beta is 0.1. The dash-dotted lines are the theoretical results from the RH relations, and the downstream plasma conditions from Hall MHD are identical to the downstream MHD results. This is because that the presence of the Hall term does not change the RH relation. Thus, the jump conditions are as the same as for the MHD case. However, Hall physics leads to a much wider width of the transition layer for all quantities compared to MHD (see Figure 3.4) and the maximum current density is much smaller than in the equivalent MHD model (the current density is not listed in Figure 3.4), because the inclusion of the Hall term in the equations introduces a new typical length, the ion inertia scale into the physics. Since the large scale jump conditions are the same in MHD and Hall MHD, the solution requires a current in the z direction to turn off the magnetic field B_y component. However, the Hall term leads to the separation of the ion and electron velocity, and the frozen-in condition only applies to the electrons which carry some of this current. Thus, Hall physics implies a deflection of the magnetic field into the z direction. Apparently this deflection is the source of a standing whistler wave downstream of the maximum current density. For a better representation of this standing whistler wave, I normalized the current density j_y component to the total current density j, which is plotted in the fifth panel and the period of a wave (wavelength λ) is indicated by the double-arrow. The bottom panel of Figure 3.6 shows the wavelength for the standing whistler wave λ increase with the increasing Hall parameter l. Note, that the quadrupolar magnetic field typical for Hall reconnection [Ma and Bhattacharjee, 2001] corresponds exactly to the current and magnetic field perturbations of this one-dimensional Hall transition from the in-to the outflow region.
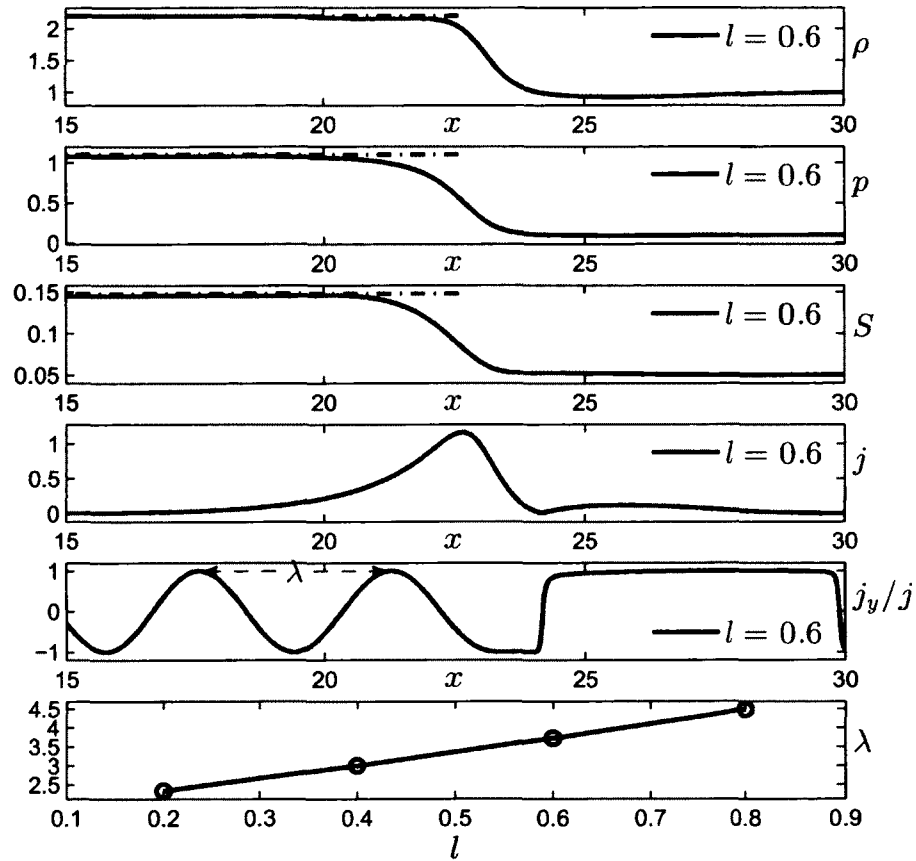
Figure 3.6: The top five panels show the plasma density ρ, thermal pressure p, entropy S, current density j, and the y component of the current density normalized to the total current density j_y/j in a Hall MHD slow shock-like simulation (the Hall parameter $l = 0.6$) with upstream plasma beta $\beta = 0.1$, and $\Delta x = 0.02$. The dash-dotted lines are the theoretical results from the RH relations. The bottom panel shows the wavelength (which is labeled in the fifth panel) as a function of the Hall parameter l.

3.3.1.3 Estimate of the entropy increase in the magnetic reconnection

It is demonstrated that slow switch-off shocks generate strong nonadiabatic heating for low upstream (inflow) plasma beta β using analytical theory and simulation, and that Hall physics does not change this result. However, this conclusion is based on one-dimensional shock configurations. To extend this argument to two-dimensional magnetic reconnection and more general inflow conditions including asymmetries requires a more general estimate.

In magnetic reconnection, pressure balance implies:

$$p_i + B_i^2 = p_o + B_o^2, \tag{3.18}$$

where i and o indicate the inflow and outflow region, respectively. Therefore, the entropy increase can be expressed as

$$\frac{S_o}{S_i} = \frac{p_o}{p_o^\gamma} \frac{\rho_i^\gamma}{p_i} = \left(\frac{p_i + B_i^2 - B_o^2}{p_i} \right) \left(\frac{\rho_i}{\rho_0} \right)^\gamma. \tag{3.19}$$

Since $B_o^2 \geq 0$, and $\rho_i < \rho_0$, due to compression, it follows that:

$$S_o/S_i < 1 + 1/\beta_i, \tag{3.20}$$

where β_i is the inflow plasma beta. The physical interpretation is straightforward. The pressure balance determines the thermal pressure in the outflow region and the thermal pressure ratio between out- and inflow regions is large if the pressure is very small in the inflow region. Thus, large entropy increases are possible only for very small plasma beta in the inflow region.

In case A, the entropy increase is consistent with the RH relation (Equation (3.14) gives $S_o/S_i = 2.95$). The estimate for entropy increase (3.20) gives a over estimate $S_o/S_i < 11$, since it does not take the compression into account. In the steady outflow region, the thermal pressure is almost identical with the total pressure (see the right-second panel in Figure 3.2), which is consistent with my assumption. Furthermore, I hypothesize that for the same inflow plasma beta β, this is the maximum possible

entropy increase, i.e., the presence of shear flow or magnetic guide field can not increase the entropy above this value.

3.3.2 Other Entropy Sources: the Diffusion Region and the Weak Fast Shock

The diffusion region is critical for the magnetic reconnection. In this region, the resistive term in Ohm's law is dominant, and nonadiabatic heating is prominent. Since the pressure is determined by total pressure balance with the inflow region, the density must decrease to balance the increasing plasma temperature. The low density plasma is convected along stream lines. Due to the symmetry, the central streamline is the y axis, which is consistent with the result in Figure 3.2. However, the typical width of the diffusion region is on the order of an ion inertia scale for Hall physics and even smaller (electron inertia or gyro scale) in a kinetic model, which is negligible compared with macro scales of the whole system. Thus I argue that the nonadiabatic heating in the diffusion region occupies a very small volume in a real space plasma and only a tiny fraction of the total plasma transported into the outflow region is actually going through the diffusion region. Therefore, only a small fraction of the plasma transported into the magnetosphere would be exposed to this nonadiabatic heating source.

The plasma in the steady outflow region is accelerated to the inflow region Alfvén speed by the slow switch-off shock. However, the plasma in the non-steady bulge region moves at a velocity significantly lower than Alfvén speed. Due to the compression and heating, the acoustic speed in the outflow region can be lower than the velocity of the outflow jet. Therefore, it is possible for the fast shock to exist in the transition from the steady outflow to the bulge [*Zenitani and Miyoshi*, 2011], (in Figure 3.2 $y \in (100, 110)$). To characterize these fast shock, I estimate the outflow region Mach number $M_o = V_o/c_{so}$, where V_o is outflow speed, which equates to the inflow Alfvén speed $V_{A_i} = B_i/\sqrt{\rho_i}$, and $c_{so} = \sqrt{\gamma p_o/(2\rho_o)}$ is the outflow acoustic speed. The pressure in the outflow region can be represented by the magnetic field

in the inflow region from pressure balance $p_o = p_i + B_i^2$. By using the jump condition for density in a switch-off shock (3.12), I find

$$M_o = \sqrt{2/(\gamma\beta_i + \gamma - 1)} \leq \sqrt{3}. \tag{3.21}$$

This Mach number does not take into account the shock speed. Therefore, the actual Mach number is smaller. And a weak fast shock is not expected to be a significant source for the entropy increase. I note that in *Zenitani and Miyoshi*'s [2011] high resolution simulation the maximum velocity of outflow jet in this fast shock region is higher than the inflow region Alfvén speed. However, the entropy remains constant across this fast shock.

3.4 More General Configurations

Although I have mostly discussed Petschek reconnection, the conclusions drawn from the estimate for the entropy increase Equation (3.20) apply to more general and asymmetric configurations. In this section, I will discuss three different reconnection configurations which more closely reflect to the real magnetopause geometry.

3.4.1 Asymmetric Density

An asymmetric configuration, with different densities and an inflow plasma beta β of 0.025, is examined in case B. The normalized entropy S/S_0 at $t = 100$ is presented in the left panel of Figure 3.7, where S_0 is the initial magnetosheath side entropy $(x > 0)$, which is $2^\gamma \approx 3.17$ times lower than magnetospheric entropy, due to the different densities. However, on both sides of the outflow region, entropy increases about 4 times compared to its original value. The magnetic field lines (the black contours in the left panel of Figure 3.7) indicates that the slow shock on the magnetosheath side is replaced by an intermediate shock [*Yong and Lee*, 1990]. For a better illustration of the outflow, the right side of Figure 3.7 shows profiles of the thermal pressure p, normalized entropy S/S_0, magnetic field B_y component, current density j_z component, and velocity V_y component, which are taken from the magenta line in

the left panel. The current density is higher on the magnetosheath side than on the magnetospheric side, which is consistent with the larger rotation of magnetic field on the magnetosheath side. This is caused by the larger inertia of the higher density magnetosheath material which requires a larger $\mathbf{j} \times \mathbf{B}$ force to change the momentum and accelerate the plasma into the outflow region[*La Belle-Hamer et al.*, 1995]. This also generates a non-zero outflow magnetic field $B_o = B_y \neq 0$, which contributes to the total pressure in the outflow region. The outflow total pressure $p + B^2$ (labeled by the dashed line in the right-uppermost panel of Figure 3.7) is larger than the thermal pressure p. The red dashed line in the entropy panel indicates the results from the RH relations, which implies that the entropy increase in the asymmetric case is less than the corresponding symmetric case.

The rigorous manner to determine B_y in the outflow region is to solve the Riemann problem [*Lin and Lee*, 1993, 1999]. However, a reasonable estimate of B_y in the outflow region can be obtained by assuming an approximately constant outflow velocity [*La Belle-Hamer et al.*, 1995], which is consistent with the right-lowermost panel in Figure 3.7. From the momentum equation and ignoring the pressure gradient along the y direction, I have

$$\rho \frac{dv_y}{dt} = j_z B_x. \tag{3.22}$$

By integrating both sides from the inflow region to outflow region

$$v_y = \int_{\text{inflow}}^{\text{outflow}} \frac{j_z B_x}{\rho} dt, \tag{3.23}$$

where $dt = dx/v_x$, and $v_x = V_{Ax} = B_x/\sqrt{\rho}$, which yields to

$$v_y = \int_{\text{inflow}}^{\text{outflow}} \frac{j_z}{\sqrt{\rho}} dx = \frac{B_i - B_o}{\sqrt{\rho}}. \tag{3.24}$$

Here I ignore compressibility. This assumption is not bad, since the maximum compression is 2.5, and the expression inside of the integral is inverse to the square root of the density. I apply this equation to both sides of the boundary, which yields to

Figure 3.7: The left panel shows the normalized entropy S/S_0 at $t = 100$. Black lines are the magnetic field lines. The five panels on the right side show the profiles of the thermal pressure p, normalized entropy S/S_0, magnetic field B_y component, current density j_z component, and velocity V_y component, which are taken from the magenta line in the left panel. The total pressure $p + B^2$ is presented by dashed line. The estimated value of B_o from Equation (3.25) is indicated by a red dashed line.

$$\frac{B_i - B_o}{\sqrt{\rho_1}} = \frac{B_o + B_i}{\sqrt{\rho_2}}$$

$$B_o = \frac{1 - r}{1 + r} B_i, \tag{3.25}$$

where ρ_1 and ρ_2 refers to the density on each side, and $r = \sqrt{\rho_1/\rho_2}$. Equation (3.25) shows that the magnitude of B_0 is always smaller than B_i, and B_o vanishes, if the density is symmetric ($\rho_1 = \rho_2$). Interchanging ρ_1 and ρ_2 changes the sign of B_o. These properties indicate the soundness of the result. In the simulation $r = \sqrt{2}$, and B_o is indicated by red dashed line in the right-third panel of Figure 3.7, which shows a good agreement with the simulation result. Combining Equation (3.25) and (3.19), I obtain

$$\frac{S_o}{S_i} < 1 + \frac{1}{\beta} \frac{4r}{(1 + r)^2}, \tag{3.26}$$

where S_i can be the entropy on either side. This relation (3.26) implies a reduction of the entropy increase in the presence of density asymmetry for the same inflow plasma beta.

3.4.2 Magnetic Shear

Magnetic reconnection without guide field is a singular situation in space plasma system. A guide field component is present almost everywhere at the dayside magnetopause. In a two-dimensional configuration, the guide field component (B_z component in this study) does not change the reconnection dynamics significantly, because it can be considered as an additional pressure and is convected by the plasma. This B_z component often increases in the outflow region, which may cause the reduction of the entropy increase in the outflow region. Figure 3.8 shows the results from Case C, where the initial configuration is the same as in Case A, except for the addition of a uniform guide field $B_z = 1$. The left panel is the normalized entropy S/S_0 at

$t = 150$, where S_0 is the inflow entropy. It shows that the outflow entropy is about 1.5 times higher than the inflow entropy, which is lower than in Case A. To better understand this transition region, a rigorous treatment is to solve the Riemann problem [*Lin and Lee*, 1993, 1999]. *Lin and Lee* [1993] demonstrated that, the switch-off shock is replaced by a rotational discontinuity and a slow shock for a symmetric guide field, which is also seen in my two-dimensional simulation. The five panels on the right side of Figure 3.8 show the profiles of the normalized entropy S/S_0, plasma beta β, two components of the tangential magnetic field B_{t1} and B_{t2}, and the total tangential magnetic field $B_t = \sqrt{B_y^2 + B_z^2}$, which are taken from the magenta line in the left panel. Due to the symmetry, I only show the $x \geq 0$ part of the cut. For a better representation of the rotational discontinuity, I rotate the frame by an angle $\theta = \arctan\left(1/B_g\right)/2 = \pi/8$, thus

$$B_{t1} = B_z \cos\theta + B_y \sin\theta \tag{3.27}$$

$$B_{t2} = -B_z \sin\theta + B_y \cos\theta, \tag{3.28}$$

The rotational discontinuity layer is shaded in dark gray and labeled R, where B_{t1} is almost constant and B_{t2} changes from $+0.5$ to -0.5. Theoretically, the rotational discontinuity does not involve an entropy increase. However, the presence of the resistivity replaces the rotational discontinuity by an intermediate shock, thus leading to an increase in entropy and decrease in the total magnetic field, which is consistent with the results in Figure 3.8. The slow shock layer is shaded in light gray and labeled S, where the total tangential magnetic field strongly deceases. This remnant magnetic field, however, is still larger than the y component of the magnetic field B_y in the inflow region. The larger B_y field implies a smaller increase of the thermal pressure in the outflow region and for this reason a reduction in the entropy increase. Therefore, Case C demonstrates that the presence of a guide field reduces the entropy increase.
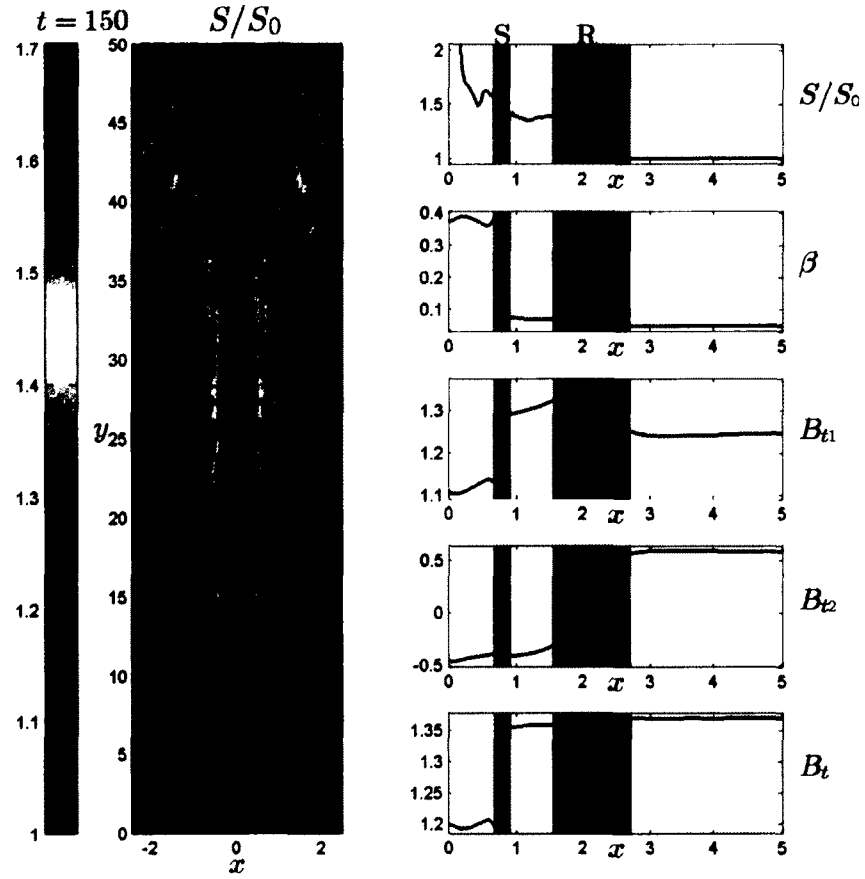
Figure 3.8: The left panel shows the normalized entropy S/S_0 at $t = 150$. Black lines are the magnetic field lines. The five panels on the right side show the profiles of the normalized entropy S/S_0, plasma beta β, two components of the tangential magnetic field B_{t1} and B_{t2}, and the total tangential magnetic field B_t, which are taken from the magenta line in the left panel.

3.4.3 Magnetic Reconnection with Shear Flow

Large shear flow always exists close to the magnetopause, due to the solar wind velocity. This sheared flow general has components along the y and z directions and here I consider shear along the z (invariant in the two-dimensional configuration) direction. Flow shear along the y direction has an effect similar to density asymmetry in that it generates a configuration similar to density asymmetry with a nonzero B_y in the outflow region [La Belle-Hamer et al., 1995]. For flow shear along the z direction, the frozen-in condition implies a drag of reconnected magnetic field lines into opposite directions on the two sides of the outflow region, which generates a B_z component. This B_z component contributes an additional magnetic pressure to the total pressure in the steady outflow region. This mechanism is demonstrated in Case D, where the initial configuration is the same as in Case A, except for the perpendicular flow shear. In Case D, the total perpendicular velocity jump is equal to the Alfvén speed. The left panel of Figure 3.9 shows the normalized entropy S/S_0 at $t = 110$, where S_0 is the inflow entropy. The figure shows that the outflow entropy is about twice the inflow entropy, which is lower than in Case A. Similar to the guide field case, the presence of the shear flow replaces the switch-off shock by an intermediate shock and a slow shock [Sun et al., 2005]. The five panels on the right side of Figure 3.9 show the profiles of the normalized entropy S/S_0, plasma beta β, two components of the tangential magnetic field B_{t1} and B_{t2}, and the total tangential magnetic field B_t, which are taken from the magenta line in the left panel. Due to the symmetry, I only show the $x \geq 0$ part of the cut. For a better representation of the intermediate shock, I rotated the frame by an angle $\theta = \pi/4$. The entropy increases through the intermediate shock layer and the slow shock layer. Again the pressure by the non-zero tangential magnetic field in the outflow region reduces the thermal pressure and the entropy increase.

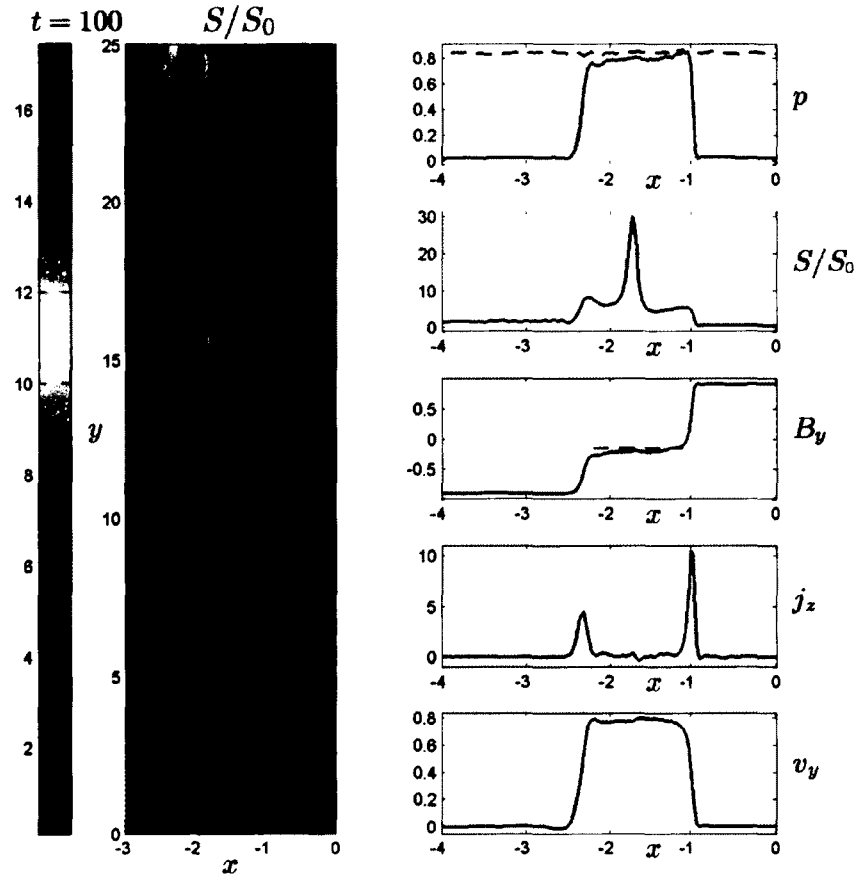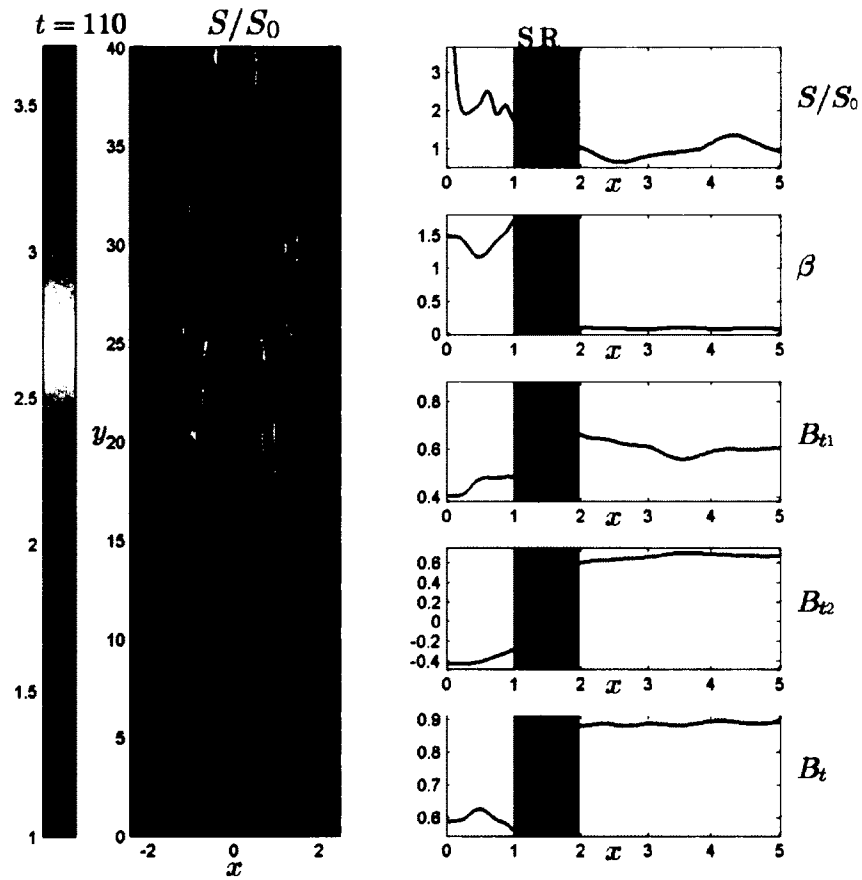Figure 3.9: The left panel shows the normalized entropy S/S_0 at $t = 110$. Black lines are the magnetic field lines. The five panels on the right side show the profiles of the normalized entropy S/S_0, plasma beta β, two components of the tangential magnetic field B_{t1} and B_{t2}, and the total tangential magnetic field B_t, which are taken from the magenta line in the left panel.

3.5 Summary and Discussion

The plasma entropy measure $p\rho^{-\gamma}$ is a useful physical quantity to identify adiabatic and nonadiabatic processes in a physical system, and satellite observations demonstrate that the access of solar wind plasma to the Earth's magnetosphere involves strong nonadiabatic heating. Magnetic reconnection is often suggested as the dominant process for this transport of plasma into the magnetosphere. In this study, I focus mainly on Petschek type magnetic reconnection, and I demonstrate that entropy can strongly increase only when the plasma $\beta \ll 1$ by means of theoretical analysis and numerical simulation using one-dimensional and two-dimensional configurations. Key arguments for this β limitation are (1) that the compression rate is usually around unity $(\rho_d/\rho_u = \mathcal{O}(1))$, and (2) that the thermal pressure is limited by the total pressure in an approximately pressure balanced system. A large entropy increase in such a total pressure balanced system requires a very small thermal pressure (compared to magnetic pressure) in the inflow region.

The prior discussion is mostly based on applications of steady state reconnection although reconnection is often considered to be a time dependent process (such as the formation of magnetic flux transfer events or plasmoids in the terrestrial magnetosphere). On sufficiently large spatial or temporal scales a steady state assumption is always violated such that I have to examine the conditions underlying the steady state assumption more carefully. The typical system time for dynamical changes in the reconnection geometry is $\tau_L = d/V$, where d is the width of the outflow region and V is the speed of group velocity of typical wave i.e, Alfvén speed for MHD physics, or whistler wave speed for Hall physics. In comparison, the typical time scale τ_r for the evolution of magnetic reconnection is characterized by the change of the reconnection rate r:

$$\tau = r\,(dr/dt)^{-1}. \tag{3.29}$$

Therefore, as long as $\tau_L \ll \tau_r$, a steady state assumption for magnetic reconnection is still applicable.

Hall physics can lead a fast reconnection rate. However, it does not change the

downstream and upstream shock relation. The frozen-in condition only applies to the electrons, which carry the majority of the current in thin current sheets and discontinuities. This current in the shocks that bound the outflow region leads to a strong deflection of the magnetic field. As a result, Hall physics introduces standing whistler waves at this boundary and changes the shock layer structure without changing the RH jump conditions that determine the change in entropy.

In two-dimensional magnetic reconnection, the entropy increase occurs mostly through the shock layers. The small reconnection diffusion region can heat plasma locally. However, it has no volume filling effect because of its microscopic (ion or electron inertia scale) size. A fast shock may exist in the transition region between steady outflow region and non-steady bulge region, when inflow plasma beta is low. However, the Mach number is too small (marginally above 1), such that the fast shock is not expected to be a major entropy source.

For more realistic configuration, density asymmetry leads to $B_y \neq 0$ in the outflow region which reduces the entropy increase. The presence of a guide field and a perpendicular shear flow also reduce the entropy increase in the outflow region. This reduction of nonadiabatic heating is caused the replacement of the switch-off shock in the steady-outflow region by a rotational discontinuity (or intermediate shock) and a slow shock, which does not switch off the tangential component of the magnetic field for both configurations. Therefore, any asymmetry, guide field, or shear flow increases the magnetic field magnitude in the outflow region and reduces the thermal pressure increase from the in- to the outflow regions which results in a lower entropy increase than in the symmetric (Petschek) situation.

The presented results demonstrate that magnetic reconnection can indeed generate a strong nonadiabatic heating. However, the condition for this is a sufficiently small plasma $\beta \ll 1$. Typical magnetosheath conditions imply a plasma beta of order 0.1 to 1. This is insufficient to explain the observed entropy of at least $1 \sim 2$ orders of magnitude between the magnetosheath and the magnetosphere. It is also noted that reconnection causes plasma compression where the original magnetosheath den-

sities are already too high in comparison with plasma sheet. A subsequent adiabatic expansion would lower the temperature of the plasm far below values observed in the magnetosphere. Therefore it is concluded that additional physics is required to explain density and temperature of the plasma sheet. Such physics can include:

1. plasma conditions that are not typical magnetosheath. For instance, density and plasma beta are typically significantly lower in the plasma depletion layer just outside of the magnetopause.

2. plasma conditions that are modified by additional processes such of Kelvin-Helmholtz instability.

3. other processes that contribute to the plasma entry, such as diffusion or other microphysical processes.

There are two particularly important applications for low beta reconnection. In the magnetotail lobes (similar in other magnetospheres such as the giant planets) the plasma beta is extraordinarily low. Here reconnection of lobe magnetic field can be expected to increase the entropy very significantly by orders of magnitude. The second application is reconnection in the solar corona where again the plasma beta is very low, and magnetic reconnection can increase the plasma entropy by orders of magnitude.

Chapter 4
Mechanisms of Field-Aligned Current Formation in Magnetic Reconnection

4.1 Introduction

Magnetic reconnection changes the magnetic topology and releases the stored energy, which is believed to play an important role at the Earth's magnetopause and magnetotail [*Dungey*, 1961; *Birn and Priest*, 2007]. At the magnetopause, magnetic flux transfer events (FTEs) [*Russell and Elphic*, 1978] often occur at the low latitude boundary layer (LLBL) for southward interplanetary magnetic field (IMF) conditions, which is considered as evidence of magnetopause magnetic reconnection. Field-aligned currents (FACs) are often observed associated with FTEs [*Saunders et al.*, 1984; *Marchaudon et al.*, 2004, 2009]. It has been demonstrated that FACs are carried by Alfvén waves along FTE flux tubes and propagate away from the magnetopause into the ionosphere [*Saunders et al.*, 1984]. Several authors [*Lee*, 1986; *Southwood*, 1987; *Cowley and Lockwood*, 1992] discussed electrodynamic models of FACs distributions associated with FTEs. In the magnetotail, magnetic reconnection is believed to play an important role in magnetic substorms. FACs are generated in the magnetotail and are highly enhanced after the onset of substorms [*Ma et al.*, 1995; *Birn and Hesse*, 1996]. Similarly earthward moving bubbles have been found to be associated with FAC systems [*Birn et al.*, 2004].

It is believed that many of the FACs which are generated in the outer magnetosphere connect to the auroral ionosphere and contribute to the typical Region 1 (poleward) and Region 2 (equatorward) system of FACs that connect ionosphere and outer magnetosphere. In regions with upward FACs, electrons may be accelerated to high energies, leading to auroral brightening on the dayside as well as nightside ionosphere [*Ma and Lee*, 1999]. Therefore, the mechanism of FAC formation is of large importance for the coupling of the magnetosphere and it's processes to the ionosphere.

It has long been known that localized pressure or inertial gradient terms perpendicular to the magnetic field imply a field-aligned gradient of FAC [*Vasyliunas*, 1984].

While sometimes addressed as source regions, for FAC such gradients do not provide causal explanation for theses currents. *Ma et al.* [1995], and *Ma and Lee* [1999] demonstrated that three-dimensional magnetic reconnection can in fact generate localized pressure gradients and inertia terms and therefore establish a system of FACs in the reconnection bulge region. *Yamade et al.* [2000] suggested that the Hall current generated in the course of magnetotail reconnection may contribute significantly to the global FAC pattern. Later, *Ma and Lee* [2001] showed that the magnitude and distribution of FACs are significantly modified by the Hall term. These previous studies are mostly based on three-dimensional configurations. However, magnetic or velocity shear should be very efficient to generate FAC in two dimensions. In fact, several of the three-dimensional results can probably be attributed to two-dimensional mechanisms.

In the traditional two-dimensional magnetic reconnection models by Sweet-Park [*Parker*, 1957; *Sweet*, 1958] and by *Petschek* [1964], there are no FACs. However, at the dayside magnetopause, magnetic reconnection operates always with a guide field component, which generally is along the current direction. Therefore, in this configuration, it is natural to have FAC. However, whether this is a simple projection effect or if there is an additional generation of FAC during the process is unresolved. Associated with this question is the dependence of FAC varying on the magnitude of the guide field component.

Magnetic reconnection is suggested as the dominant process for plasma transport from solar wind into the Earth's magnetosphere for southward IMF conditions. However, a large velocity shear always exists close to the magnetopause, because the shocked solar wind streams around the magnetosphere. In general this sheared flow has components along the z directions (invariant in two-dimensional configuration) direction. Different tangential velocities on two sides of a boundary are possible without a change of the boundary structure only for a tangential discontinuity. If a magnetic field connects the two sides of the boundary, the frozen-in condition implies a drag of the reconnected magnetic field line into opposite directions on both sides of

the boundary, which generates a B_z component and thereby FAC. This particularly also applies to magnetic reconnection in the presence of shear flow across a plasma boundary. The relation between the magnitude of the shear flow and the generated FACs is highly important and is examined in this study.

For magnetic reconnection, the typical length scale of the diffusion region is on the ion or even on the electron inertia scale. Therefore, it is also important to examine the influence of Hall physics on FAC formation. The inclusion of the Hall term in the equations leads to the separation of the ion and electron velocity, and the frozen-in condition only applies to the electrons, which move anti-parallel to the current in a thin current sheet. Therefore, the effect of Hall physics is not unlike the effect of shear flow in ordinary MHD. In magnetic reconnection, Hall physics generates the typical bipolar structure of the magnetic field B_z component and Hall current system [*Otto*, 2001; *Ma and Bhattacharjee*, 2001]. *Ma and Lee* [2001] examined the influence of Hall physics on FAC generation by using three-dimensional simulation. However, much of this FAC generation might be attributed to two-dimensional mechanisms. It is also a goal of this study to examine FAC generation by Hall physics in two dimensions.

The above questions are systematically examined in this study by using two- and one-dimensional MHD and Hall MHD simulation considering the influence of a guide magnetic field and of shear flow.

4.2 Numerical Model

In this study, I solve the full set of the one- and two-dimensional normalized resistive MHD and Hall MHD equations as introduced in Chapter 2. The results from three selected simulation cases to study the FAC formation mechanism are present in Section 4.3. The simulation domain is a box with $|x| \leq 30$, and $0 \leq y \leq 120$, and is resolved by using 203×403 grid points with a non-uniform grid along the x and y directions, where the x direction normal to the current layer (boundary), y is direction along the boundary, and z is along the invariant direction. To sufficiently resolve the diffusion region, the best resolution is set to 0.1 and 0.2 in the x and y

Table 4.1: Values of the simulation parameters

Case	B_{z0}	V_{z0}	l
A	0.5	0	0
B	0	0.5	0
C	0	0	1

direction in the diffusion region. The initial equilibrium is a one-dimensional modified Harries sheet given by

$$B_x = 0, \tag{4.1}$$

$$B_y = \tanh(x), \tag{4.2}$$

$$B_z = B_{z0}, \tag{4.3}$$

$$V_x = 0, \tag{4.4}$$

$$V_y = 0, \tag{4.5}$$

$$V_z = V_{z0} \tanh(x), \tag{4.6}$$

$$p = p_\infty + 1 - B^2, \tag{4.7}$$

$$\rho = 1, \tag{4.8}$$

where $p_\infty = 0.25$, and the values of other parameters are list in Table 4.1. Case A is chosen to study the FAC formation for magnetic reconnection with a guide field. Case B is included to investigate case in which shear flow is perpendicular to magnetic reconnection, and Case C is used to examine the influence of Hall physics on FAC formation.

In this study, magnetic reconnection is triggered by the localized resistivity model

$$\eta = \eta_0 \exp\left(-t/t_0\right) / \left[\cosh(x)\cosh(y)\right] + \eta_b, \tag{4.9}$$

where $\eta_0 = 0.05$, $t_0 = 3$, and $\eta_b = 0.002$ is the background resistivity to smooth the numerical dispersion. Free boundary conditions ($\partial_n = 0$, where ∂_n is the partial derivative in the direction normal to the boundary) are applied to the x maximum

and minimum boundary and y maximum boundary. The y minimum boundary is determined by symmetry properties of the (Hall) MHD equations [*Otto et al.*, 2007].

The transition of the plasma properties (density, velocity, pressure, and magnetic field) from one inflow region through the outflow region to the other inflow region is mostly one-dimensional and is achieved in general through a series of MHD waves and discontinuities. To better resolve the physics in this transition layer, I carry out one-dimensional simulations of the Riemann problem, which has the advantage to choose much higher resolution for shorter execution times and better accuracy (uniform grid with $\Delta x = 0.02$ in this study). This transition layer can be simulated in a one-dimensional configuration by adding a small constant B_n ($= 0.025$ in this study) component to the Harries sheet magnetic field [*Lin and Lee*, 1993, 1999]. In order to compare with the two-dimensional results, I use the same parameters as for the two-dimensional cases. The resistivity η is 0.0002 for most cases, and for some Hall MHD cases large resistivity $\eta = 0.002$ is applied for the numerical stability reason.

4.3 Simulation Results

In a two dimensional configuration, the guide field component (B_z component in this study) does not change the dynamics of magnetic reconnection significantly, because it can be considered as an additional pressure and is convected by the plasma. Figure 4.1 illustrates results from case A (with a guide magnetic field of 0.5) and the corresponding one-dimensional simulation. The left panel shows FAC density $j_\parallel$ at $t = 150$ for case A. Black lines are reconnected magnetic field lines (contours of the z component of vector potential A_z). The middle five panels show the profiles of B_y, B_z, j_y, j_z, and $j_\parallel$ in a cut at $y = 59.81$, indicated by the purple line in the left panel. The corresponding one-dimensional simulation results are presented in the right panels. Note, that the FAC density is present only on reconnected field lines and localized where the magnetic field is strongly bend, which indicates that the formation of the FAC is in part a projection effect in the presence of B_z. However, the

guide field alters the transition layer structure. The switch-off shock is replaced by an intermediate shock (a rotational discontinuity-like structure in resistive MHD) and a slow shock [*Lin and Lee*, 1993, 1999], which is illustrated by the five middle panels. From the inflow region (right), B_y turns to 0 while B_z increases to 1, which requires a current layer (j_y and j_z) to rotate the magnetic field and therefore generate the FAC. Behind this intermediate shock, the decreasing B_z in the slow shock corresponds to a decreasing j_y and $j_\parallel$. Close to the diffusion region (around $y = 0$) these structures have not fully developed such that, the intermediate shock and slow shock may overlap or interact with each other. To better represent this transition layer structure, I also conducted a one-dimensional simulation with the same upstream (inflow) parameter. The five panels on the right side show a similar structure and value compared to the middle five panels. Note, that in both cases, the intermediate shock layer is wider than the slow shock layer. This difference is not caused by the grid resolution, because the one-dimensional simulation is using a higher resolution uniform grid. A possible physical interpretation is that a wider current layer causes a lower entropy increase in the intermediate shock, which is better consistent with a constant entropy profile through the rotational discontinuity as would be the case in the ideal MHD. In contrast, a thin current layer is required to generate strong nonadiabatic Ohmic heating through the slow shock layer. Strictly, slow shocks cannot generate FACs due to the coplanarity condition. The respective FAC in the simulation is likely because the structure is not a pure slow shock or because of numerical artifacts. In conclusion, magnetic reconnection with a guide field component generates FAC along the open field lines by intermediate shocks, and slow shock layers are not a source for FAC.

Note, that the intermediate shock is not a static structure. Figure 4.2 shows the temporal evolution of the magnitude of FAC density $j_\parallel$ in the intermediate shock for $B_{z0} = 1$ from the one-dimensional simulation. It illustrates that the intermediate shock is not well developed at the early times $t < 200$. After $t < 200$, $j_\parallel$ decreases with time due to resistive diffusion. In order to quantify the FAC density $j_\parallel$ as a function of the guide field magnitude B_{z0}, I compare the maximum value of $j_\parallel$ in the
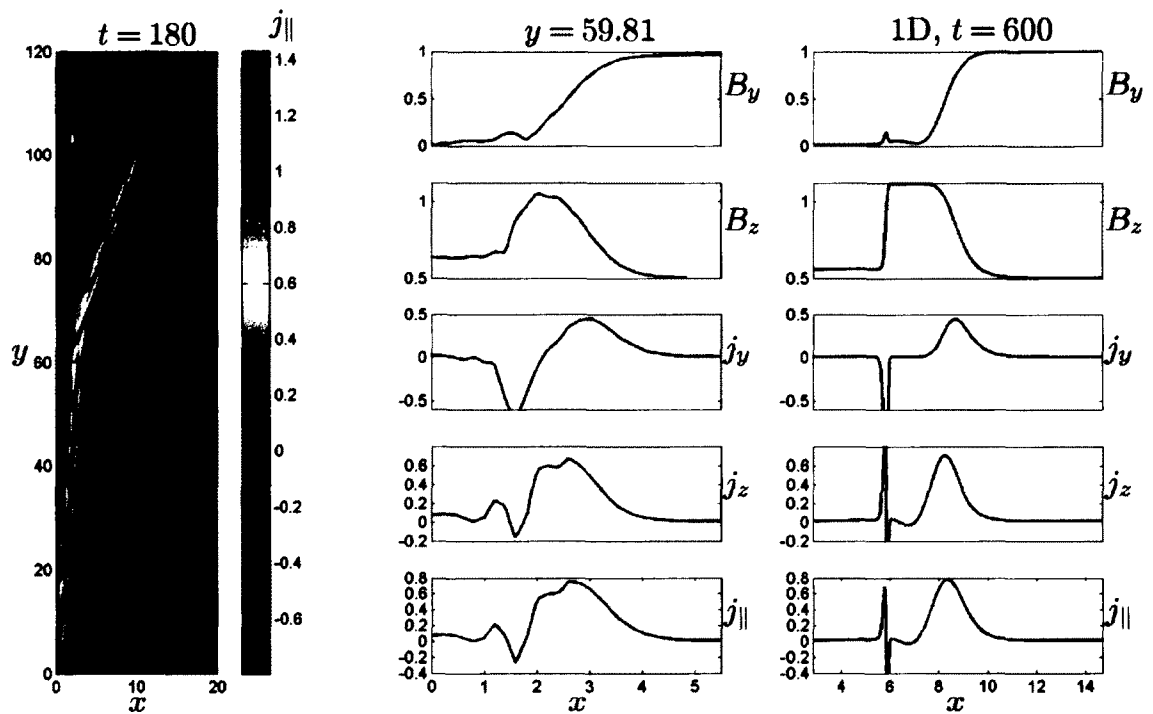
Figure 4.1: The left panel shows FAC density $j_{\|}$ at $t = 150$ for case A. Black lines are open magnetic field lines (contours for vector potential). The middle five panels show the profiles of B_y, B_z, j_y, j_z, and $j_{\|}$ in a cut at $y = 59.81$, which is indicated by a purple line in left panel. The corresponding one-dimensional simulation results are presented in the right five panels.

intermediate shock after the intermediate shock is well developed.

The left panel of Figure 4.3 shows the maximum $j_\parallel$ in the intermediate shock for different guide magnetic field B_{z0} varying from 0.1 to 1. It illustrates that $j_\parallel$ is not large for a small guide field component, which agrees with the asymptotic state without a guide field for which $j_\parallel = 0$. However, for a large guide field, the total magnetic field rotation through the intermediate shock is small. Therefore, it is also not expected to have a large $j_\parallel$.

To evaluate the overall FAC generated by the guide field component, I integrate the FAC density $j_\parallel$ along the x axis. Since the initial configuration already has a FAC, the integral $\int j_\parallel dx$ also indicates whether the FAC is generated or simply redistributed. The middle panel of Figure 4.3 shows $\int j_\parallel dx$ varying with the time for different guide field magnitudes B_{z0}. The same color as in the left panel of Figure 4.3 is used to identify different B_{z0} values. It shows that initially $\int j_\parallel dx$ is proportional to the guide field magnitude B_{z0} and converges to values between 1.1 and 1.2. For a small guide field component, $\int j_\parallel dx$ strongly increases with time, which indicates that strong FAC has been generated in magnetic reconnection. For larger guide field values B_{z0}, the increasing $\int j_\parallel dx$ diminishes, which implies that for large guide fields FACs are mostly redistributed. Note, that the final value of $\int j_\parallel dx$ varies only between 1.1 and 1.2, which is a small range compared to the variation of the initial values. This indicates that the overall evolving FAC is not very sensitive to the magnetic guide field value.

For a mapping into the ionosphere, it is the total FAC, instead of the maximum FAC density that is important. Due to the frozen-in condition, $\Phi = Bs$ is a constant value along the magnetic field, where Φ is the magnetic flux, and s is the cross sectional area of a magnetic field flux tube. Thus, $j_\parallel B^{-1}$ can be used to estimate FAC, because B^{-1} is proportional to the cross sectional area (this assumes that all FAC closes in the ionosphere and stays on the same magnetic flux tube). The total FAC into the ionosphere is determined by the integral $j_\parallel B^{-1}$ along x. This quantity should be conserved, if the current is mostly along the magnetic field direction. The
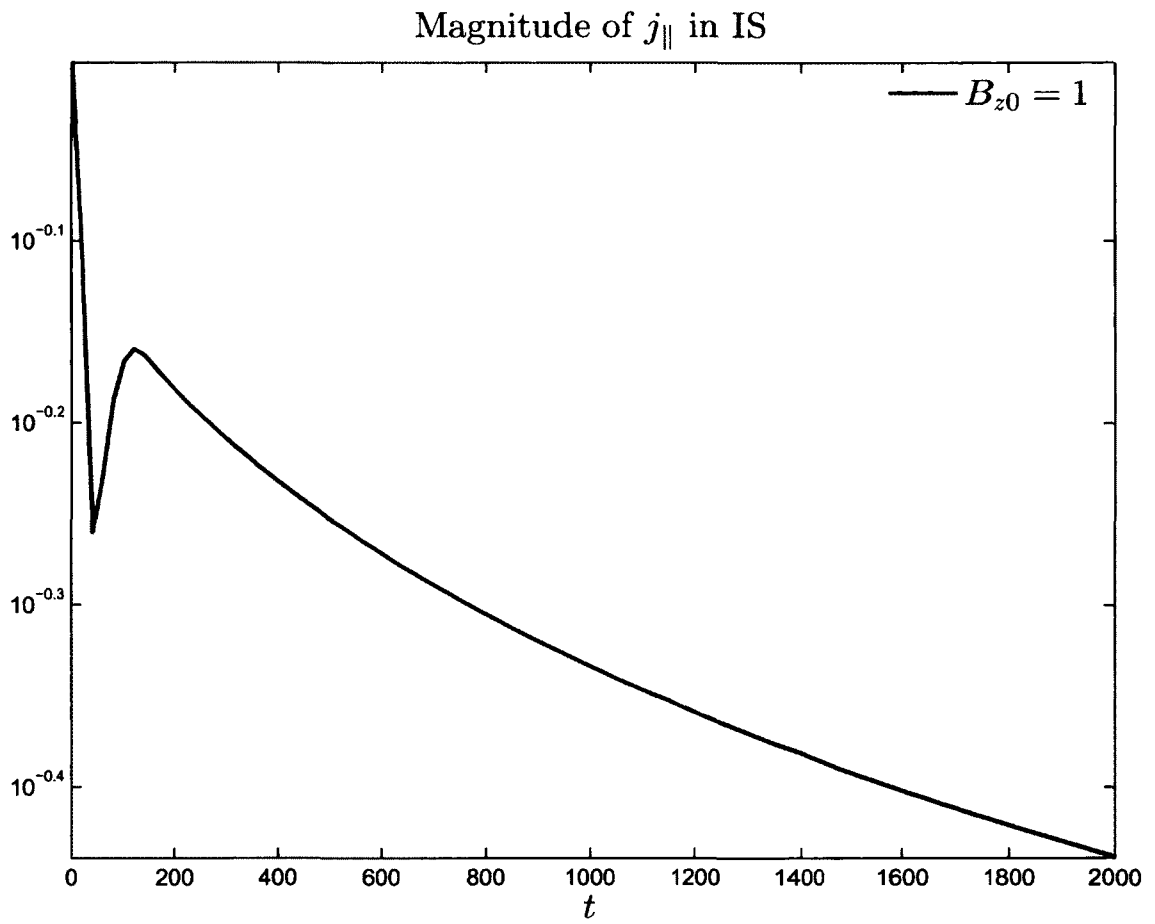
Figure 4.2: The magnitude of FAC density $j_\parallel$ in the intermediate shock as a function of time.
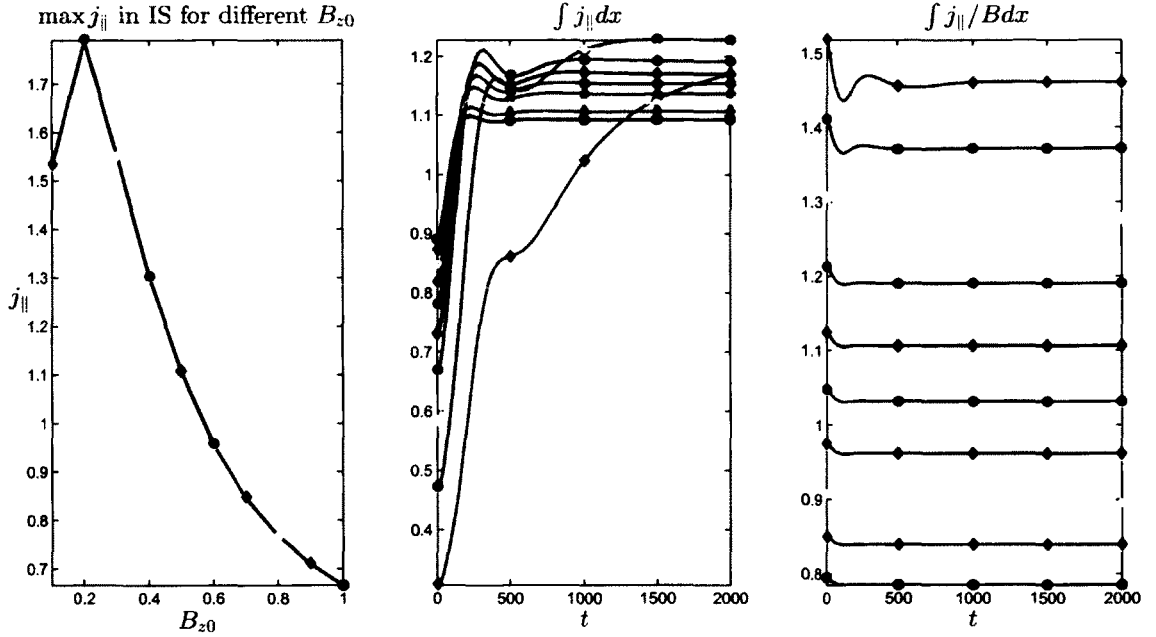
Figure 4.3: The maximum FAC density $j_\parallel$ (left), $\int j_\parallel dx$ (middle), and $\int \left(j_\parallel / B\right) dx$ (right) for different guide field magnitude B_{z0}.

right panel of Figure 4.3 shows $\int j_\parallel B^{-1} dx$, which confirms this assumption. The value of $\int j_\parallel B^{-1} dx$ decreases with increasing B_z which seems inconsistent with the limit of $B_z = 0$ where $\int j_\parallel B^{-1} dx = 0$. This limit is indeed not analytic and the FAC changes discontinuous from -1 to $+1$ (in normalized units) for arbitrarily small negative or positive B_z. Note, that $\int j_\parallel dx$ is analytic because although the $j_\parallel$ represents a step function, the integral current converges to 0 because the current is nonzero only in an arbitrarily small vicinity of $x = 0$. It is noted that that the limit of B_z to 0 is not realistic in MHD because an extreme concentration of the FAC will involve kinetic processes.

Figure 4.4 illustrates results for case B (with 0 guide field but finite shear velocity) using two and one-dimensional simulations. The left panel shows FAC density $j_\parallel$ at $t = 180$ for case B. Black lines are reconnected magnetic field lines (contours of the z component of vector potential A_z). The middle five panels show the profiles of B_y, B_z,
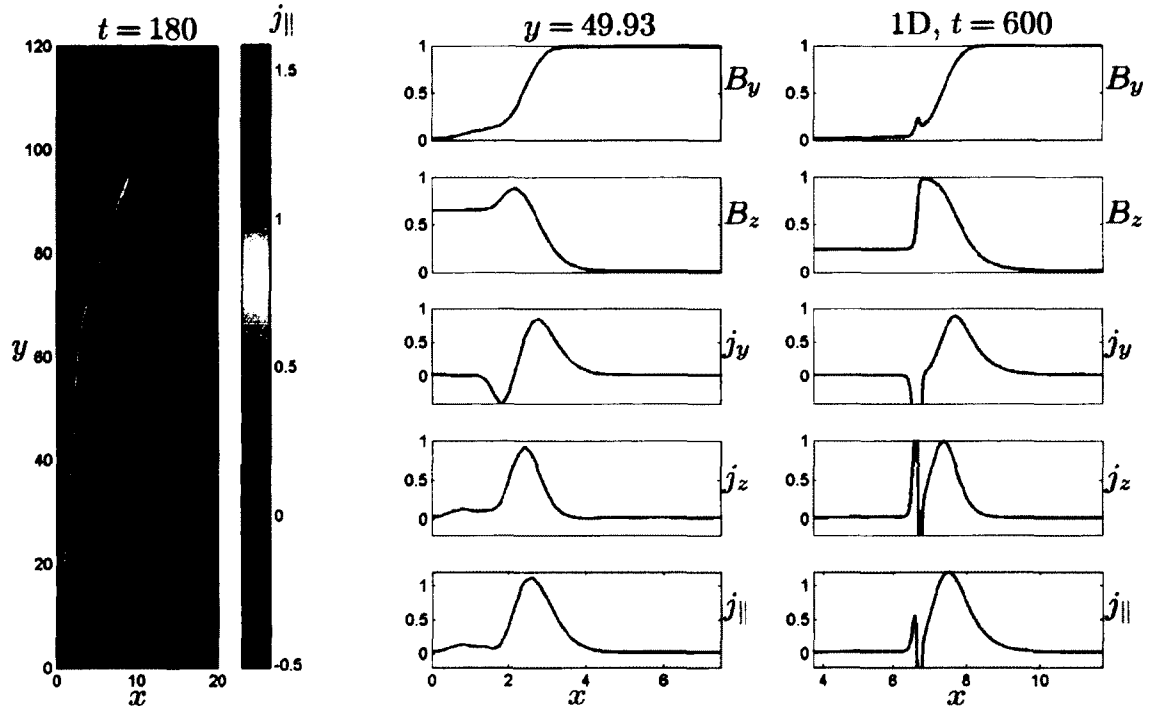
Figure 4.4: This figure has the same format as Figure 4.1. The middle five panels show the profiles of B_y, B_z, j_y, j_z, and $j_\parallel$ in a cut at $y = 49.93$, indicated by a purple line in left panel. The corresponding one-dimensional simulation results are presented in the right five panels.

j_y, j_z, and $j_\parallel$ in a cut at $y = 59.81$, indicated by the purple line in the left panel. The corresponding one-dimensional simulation results are presented in the right panels. All FACs are again located on the open field lines. The middle five panels show that the magnetic field B_y component is switched off while the B_z component is switched on, which indicates again that this is an intermediate shock and the magnetic field rotates from y direction to the z direction. The strong negative excursion of j_y represents a slow shock. The high resolution one-dimensional simulation shows that the slow shock represents a much thinner layer. In general, the structure of the magnetic reconnection layers is somewhat similar to the case A [Sun et al., 2005].

Figure 4.5 has the same format as Figure 4.3, except that the different curves represent different shear flow values V_{z0} instead of guide field values. The left panel illustrates that the maximum $j_\parallel$ as a function of V_{z0} has a peak value max $(j_\parallel) \approx 1.8$, for $V_{z0} = 0.4$. It is expected that the maximum of $j_\parallel$ decreases with decreasing V_{z0}, which is consistent with the asymptotic in which $j_\parallel = 0$ for $V_z = 0$. The middle panel of Figure 4.5 demonstrates that large FACs are quite efficiently generated even for moderate perpendicular shear flow. As expected, the value of $\int j_\parallel dx$ increases with increasing V_{z0} and appears to converge toward a value of about 1.5. Note, however, that this evolution toward the asymptotic values takes a rather long time. The right panel of Figure 4.5 illustrates that the value of $\int (j_\parallel/B) \, dx$ shows an even stronger tendency to converge to a fixed value of close to 1.6 for all cases with shear flow of 0.2 and higher. Also the rise time is much shorter. Therefore, even moderate values of shear flow should generate significant ionospheric FACs. Comparing the results for a guide field with the inclusion of shear flow, it is noted that the maximum FAC density is about equal and occurs for $B_{z0} = 0.2$ and $V_{z0} = 0.4$. However, in general it appears that shear flow generates a larger value of $\int (j_\parallel/B) \, dx$ which is relevant for the ionospheric magnitude of the FAC. Although both cases, guide field and shear flow, generate significant FAC, total current that can be potentially observed in the ionosphere is typically larger in the presence of shear flow.

To conclude this examination of FAC generation is worth to consider the effects of Hall physics. Here the generation of FAC occurs without a guide field or shear flow for the bulk plasma. The magnetic field is frozen to the electron fluid, such that the motion by the electron current is sufficient to deflect the magnetic field into the invariant direction. The first two panels of Figure 4.6 show magnetic field B_z component and the FAC density $j_\parallel$ at $t = 150$ for case A. The bipolar structure of magnetic field B_z component extends all the way along the outflow region, instead of being localized in the vicinity of the reconnection region as observed by the GEM challenge [Otto, 2001]. The FAC density $j_\parallel$ is located along the entire boundary of the outflow region, and has the similar bipolar structure as B_z. The high resolution

Figure 4.5: The maximum FAC density $j_\parallel$ (left), $\int j_\parallel dx$ (middle), and $\int \left(j_\parallel / B \right) dx$ (right) for different shear flow magnitude V_{z0}.

one-dimensional simulation demonstrates that this bipolar structure is a part of a standing whistler wave. The physical explanation for this standing wave is as follows: The large scale jump conditions imposed by MHD is the same for Hall MHD, and this solution requires a strong current in the z direction to turn off the magnetic field B_y component. In MHD this is accomplished by slow switch-off shocks (in the symmetric case). However, in Hall MHD a large current density in the z direction combined with the frozen-in condition for electrons implies a deflection of the magnetic field into the z direction. This deflection apparently is the source of a standing whistler wave downstream of the maximum current density. The current density and FAC are much lower in Hall MHD than in MHD, because transition region depends on the wavelength of the whistle wave and becomes much wider. The one-dimensional results are similar to the two-dimensional results except for the multiple larger amplitude standing waves up- and downstream of the outflow boundary. These standing waves are not visible in the two-dimensional results due to a lack of resolution because the one-dimensional results use a resolution about 25 times better then in the two-dimensional simulation. It is not clear if this whistler wave can be observed by satellites, because the smaller amplitude waves can be concealed by the typical noise in space plasma and the waves could also be suppressed by ion gyro-viscous effects.

Figure 4.7 has the same structure as Figure 4.3, except for different Hall parameter l, and the left panel showing the maximum $|j_{\parallel}|$. The left panel illustrates that the maximum $|j_{\parallel}|$ as a function of Hall parameter l has a maximum at $l = 0.2$. This result is in contradiction to Ma and Lee's [2001] three-dimensional results in which FAC increases with increasing l (ion inertia scale). Naively it is expected the maximum $|j_{\parallel}|$ decreases with decreasing Hall parameter l, since there is no FAC for $l = 0$. However, a rigorous examination shows that this is not really correct. The figure shows that the maximum of $|j_{\parallel}|$ decreases for $l > 0.2$ which is the correct behavior for the following reason. The Hall MHD equations have no intrinsic scale except for the ion inertia scale λ_i. For example, a value of $l = 0.5$ implies the choice $L_0 = 2\lambda_i$. For a fixed ion inertia scale the cases with $l = 1$ and $l = 0.5$ only imply a different
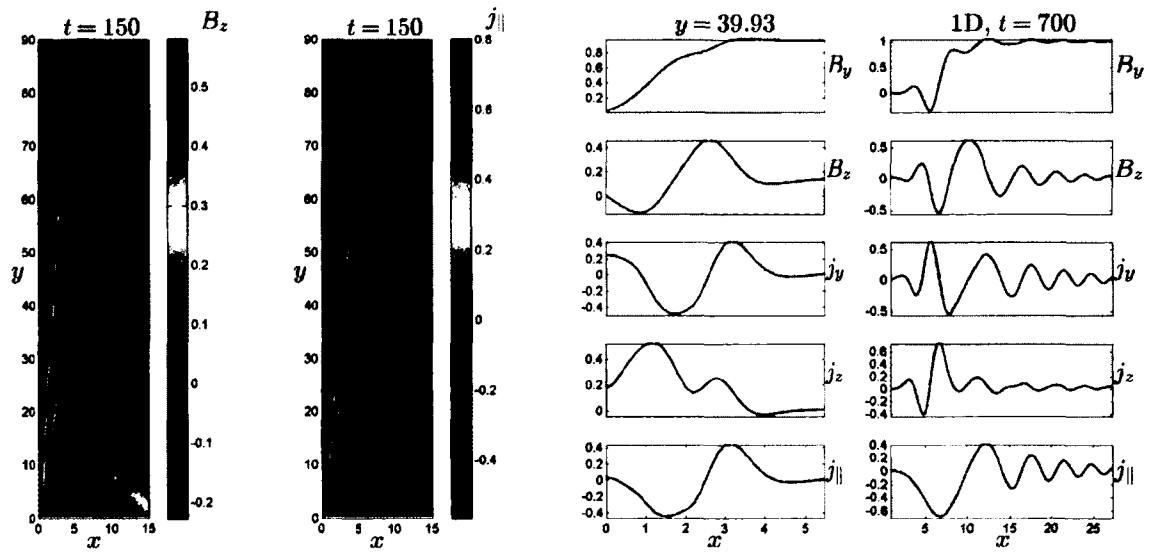
Figure 4.6: (From left) The first two panels shows magnetic field B_z component and FAC density $j_\parallel$ at $t = 150$ for case A. Black lines are open magnetic field lines (contours for vector potential). The five panels on the third column show the profiles of B_y, B_z, j_y, j_z, and $j_\parallel$ in a cut at $y = 39.93$, which is indicated by a purple line in left panel. The corresponding one-dimensional simulation results are presented in the right five panels.

normalization for the length scale L_0 for these cases. This can easily be removed by renormalizing the $l = 0.5$ case which increases the normalization of current density by a factor of two and therefore leads to a current of half its value in normalized units. This implies that the maximum current density should vary as l^{-1} for different values of l. At first glance one might conclude that this is wrong because this leads to an infinite current density in the limit $l \to 0$. However, this arbitrarily large current is also concentrated in arbitrarily thin region. This is not possible in a real physical system where gyro viscous and other dissipative effects limit current density and width. It is also not possible in a numerical simulation with limitations on resolution and dissipation of structure below a resolution threshold. This explains the maximum of $|j_\parallel|$ in Figure 4.7 because for $l < 0.2$ the resolution is insufficient or resistivity is too high to reflect the correct ion inertial dynamics. The reason for a decreasing maximum of $|j_\parallel|$ with increasing Hall parameter l is the increasing width of the current layer. Note, that the maximum value of $|j_\parallel|$ in the results presented here is much higher than in *Ma and Lee*'s [2001] three-dimensional study indicating that my resolution and resistivity is better and specifically for values of $l = 1$ appropriate to address the ion inertia physics.

Note, that the increase of the integrals $\left| \int j_\parallel dx \right|$ and $\left| \int j_\parallel B^{-1} dx \right|$ with the increasing Hall parameter is opposite to the change of $|j_\parallel|$. These integrals contain the product of length scale and current density, and this product is independent of a renormalization (the factors for length and current density cancel). However, a renormalization should be applied to the time scale. In other words, the time 2000 for $l = 0.8$ corresponds to the time 1000 for $l = 0.4$. This maps most of the curves except for $l \leq 0.1$ on top of each other. Finally it is noted that the values of $\left| \int j_\parallel dx \right|$ and $\left| \int j_\parallel B^{-1} dx \right|$ increases with the time. This is likely caused by the expanding standing whistler wave structure at the outflow boundary which contribute additional FAC. In summary, two-dimensional magnetic reconnection, including Hall physics leads to a strong generation of FAC, as long as the typical length scale is approximately the ion inertia scale.
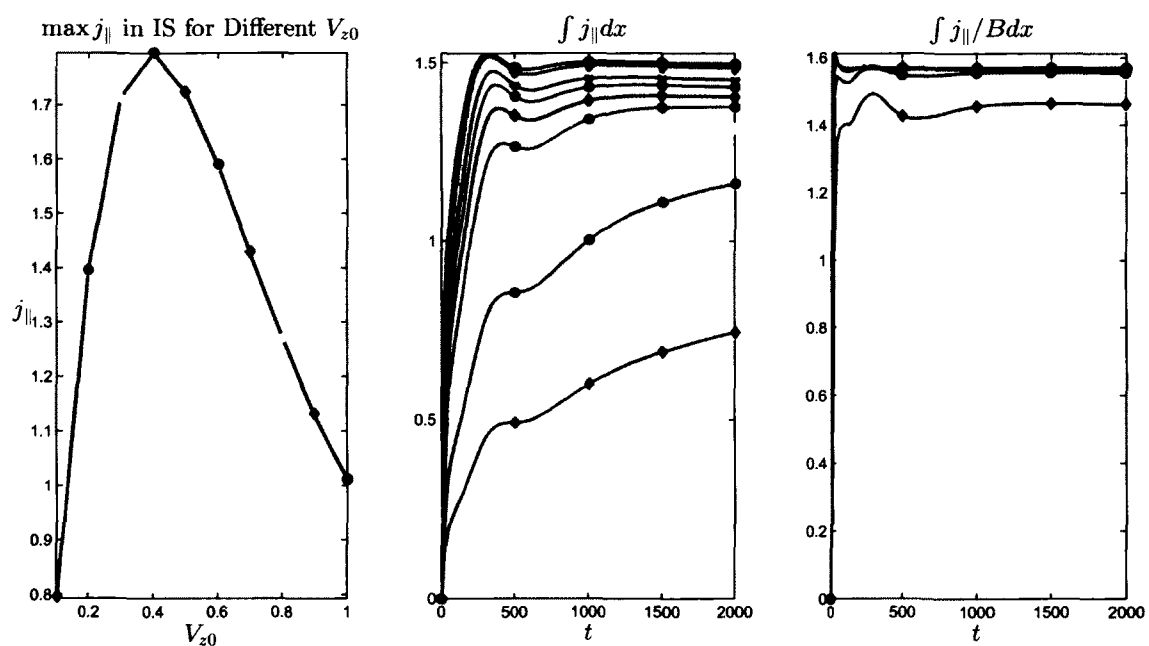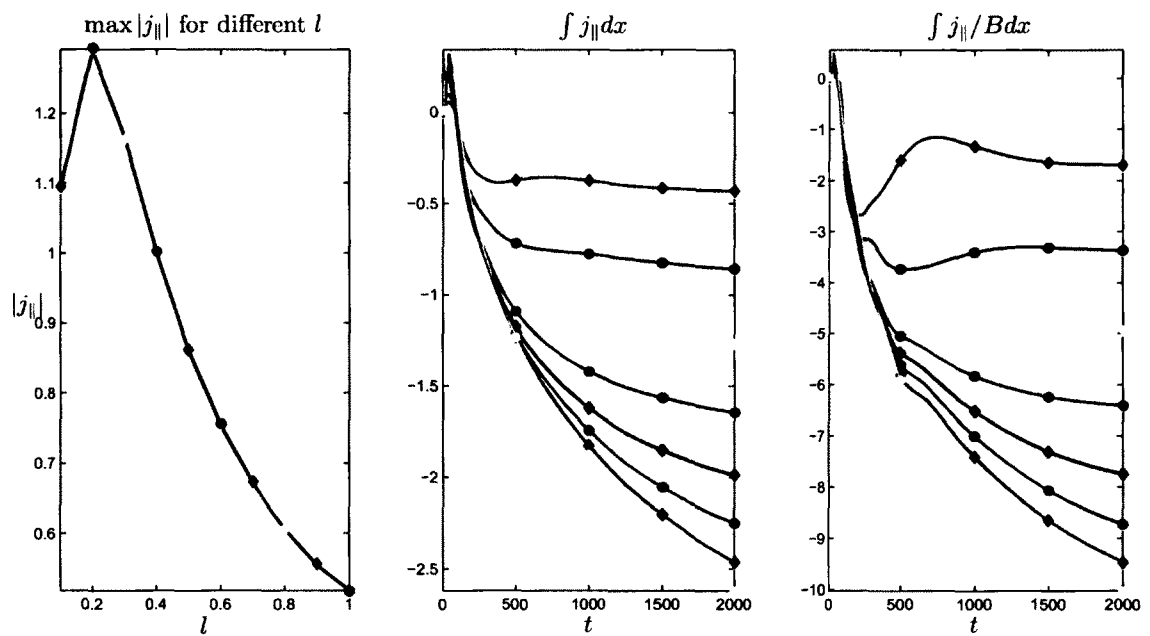
Figure 4.7: The maximum FAC density $|j_\parallel|$ (left), $\int j_\parallel dx$ (middle), and $\int (j_\parallel/B)\, dx$ (right) for different Hall parameter l.

It is well known, that rotational discontinuities, intermediate shocks, and switch-off shocks satisfy the Walen relation

$$\Delta \mathbf{V} = \Delta \mathbf{V}_A = \Delta(\mathbf{B}/\sqrt{\rho}) \tag{4.10}$$

for Alfvén waves. Figure 4.8 shows the Alfvén velocity change $|\Delta \mathbf{V}_A|$, ion velocity change $|\Delta \mathbf{V}|$, and electron velocity change $|\Delta \mathbf{V}_e|$, which illustrates that in Hall MHD both ions and electron also approximately satisfy the Walen relation. It is interesting that the small deviations between Alfvén speed variation and plasma bulk and electron velocity appear systematic up-and downstream of the outflow boundary. Such a systematic deviation has not yet been identified in observations but it might be interesting to examine whether such a systematic deviation from the Alfvén speed is present for the plasma bulk and electron velocity.

4.4 Summary and Discussion

Satellite observations provide evidence for the generation of FAC during magnetic reconnection. To better understand the mechanisms of FAC formation in two-dimensional magnetic reconnection, three selected simulation cases have been carefully studied.

In a configuration with a guide field component, FACs are present already in the initial state, such that the FACs observed in magnetic reconnection are partly a projection effect. However, guide field reconnection replaces the switch-off shocks of Petschek reconnection with an intermediate shock and a slow shock in the reconnection transition layer. All of FACs are generated in the intermediate shock layers. The slow shock layers are much thinner than the intermediate shock layers and ideally should satisfy the coplanarity condition such that the small associated FACs are either the result of a small deviation from the slow shock solution or a numerical artefact. For a small guide field component, a larger amount of FAC can be generated by reconnection because of the larger magnetic field rotation. Vice versa a large guide field implies less rotation of the magnetic field such that the projection effect is more important. Note, that a large guide field component indicates a small value of the
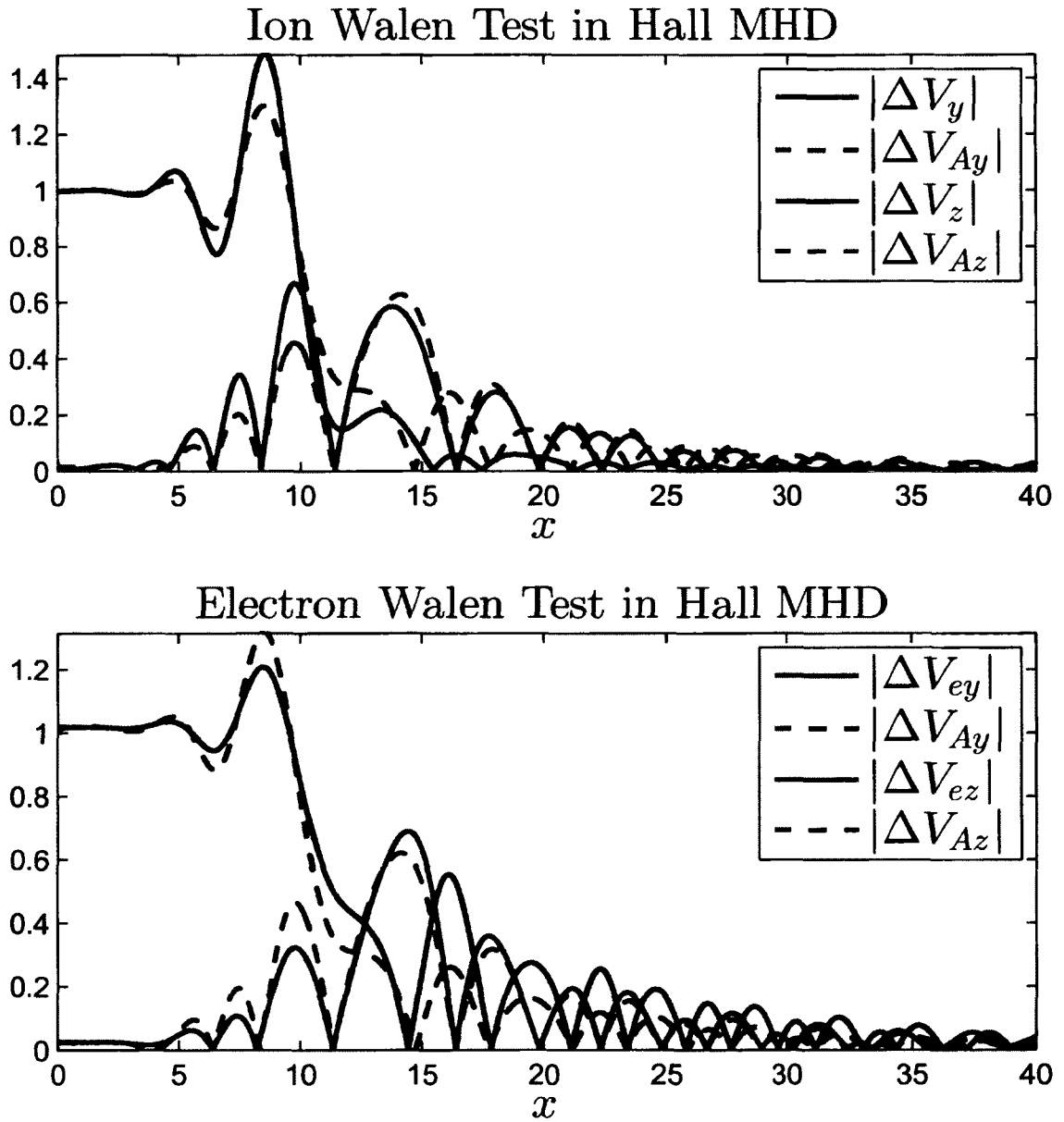
Figure 4.8: Hall MHD Walen test. Alfvén velocity change $|\Delta \mathbf{V}_A|$, ion velocity change $|\Delta \mathbf{V}|$, and electron velocity change $|\Delta \mathbf{V}_e|$.

anti-parallel magnetic field components, such that magnetic reconnection is expected be slow on the Alfvén time scale based on the total magnetic field. The total amount of FAC $\int j_\parallel /B dx$ into the ionosphere is not sensitive to the initial (or asymptotic) guide field value.

A perpendicular shear flow generates a B_z component and therefore FAC due to the frozen-in condition. The reconnection layer for a perpendicular shear flow configuration is similar to the reconnection layer in the guide field case. Since there is no FAC in the initial configuration such currents are solely generated by the intermediate shock in the reconnection geometry. The total amount of FAC $\int j_\parallel /B dx$ is largely independent of the initial shear flow for values equal or larger than 0.2. The current into the ionosphere is generally larger for shear flow than for guide field states.

The inclusion of Hall physics leads to the separation of ion and electron speed, and the frozen-in condition only applies to the electrons. The switch-off shock layer in the MHD is replaced by a standing whistler wave in the Hall MHD. The often-found B_z bipolar structure (also for FAC) is the primary part of this standing wave, and this bipolar structure extends all the way along the outflow region, instead of being localized in the vicinity of the reconnection region. Compared with previous three-dimensional simulation results, my results show a much higher maximum of $j_\parallel$ likely because of higher resolution. The maximum of $j_\parallel$ does not simply increase with increasing Hall parameter. This is because for a fixed ion inertia scale λ_i, a larger Hall parameter l implies a smaller normalization scale L_0, which increases the normalized current density J_0 and therefore decreases the current density measured in normalized units. Opposite to the change of $|j_\parallel|$, the integrals $|\int j_\parallel dx|$ and $|\int j_\parallel B^{-1} dx|$ increase with the increasing Hall parameter. And both ions and electrons approximately satisfy the Walen relation.

I note that this study is based on a symmetric configuration, while the real magnetopause is asymmetric, i.e., different densities, magnetic field magnitudes, and shear flow on the two sides of the boundary. However, qualitatively, my conclusions concerning the evolution of intermediate shocks and more importantly on FAC generation

by guide magnetic fields, velocity shear, and Hall physics are still applicable. This study also provides guidance and reference for more specific studies on the effects of asymmetry for the evolution of FAC.

Chapter 5

Interaction Between Magnetic Reconnection and Kelvin-Helmholtz Instability for Southward IMF Conditions: Kelvin-Helmholtz Type Perturbation

5.1 Introduction

Magnetic reconnection and Kelvin-Helmholtz (KH) instability are often considered as the two most important mechanisms for solar wind plasma access to the Earth's magnetosphere [*Axford*, 1964; *Dungey*, 1961]. Magnetic reconnection occurs in the presence of sufficiently large anti-parallel magnetic field components, e.g., in the case of southward interplanetary magnetic field (IMF) close to the equatorial magnetopause. Magnetic reconnection requires that the local width of the current layer is comparable to the diffusion width, i.e., ion or even electron inertia or gyro scale. A localized diffusion, which is caused by the micro-instabilities or electron pressure anisotropy, breaks down the so-called "frozen-in" condition and therefore changes the topology of the magnetic field, which allows the plasma access across the Earth's magnetospheric boundary. The efficiency of magnetic reconnection is measured by the rate of the magnetic flux transport (also called the "reconnection rate"). Both theory and simulation show that a fast (Petschek type) magnetic reconnection rate is about 0.1 [*Birn et al.*, 2001], which is based on a two-dimensional reconnection geometry assuming a unit distance into the invariant direction.

In comparison, KH modes occur for a sufficiently large shear flow [*Chandrasekhar*, 1961]. It has been demonstrated that plasma compressibility, a finite width of shear flow transition, and a parallel magnetic field component can stabilize the instability [*Chandrasekhar*, 1961; *Miura and Pritchett*, 1982]. Large velocity shear is typical for the Earth's magnetopause where the fast solar wind moves along the magnetosphere [*Miura*, 1982; *Miura and Pritchett*, 1982; *Miura*, 1984, 1992, 1995a; *Otto and Fairfield*, 2000; *Fairfield et al.*, 2000; *Hasegawa et al.*, 2004]. The total velocity difference between the solar wind plasma and the stagnant magnetospheric plasma varies from zero at the subsolar point to values close to the solar wind speed (about $100 \sim 1000\,\mathrm{km/s}$)

near the tailward flank boundary, which determines the various KH stability and growth rate. Since the KH instability is an ideal instability, mass transport across the magnetospheric boundary is not expected. However, it is demonstrated that in the resistive MHD, the nonlinear KH modes drive magnetic reconnection even for northward IMF conditions [*Otto and Fairfield*, 2000; *Fairfield et al.*, 2000; *Nykyri and Otto*, 2001, 2004; *Nakamura et al.*, 2006, 2008].

When the IMF is northward, magnetic reconnection cannot operate in the unperturbed magnetopause geometry because magnetic shear is small. Therefore, KH modes are the primary instability, and reconnection occurs only if the magnetic field has been strongly modified by the KH wave. For such conditions satellite observations provide strong evidence for the presence of nonlinear KH waves [*Fairfield et al.*, 2000; *Hasegawa et al.*, 2004]. However, for southward IMF conditions, both magnetic reconnection and Kelvin-Helmholtz (KH) modes can operate simultaneously, and there are only very few studies to examine this situation. Recently *Hwang et al.* [2011] presented first in situ observations of nonlinearly developed KH waves during southward IMF, and they suggested that under southward IMF KH vortices become easily irregular and temporally intermittent [*Hwang et al.*, 2011].

In a system which is unstable to both KH modes and tearing modes (linear stage of magnetic reconnection), the dominant dynamic process depends on the growth rates of these two modes and the respective initial perturbations [*Chen*, 1997]. In the nonlinear stage, the interaction of these processes is an open question that depends on the primary instability process. The results of this interaction are expected to depend strongly on the initial conditions or boundary conditions, namely conditions where (1) magnetic reconnection is the primary processes, or (2) KH modes represent the initial or primary process. Here I focus on the second condition.

Section 5.2 introduces the simulation method and boundary conditions used in this study. In Section 5.3, I first present the overall dynamics, then show the modulation of magnetic reconnection by the primary KH modes, and examine the influence of several critical parameters, i.e., the initial shear flow value, the guide magnetic field,

Table 5.1: Simulation Normalization

Magnetic field B_0	20 nT
Number density n_0	$10\,\text{cm}^{-3}$
Length scale L_0	640 km
Alfvén velocity V_A	$138\,\text{km} \cdot \text{s}^{-1}$
Time T_A	4.6 s

the KH wave number, and the inclusion of Hall physics. Section 5.4 presents a summary and discussion.

5.2 Numerical Methods

In this study I solve the full set of the three-dimensional normalized resistive MHD and Hall MHD equations as introduced in Chapter 2. The values for the normalization of the simulation units are summarized in Table 5.1.

I present the results from a series of simulation cases to study the interaction between magnetic reconnection and KH modes. The simulation domain is a volume with $|x| \leq L_x = 30$, $|y| \leq L_y = 20$, and $|z| \leq L_z = 40$, and is resolved by using $103 \times 203 \times 103$ grid points with a non-uniform grid along the x and z directions. For MHD cases, the Hall parameter is set to $l = 0$, and for the Hall MHD cases, the Hall parameter is chosen as $l = 0.6$, which implies a realistic ion inertia scale of 384 km at the magnetopause. To sufficiently resolve the diffusion region and Hall physics, the best resolution is set to 0.1 and 0.2 in the x and z direction in the diffusion region.

The initial equilibrium is a one-dimensional modified Harries sheet given by

$$B_x = 0, \tag{5.1}$$

$$B_y = B_{y0}, \tag{5.2}$$

$$B_z = - B_{z0} \tanh(x), \tag{5.3}$$

$$V_x = 0, \tag{5.4}$$

$$V_y = - V_{y0} \tanh(x), \tag{5.5}$$

$$V_z = 0, \tag{5.6}$$

$$p = p_\infty + 1 - B^2, \tag{5.7}$$

$$\rho = \rho_0 + \delta\rho \tanh(x), \tag{5.8}$$

where $B_{z0} = \pm 1$ for dawn and dusk case, respectively, $p_\infty = 0.25$, $\rho_0 = 1$, $\delta\rho = 0.1$. B_y represents the guide field and V_{y0} is the magnitude of shear flow. For convenience, I use the fast mode Mach number $M_f = V_{y0}/V_f$ to represent this speed, where $V_f = \sqrt{(B_{z0}^2 + \gamma p_\infty/2)/\rho_0} = 1.1$ is the average fast mode speed. Since the growth and evolution of KH waves strongly depends on the initial shear flow magnitude V_{y0}, which drives the instability, and on the magnitude B_{y0} of the magnetic field along the wave vector, which can stabilize the mode, I choose these in the range $M_f \in [0, 0.9]$ and $B_{y0} \in [0, 0.4]$. The reference case uses $B_{z0} = 1$, $B_{y0} = 0$, and $V_{y0} = 0.5$. Figure 5.1 shows a sketch of the 3D system, where magnetic shear, shear flow, and the structure of the KH wave are indicated.

In order to select the KH mode as the primary process, the system is triggered by a KH type perturbation, which is chosen as

$$\delta\mathbf{V} = [\nabla\Psi(x,y) \times \hat{\mathbf{e}}_z] f_1(z), \tag{5.9}$$

where

$$\Psi(x, y) = - (\delta v/n) \cos(ky) \tanh(kx), \tag{5.10}$$

$\delta v = 0.2$, n is the number of the KH modes in the system, and $k = n\pi L_y^{-1}$ is wave
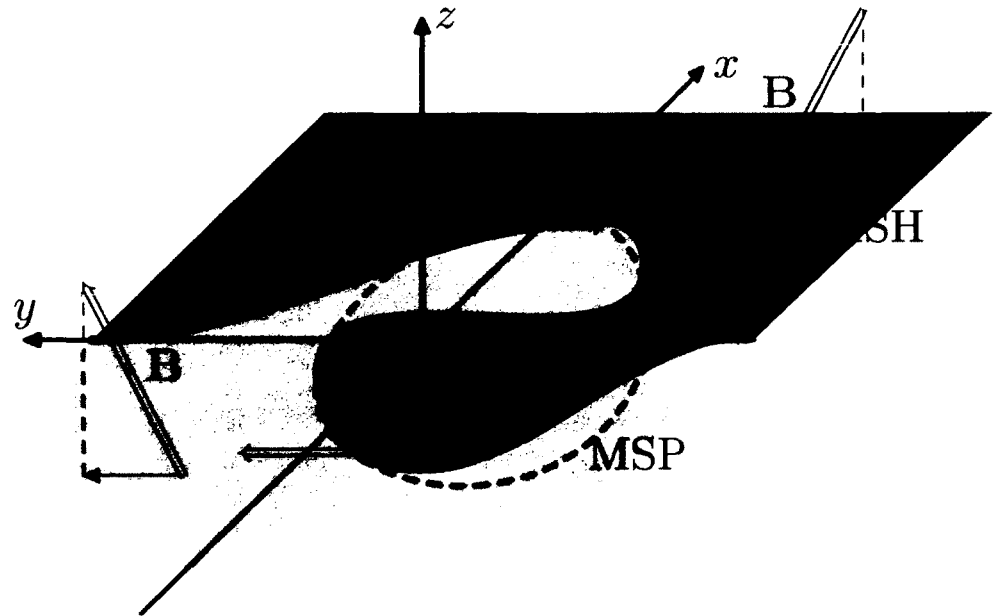
Figure 5.1: Sketch of the system geometry, where magnetic shear, shear flow, and the structure of the KH wave are indicated.

number. The function f_1 is given by

$$f_1(z) = \frac{1}{2}\left[\tanh\left(\frac{z+z_0}{d}\right) - \tanh\left(\frac{z-z_0}{d}\right)\right], \tag{5.11}$$

with $z_0 = 15$, and $d = 3$ and is used to localize the perturbation in the region where $z < |15|$. Note, that this perturbation is not a normal mode, i.e., a solution of the linearized equation, but the spectrum of the perturbation has a dominant contribution to the normal mode with the chosen wave number.

It is natural to use periodic boundary conditions along the y direction. Free boundary $\partial_x = 0$ conditions are applied in the x direction. However, the simulation box is chosen sufficiently wide that boundary effects can be ignored. An artificial friction term $-\nu(z)\left[\rho\mathbf{V} - \rho(0)\mathbf{V}(0)\right]$ is added on the right-hand side of the momentum equation, where $\rho(0)$, and $\mathbf{V}(0)$ are the initial plasma density and velocity,

respectively. The friction coefficient is localized near the z boundary and given by

$$\nu\left(z\right) = \frac{\nu_0}{2}\left[2 - \tanh\left(\frac{z + z_\nu}{dz_\nu}\right) + \tanh\left(\frac{z - z_\nu}{dz_\nu}\right)\right],\qquad(5.12)$$

$\nu_0 = 1$, $z_\nu = 0.75L_z$, and $dz_\nu = 3$. This form of a friction term introduces a magnetic line tying on either side of the magnetopause close to the z boundaries to mimic the fact that the magnetosheath magnetic field lines are moving with the solar wind, and that magnetospheric field footprints stick to the Earth's ionosphere (i.e., at large distances from the equatorial plane).

The resistivity in the magnetosphere is almost zero. Therefore, the current density can assume in principle an arbitrarily high value. However, a large current density is equivalent to a large current carrier drift velocity $\mathbf{V}_d = \mathbf{V}_i - \mathbf{V}_e$, where $\mathbf{V}_i$ is ion velocity, and $\mathbf{V}_e$ is electron velocity. When the drift velocity $\mathbf{V}_d$ is faster than some typical value, such as the ion-acoustic speed, micro-instabilities lead to turbulence limiting a further increase of the drift velocity $\mathbf{V}_d$. This implies a loss of momentum of the current carriers which is equivalent to a resistivity. Thus, in the simulation, a resistivity is switched on only when the drift velocity $|\mathbf{V}_d|$ is faster than a critical speed $v_c = \alpha c_s$, where $c_s = \sqrt{(\gamma p) / (2\rho)}$ is the ion-acoustic speed, and α is of order unity ($\alpha = \sqrt{4/\gamma}$) when the ion inertia scale is of the order of the normalization length L_0. In reality α is determined by the onset conditions for current driven turbulence in a strong current. Since the exact choice has minor influence on the macroscopic dynamics, it is used in the model as a free parameter to adjust magnetic reconnection onset condition. In the simulation, three resistivity models are applied, which are given by:

$$\text{Model 1:}\qquad \eta_1 = \eta_0\sqrt{j^2 - j_c^2}H\left(j - j_c\right) + j_b,\qquad(5.13)$$

$$\text{Model 2:}\qquad \eta_2 = \eta_0\sqrt{j - j_c}H\left(j - j_c\right) + j_b,\qquad(5.14)$$

$$\text{Model 3:}\qquad \eta_3 = \eta_0\left(j^2 - j_c^2\right)H\left(j - j_c\right) + j_b,\qquad(5.15)$$

where $\eta_0 = 0.05$, $H(x)$ represents a step function, $j_c = \rho v_c = \sqrt{2\rho p}$ the critical electric density, and $j_b = 0.001$ a background resistivity. However, the results indicate that

the overall dynamical properties are not sensitive to the specific resistivity model or the exact choice of the parameters in the model. Therefore, unless stated otherwise, I always use Model 1.

5.3 Simulation Results

5.3.1 Overall Dynamics

The KH mode growth rate and the reconnection rate are two of the most important physical quantities to characterize the dynamics of the system. Assuming an incompressible plasma, a discontinuous change of the tangential velocity, and the presence of different densities and tangential magnetic fields across a plasma boundary, the linear theory [*Chandrasekhar*, 1961] shows that the KH mode growth rate q is:

$$q = \sqrt{\alpha_1\alpha_2\left[(\mathbf{v_1} - \mathbf{v_2}) \cdot \mathbf{k}\right]^2 - \alpha_1\left(\mathbf{v_{A1}} \cdot \mathbf{k}\right)^2 - \alpha_2\left(\mathbf{v_{A2}} \cdot \mathbf{k}\right)^2}, \qquad (5.16)$$

where the indices refer to the two sides of the shear flow layer, $\alpha_i = \rho_i/(\rho_1 + \rho_2)$, $\mathbf{k}$ is the wave vector of the perturbation, and $\mathbf{v_{Ai}} = \mathbf{B_i}/\sqrt{\rho_i}$ is the Alfvén velocity.

Figure 5.2 shows that the logarithm of the amplitude of the perturbation $|\max(\delta v_x) - \min(\delta v_x)|$ increases linear with time for different resistivity models. In the linear stage (before 80 Alfvén times), the growth rate q is 0.043, which is lower than the theoretical value 0.078 from Equation (5.16). Two explanations for this lower growth rate are the finite width of shear layer and compressibility. A third important cause for stabilization is the localization of the wave in the z direction which leads to a loss of wave energy by radiation of Alfvén waves. In the three-dimensional configuration, the plasma velocity caused by the wave (v_x, v_y) is confined to a vicinity of the equatorial plane and drags the magnetic field lines across the boundary. However, the building magnetic tension in three-dimensions tends to pull the magnetic field line back to its original position (unless this field line is "broken" by magnetic reconnection). An alternative but equivalent explanation is the generation of Alfvén waves through the growing KH modes which travel in the positive and negative z directions and extract energy from the KH mode. The perturbation δv is comparable to the initial shear

flow magnitude V_{y0} after $t = 80$, and fully nonlinear KH vortices have formed. Figure 5.2 also shows that the growth rate of KH modes for different resistivity models is almost identical, which demonstrates that the overall KH mode dynamics is insensitive to the specific resistivity model.

The strong anti-parallel magnetic field represents a configuration that is susceptible to magnetic reconnection. The onset of large amplitude KH modes deform the current layer, which widens in the center of the vortex and thins in the spine of the KH wave (see Figure 5.1). As a result, the width of the current layer becomes comparable to the diffusion length, which satisfies the condition for the onset of resistivity and causes magnetic reconnection.

To identify the reconnected (open) magnetic flux, field lines are traced from the top boundary $(z = L_z)$. The open or reconnected field lines from the top boundary on the magnetosheath side $(x > 0)$ extend toward the equatorial plane, and connect to the field lines on the magnetosphere side, which extend back to the top boundary because the field magnetospheric field has the opposite direction along z. Thus, all open field lines started from the top boundary on the magnetosheath side $(x > 0)$ have endpoints also at the top boundary on the magnetosphere side $(x < 0)$. By integrating all of the positive (or negative) open flux (along z) at the top boundary, one can obtain the total reconnected flux

$$\Phi = \frac{1}{2} \int_{\text{open}} |B_z(x, y, L_z)| \, dx dy, \qquad (5.17)$$

where the integral is taken over the open flux at the top boundary plane. In order to compare with two-dimensional reconnection theory, this reconnection rate is normalized to the system size $2L_y$, Therefore, the normalized reconnection rate r is defined by

$$r = \frac{1}{2L_y} \frac{d\Phi}{dt}. \qquad (5.18)$$

Figure 5.3 presents the reconnected magnetic flux Φ and the normalized reconnection rate r for different resistivity models. It shows that magnetic reconnection strongly increases when the KH modes reach their nonlinear stage. The simulation assumes
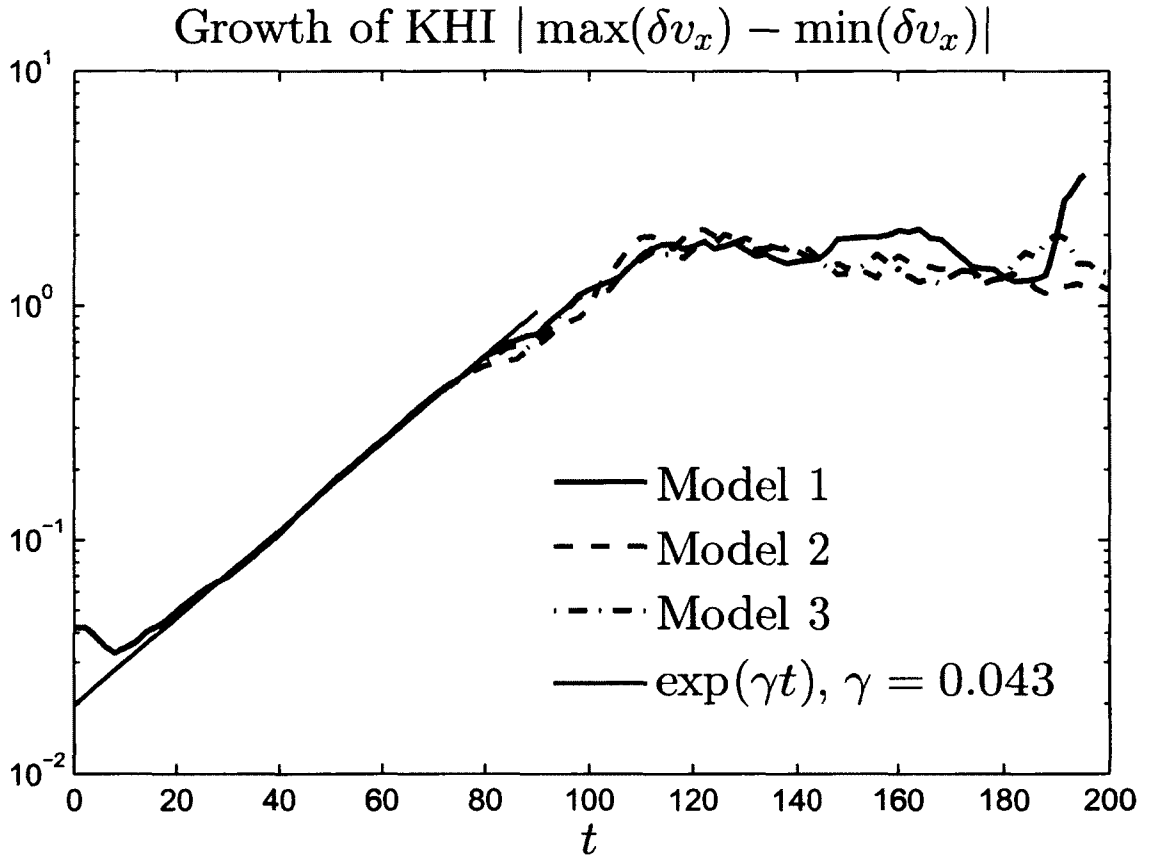
Figure 5.2: The growth of the KHI $|\max(\delta v_x) - \min(\delta v_x)|$ for the different resistivity models. The black solid line is the exponential curve fitting based on data from Model 1, which shows a growth rate of $q = 0.043$.

the highest rate is close to 0.1, which is similar to the Petschek reconnection rate, and is largely independent of the resistivity model. However, the normalized reconnection rate drops when a certain amount of magnetic flux has been reconnected, which indicates that the total amount of open flux is determined by the longest wavelength KH wave in the simulation box.

The frozen-in condition implies that the magnetic field is equipotential if the resistivity is 0. Any local diffusion and specifically magnetic reconnection, which breaks the frozen-in condition, generates a parallel electric field component $E_{\parallel}$. Therefore, the field-aligned electric potential difference

$$\Delta\phi = \int E_{\parallel}ds, \tag{5.19}$$

where ds is an infinitesimal length along the magnetic field line, indicates whether the magnetic field line goes through a diffusion region (newly reconnected) or not [*Hesse and Schindler*, 1988]. The colored area in Figure 5.4 illustrates the region of open flux at the top boundary. Here the left panel of the figure presents the field-aligned electric potential difference $\Delta\phi$ for open field lines for the reference case at $t = 164$. To improve contrast, the color-bar only covers $\Delta\phi < 0.088$. However, the maximum value of $\Delta\phi$ is 0.63, which appears dark red in the panel.

To identify the magnetic reconnection site, I record the lowermost point along the open field line (deflection point), since open field lines are deflected somewhere in the simulation system. Field lines may be deflected several times before they finally turn back to the top boundary. For newly reconnected flux, which is still connected to the dominant diffusion regions and has a large field-aligned electric potential difference $|\Delta\phi|$, the deflection point is the location of the lowermost reconnection site along this field line. The plot on the right side in Figure 5.4 presents the z coordinate of these deflection points.

Magnetic field lines near the open-close flux boundary $x \approx |7.5|$ are expected to be newly reconnected, which is consistent with the largest field-aligned electric potential difference (dark red region and some folds in the color plots). The corresponding

Reconnected Magnetic Flux Φ

Reconnected Rate $(d\Phi/dt)(2L_y)^{-1}$
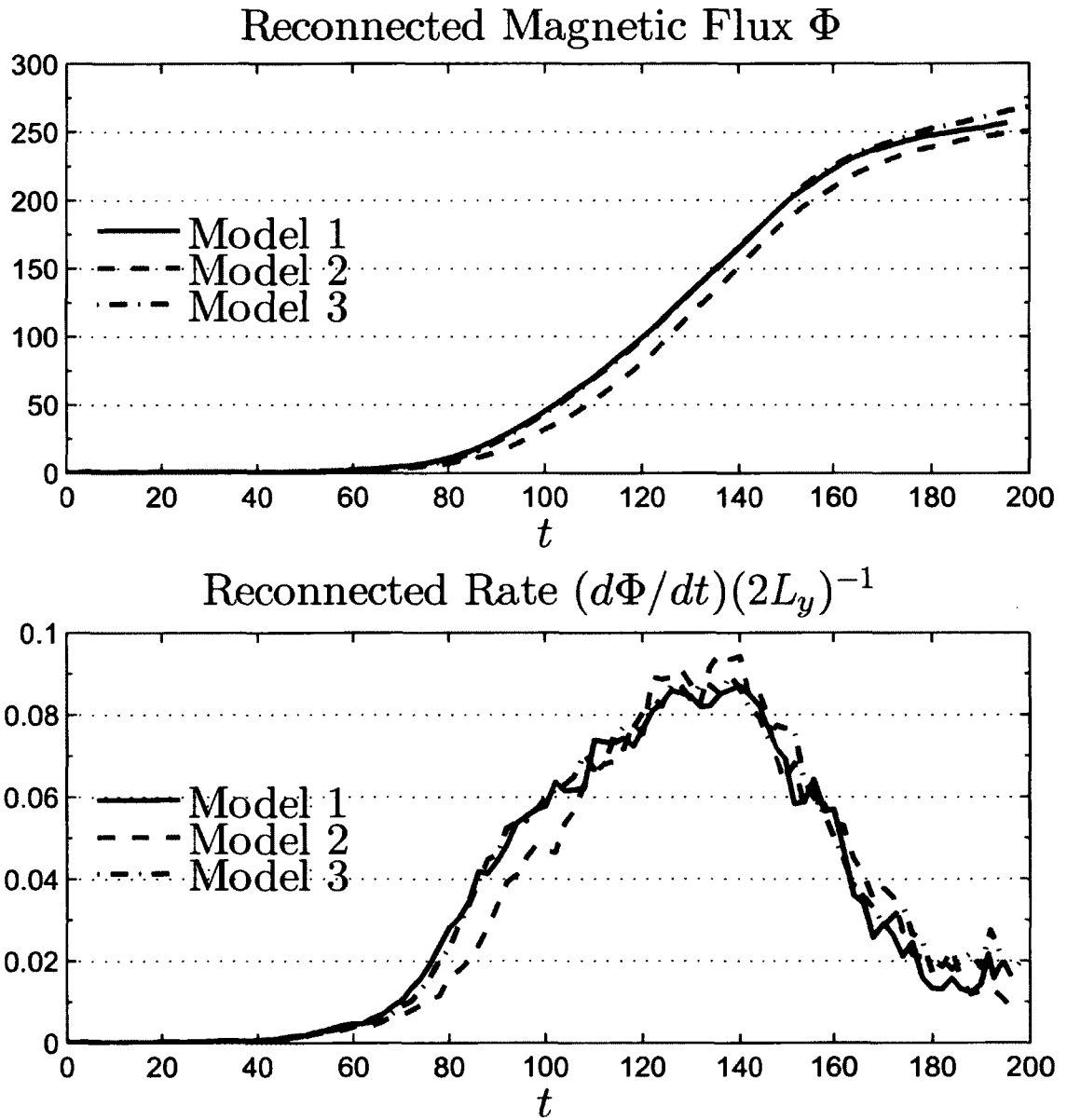
Figure 5.3: Reconnected magnetic flux Φ, and normalized reconnection rate r for the different resistivity models.

deflection points are close to the equatorial plane, which indicates that most of the magnetic flux is reconnected near the equatorial plane. Earlier reconnected magnetic field lines, whose foot-points at the top boundary are closer to the y axis, are deflected at a higher z position, which indicates that the reconnected field lines are convected toward the top boundary.

The reddish region ($\Delta\phi \approx 0.08$) inside the shear flow layer $|x| < 1$, where field lines are deflected near $z = 30$, indicates that there is another diffusion region at higher latitudes. However, the value of $\Delta\phi$ is one order of magnitude lower than those near the equatorial plane. Therefore, this higher latitude reconnection only has secondary effects for the dynamics of the system.

To demonstrate that the location of the diffusion region is indeed near the equatorial plane, I also present the field-aligned electric potential difference $\Delta\phi$ (left) and the magnetic field B_z component (right) for the reference case at $t = 164$ in a cut at $z = 1$ close to the equatorial plane in Figure 5.5. The large magnitude of the field-aligned electric potential difference $|\phi|$ is highly consistent with the low $|B_z|$ region, which demonstrates that magnetic reconnection is strongly influenced by KH modes. The results also confirm that magnetic reconnection takes place mainly in the spine of the nonlinear KH wave. The patchy pattern of the field-aligned electric potential difference $\Delta\phi$ inside of the KH vortex implies the onset of patchy reconnection associated with multiple current layers, which also contributes the normalized reconnection rate.

For a better representation of the diffusion region, I present the resistivity in projections on the xy and xz planes at $t = 164$ for the reference case in Figure 5.6. The color index is on a log-scale, and the isosurface uses $\eta = 10^{-1.75} \approx 0.018$. The resistivity is mostly enhanced close to the equatorial plane, consistent with my previous analysis. The pattern of the resistivity distribution also indicates that the diffusion region is strongly modified and deformed by KH waves. The small diffusion region near the $(0, 10, 30)$ may correspond to the afore mentioned higher latitude reconnection. A possible scenario for this magnetic reconnection is the following. Earlier (old)
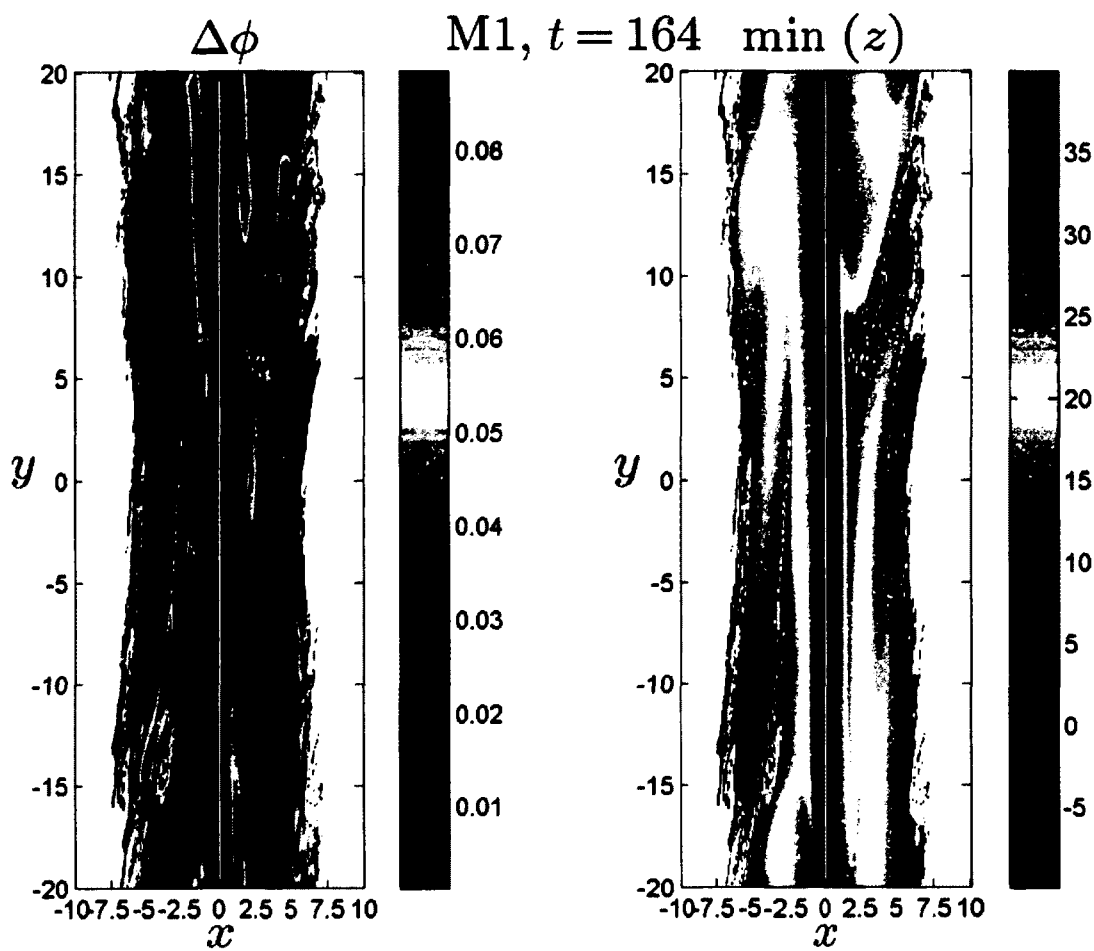
Figure 5.4:   Field-aligned electric potential difference $\Delta\phi$ and the z component of the deflection point min (z) for the reference case at $t = 164$ in a cut at $z = 40$ (top boundary).
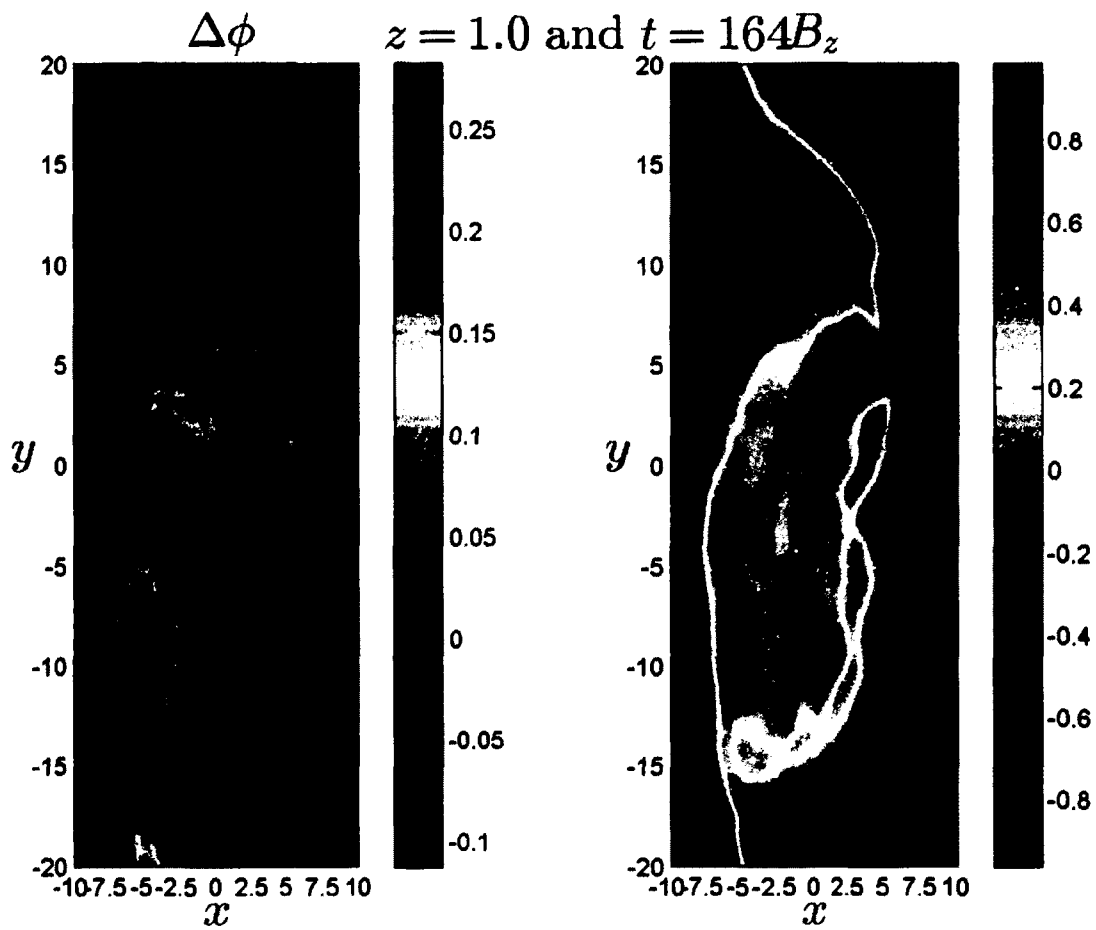
Figure 5.5: Field-aligned electric potential difference $\Delta\phi$ (left) and the magnetic field B_z component (right) for the reference case at $t = 164$ in a cut at $z = 1$ close to the equatorial plane.

reconnected flux has moved away from the equatorial plane and the corresponding foot-points on the two sides of the boundary have moved a large distance with the shear flow in to opposite y directions creating a large B_y component along the field lines. Newly reconnected flux does not pass this large y shear such that the interaction of older open flux and newly reconnected flux can generate significant current layers caused by the different B_y components. This may be further amplified locally through KH waves and cause the higher latitude reconnection. However, this magnetic reconnection only involves the open magnetic field lines, which does not change the normalized reconnection rate.

5.3.2 Influence of the Shear Flow Magnitude

The shear flow magnitude V_{y0} is a critical value for KH modes. The linear theory for KH growth rate Equation (5.16) shows a KH mode growth rate q proportional to the shear flow magnitude V_{y0} for any arbitrary value, which, however, is not the case for a three-dimensional compressible finite width system. Figure 5.7 shows the KH instability growth rate q (top), reconnected magnetic flux Φ (middle), and normalized reconnection rate r (bottom) for different shear flow magnitude V_{y0}, which ranges from 0 to $0.9V_f$. It demonstrates that a low critical shear flow magnitude $V_{lc} \in (0.2, 0.3)\,V_f$ is required to overcome compressibility and magnetic field tension. The KH mode growth rate q increases linearly with the shear flow magnitude V_{y0} above this lower threshold, however, it becomes insensitive to the shear flow magnitude V_{y0} when it reaches some saturation value q_s (about 0.045). When the shear flow magnitude V_{y0} is close to the fast mode speed V_f, information cannot propagate anymore from the upstream obstacle (vortex) to the downstream (opposite side) such that the KH growth is switched off. Both the reconnected flux Φ and the reconnection rate r show a strong correlation with the KH mode growth rate q (or initial value of the shear flow V_{y0}). For $V_{y0} < V_{lc}$, reconnected flux Φ and reconnection rate r are negligible, which indicates that reconnection close to the sub-solar region is not likely caused by KH modes. For KH mode growth rates q lower than the saturation value q_s, the vortex
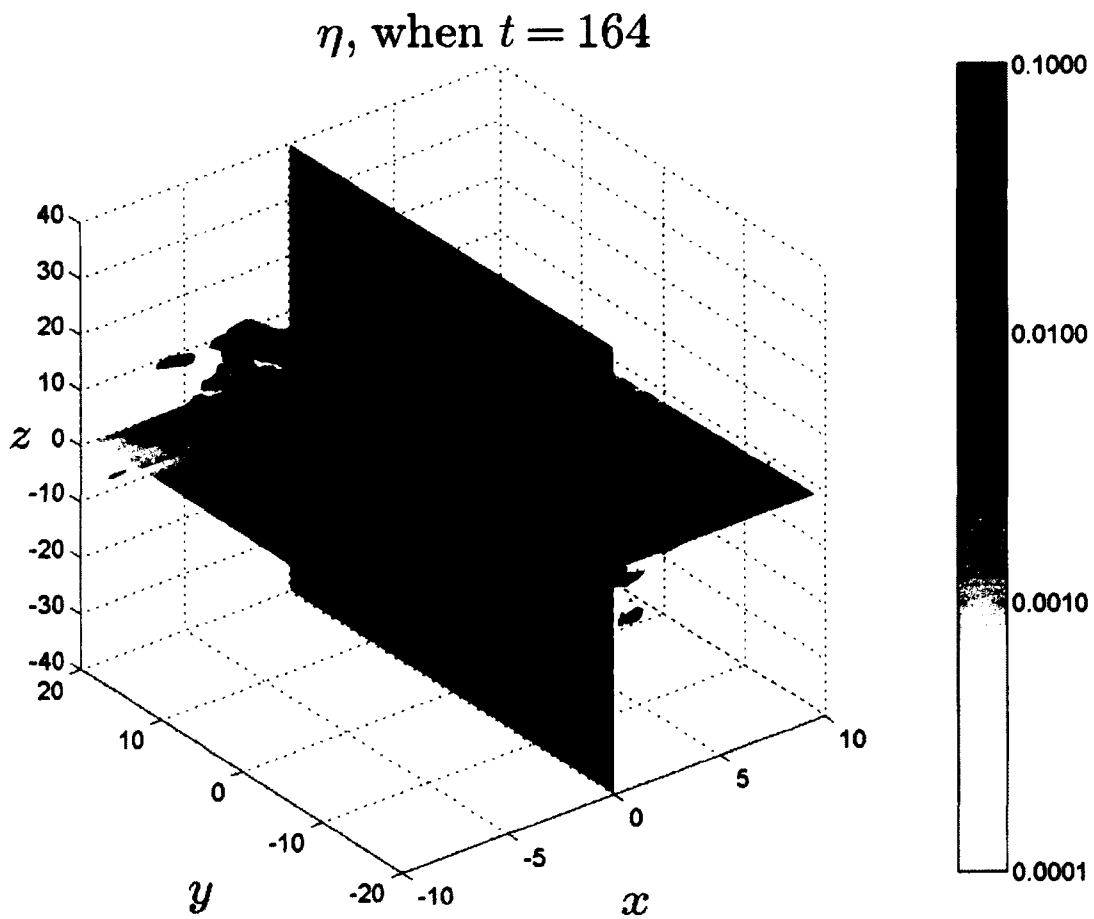
Figure 5.6: Distribution of resistivity η in a three-dimensional view.

size increases with larger shear flow magnitude, and therefore both reconnected flux Φ and normalized reconnection rate r increase. When the KH mode growth rate q is close to the saturation value q_s, the reconnected flux Φ and normalized reconnection rate r also becomes insensitive to the shear flow magnitude V_{y0}. Note, that the initial configuration used an under critical width of the current sheet, meaning that no resistivity is switched on initially. Otherwise reconnection would have started from the beginning of the simulation.

5.3.3 Influence of the Guide Field Component

Magnetic reconnection without guide field is a singular situation in space plasma system. A guide field component is present almost everywhere at the dayside magnetopause. In the considered configuration, this guide field component (magnetic field B_y component) is parallel to the direction of the shear flow. Thus, it can decrease the KH mode growth rate. Figure 5.8 shows the linear growth rate of the KH instability q (top), reconnected magnetic flux Φ (middle), and normalized reconnection rate r (bottom) for different initial guide components B_{y0} varying from 0 to 0.4 with a shear flow magnitude $M_f = 0.5$ (the cut-off value is $B_y = 0.49$ in this condition). The KH instability growth rate q decreases with increasing initial guide field value B_{y0} consistent with the linear theory. The total reconnected magnetic flux Φ and maximum normalized reconnection rate r also decrease with increasing guide field value B_{y0}, except for the $B_{y0} = 0$ case. Here the maximum normalized reconnection rate is a little lower than in the $B_{y0} = 0.1$ case although reconnection starts a bit earlier to increase. This indicates that a small guide field has minor influence and might even aid KH modes to twist the magnetic field lines more easily, with a slight increase in the normalized reconnection rate. However, a sufficient guide field component clearly stabilizes the KH waves, which means that the system spends more time to reach its nonlinear stage and saturation occurs at a smaller amplitude and size of the KH vortex. Therefore, both the total reconnected magnetic flux Φ and the normalized reconnection rate r decrease. Especially, when the initial guide field value B_{y0} is close
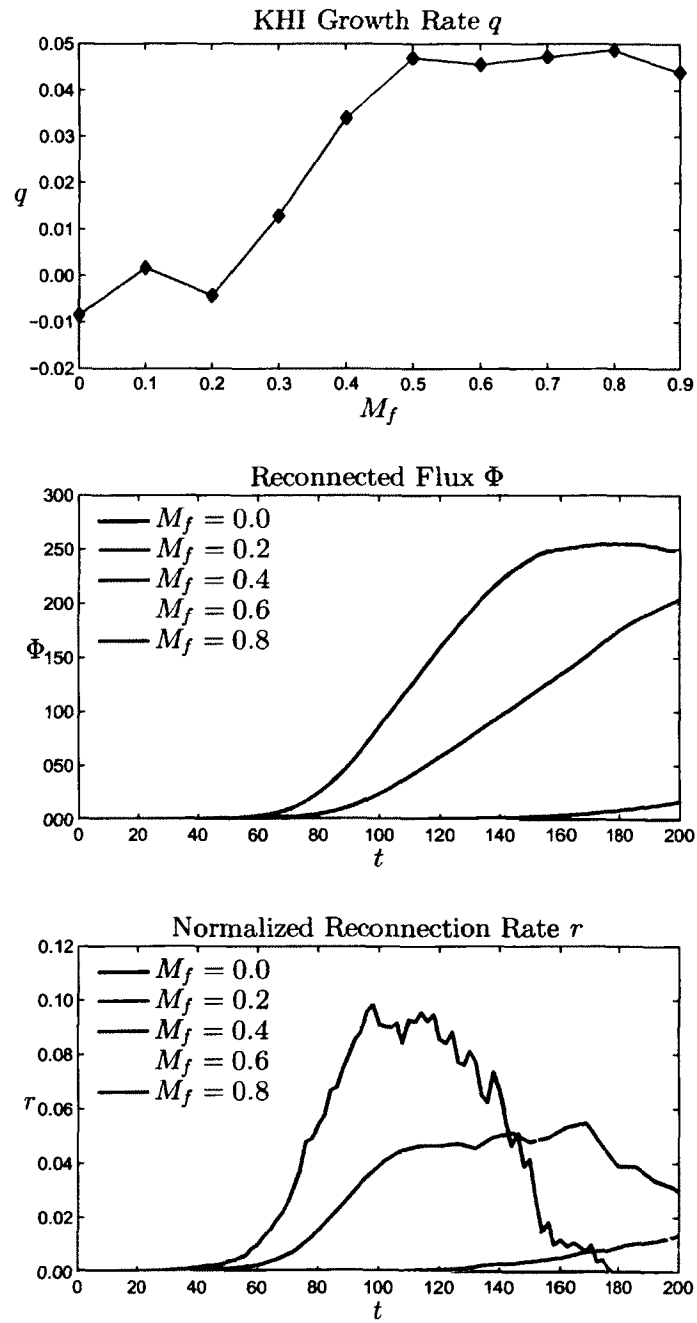
Figure 5.7: The KHI growth rate q (top), reconnected magnetic flux Φ (middle), and normalized reconnection rate r (bottom) for different initial speed of shear flow V_{y0}.

to the cut-off value ($B_{y0} = 0.4$ case), magnetic reconnection may not even be switched on.

5.3.4 Influence of the KH Mode Wave Number

The linear theory indicates that KH mode growth rate q is proportional to the KH wavenumber k [Chandrasekhar, 1961]. However, for the finite width shear flow, the fastest growth occurs for $ka \sim 0.5$ [Miura and Pritchett, 1982], where a is the width of the shear flow. For a multi-spectral system, the fastest growing modes dominate the dynamics at beginning, and at later times longer wavelengths, which involve more energy, becomes important. Thus in this study, I am not necessarily interested in the condition for fastest growth rate. Figure 5.9 shows the growth of the KHI $|\max(\delta v_x) - \min(\delta v_x)|$ (top), reconnected magnetic flux Φ (middle), and normalized reconnection rate r (bottom) for different KH wave-numbers (all other parameters are the same as for the reference case). In the linear stage, the KH growth rate q increases with increasing KH wavenumber k. Case $n = 8$ is slower than case $n = 4$, which is consistence with Miura and Pritchett's [1982] results. For all cases, the final KH wavelength is identical to the size (in y direction) of the simulation box. Notably, $n = 4$ and 2 case have more reconnected magnetic flux Φ than $n = 1$ case at the early stage. However, after $t = 120$ and 160 the $n = 1$ mode starts to dominate the total amount of reconnected flux. This indicates that although shorter wavelengths can generate faster growth and a larger normalized reconnection rate r, the total reconnected flux Φ is almost identical, because the total reconnected flux Φ is limited by the longest wavelength KH wave in the simulation.

The coalescence of KH vortices has been often reported and is considered as a mechanism of the evolution from shorter wavelength KH modes to the longer wavelength KH modes by different authors (see summary in [Miura, 1995b]). However, the growth of the longer wavelength KH modes and decay/diffusion of the shorter wavelength KH modes is another possible scenario for this evolution. To examine this evolution, I present the magnetic field B_z component at the equatorial plane for
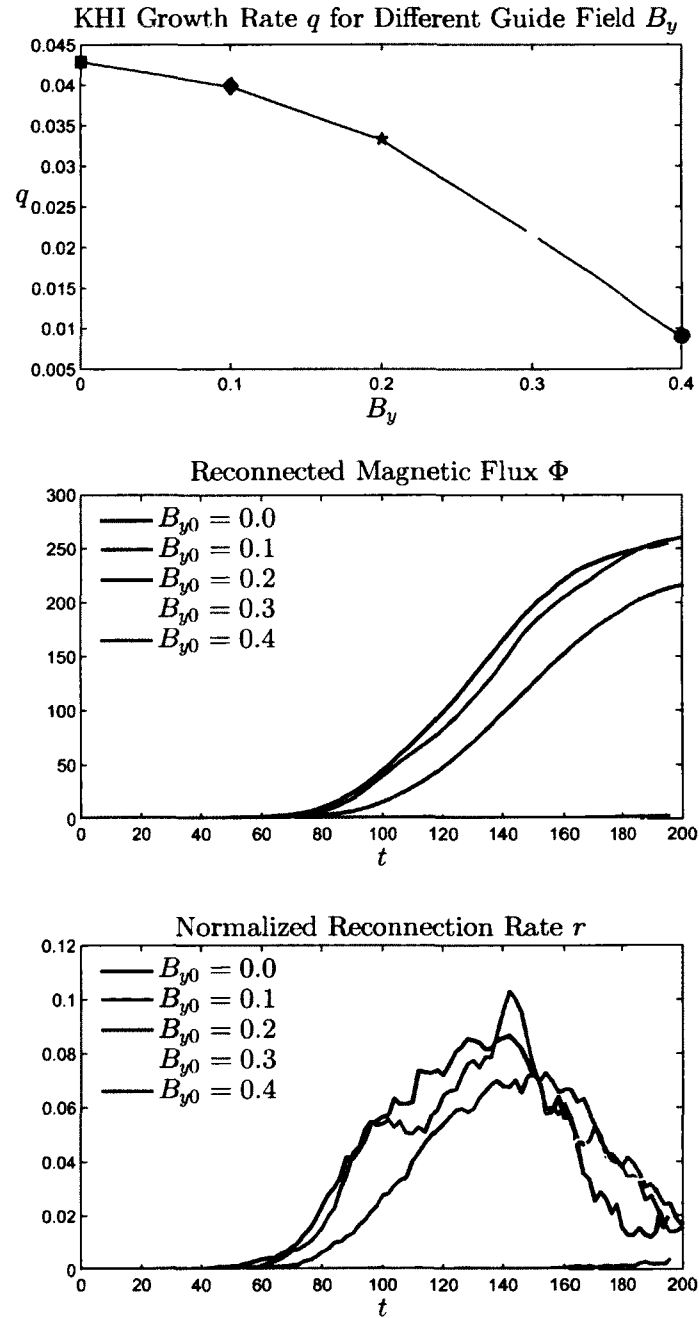
Figure 5.8: The KHI growth rate q (top), reconnected magnetic flux Φ (middle), and normalized reconnection rate r (bottom) for different initial guide field component B_{y0}.

Figure 5.9: The growth of the KHI $|\max(\delta v_x) - \min(\delta v_x)|$ (top), reconnected magnetic flux Φ (middle), and normalized reconnection rate r (bottom) for different KH wave-numbers.
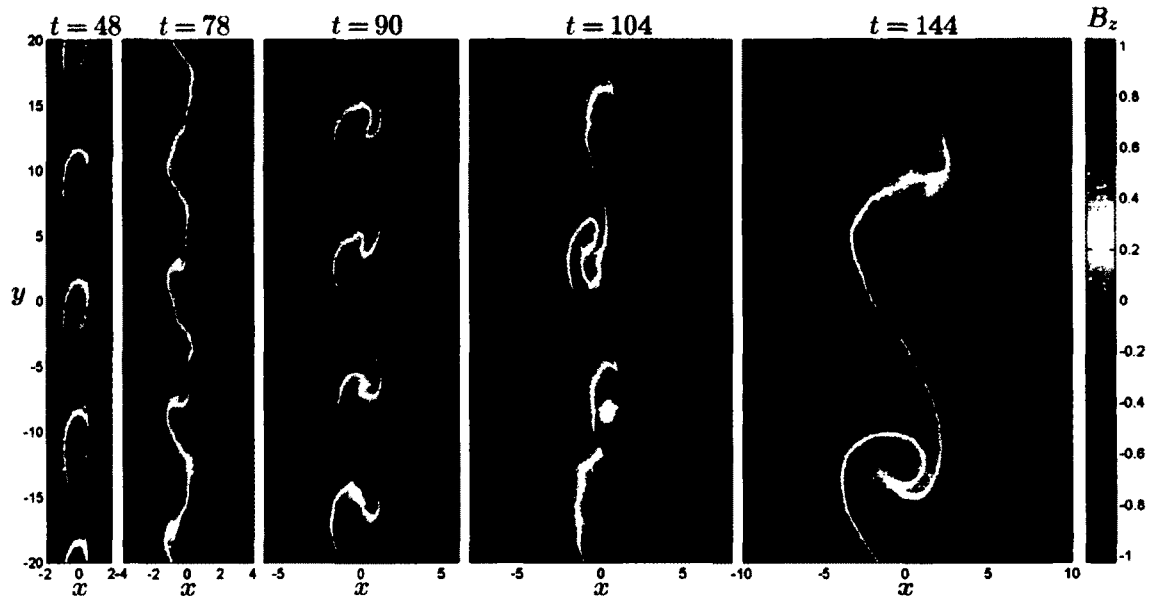
Figure 5.10: The magnetic field B_z component at equatorial plane for $t = 48$, 78, 90, 104, and 144 for $n = 4$ case.

$t = 48$, 78, 90,104, and 144 for $n = 4$ case. The four KH vortices observed at $t = 48$ decay at $t = 78$. However, at $t = 90$, $n = 4$ mode are formed again, which is not possible in two-dimensions. In three dimensions magnetic reconnection can thin the shear flow layer in the diffusion region after $t = 78$, which satisfies the KH onset condition again. These vortices decay at the boundary of the longer wavelength $n = 2$ mode at $t = 104$, and the $n = 2$ modes dominate the system at $t = 144$. Thus the evolution of the KH modes from shorter wavelength modes to the longer wavelength modes is likely caused by the diffusion/dissipation of smaller wavelength modes in a nonlinear state and ordinary growth and later dominance of the larger wavelength modes occurs instead of coalescence. Note, that the presence and decay of KH vortices is consistent with the normalized reconnection rate r oscillation (yellow line in bottom panel of Figure 5.9), which illustrates the strong influence on magnetic reconnection by the KH waves.

5.3.5 Influence of Hall physics

The typical width of the magnetospheric boundary is about several ion inertia scales, and magnetic reconnection onset requires a width of the current layer comparable or even smaller than the ion inertia scales. In this section, three selected cases are chosen to investigate effects caused by Hall physics. For computational reasons, a smaller simulation box $(L_y = 10)$ is used in these three cases. Hall term leads to the separation of the ion and electron velocity, and the frozen-in condition only applies to the electrons which carry most of the current in thin current sheets. Hall physics also generates a faster magnetic reconnection [*Birn et al.*, 2001; *Otto*, 2001], and *Huba* [1994] demonstrates that the Hall term breaks down the dawn-dusk symmetry. Therefore, the first case with Hall parameter $l = 0.6$ represents the dawn side $(B_{z0} = 1.0)$, and the second case with the same parameter, except represents the dusk side $(B_{z0} = -1.0)$. For comparison, the third case is the MHD case $(l = 0)$. All other parameters are the same as for the reference case. Figure 5.11 shows that the KH growth rate q in Hall MHD case is faster than the MHD cases. This is likely because the plasma momentum is mostly carried by ions, which are no longer frozen-into the magnetic field lines. Thus, the stabilization by the parallel magnetic field component appears reduced for the ions. Hall physics leads to a faster normalized magnetic reconnection rate r at beginning. However, in the nonlinear stage MHD magnetic reconnection is slightly faster, which is consistent with the growth of KH modes. The overall evolution does not show a significant dawn-dusk asymmetry, although, magnetic reconnection on the dawn side $(B_{z0} = 1.0)$ is slightly faster than on the dusk side $(B_{z0} = -1.0)$.

5.4 Summary and Discussion

For southward IMF conditions, the interaction between KH modes and magnetic reconnection is important to understand because it can potentially determine the plasma transport across the Earth's magnetospheric boundary. Here I have examined this interaction systematically for conditions in which KH waves are the primary
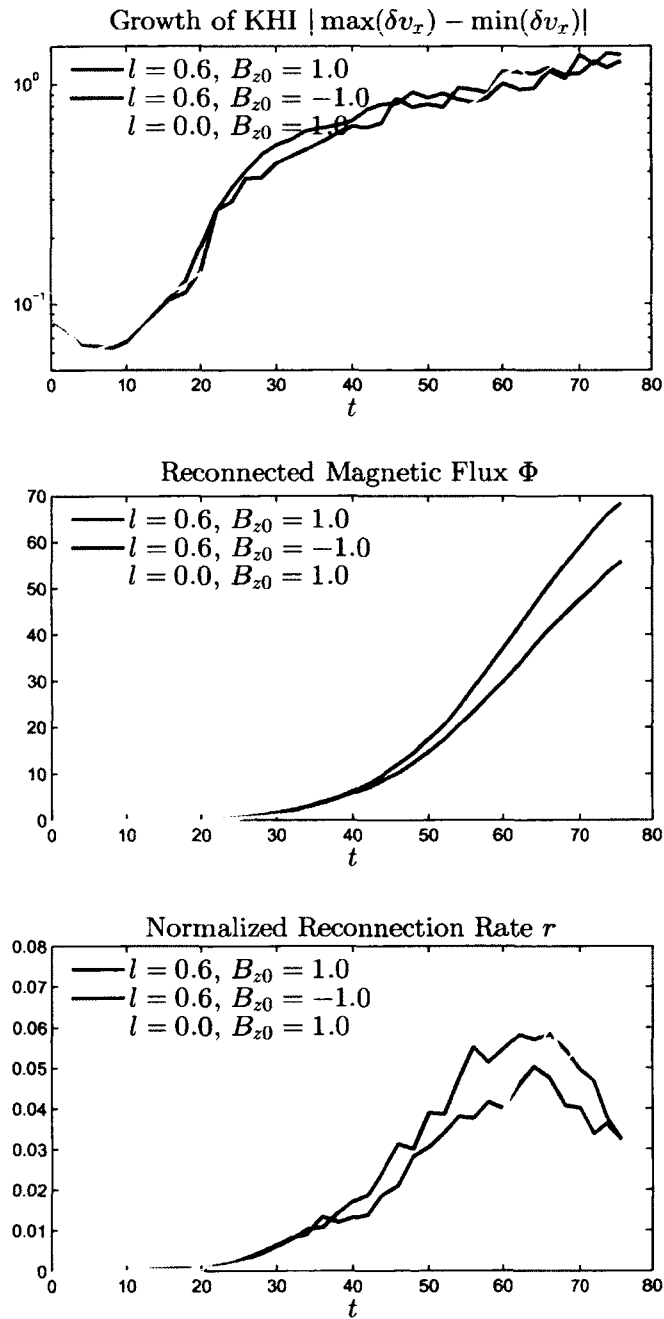
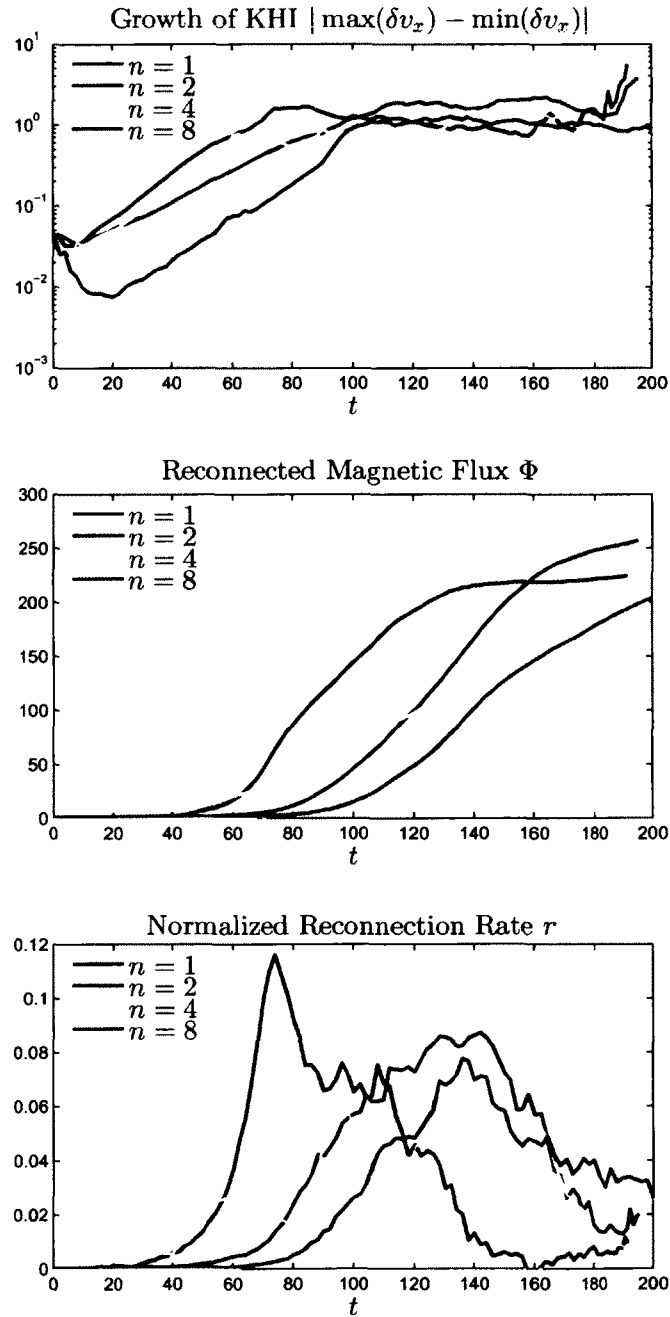Figure 5.11: The growth of the KHI $|\max(\delta v_x) - \min(\delta v_x)|$ (top), reconnected magnetic flux Φ (middle), and normalized reconnection rate r (bottom) for different Hall parameter and B_{z0}.

instability process in this interaction. My main results can be summarized as follows. The growth rate of three-dimensional KH waves is smaller than linear theory predicts because the simulations include compressibility, the finite width of shear flow layer, and a three-dimensional localization of the KH waves. A low critical threshold of the shear flow magnitude V_c is required to cause onset of the KH instability. Magnetic reconnection is driven and strongly modified by the nonlinear KH modes. A larger shear flow magnitude V_{y0} increases both the reconnected flux Φ and the normalized reconnection rate r. However, when the KH growth rate q reaches a saturation value q_c, the reconnected flux Φ, and the normalized reconnection rate r become insensitive to the specific shear flow magnitude V_{y0}. A sufficiently small guide field has only minor influence and may actually increase magnetic reconnection slightly. However, a sufficiently large guide field component clearly stabilizes the KH modes and therefore switches off magnetic reconnection. The relation between KH mode growth rate and KH wavenumber k is generally consistent with *Miura and Pritchett*'s [1982] results. A shorter wavelength KH mode has a higher KH growth rate q and reconnection rate r. During the evolution shorter wavelength modes decay, and longer wavelength modes grow to become the dominant modes. The normalized reconnection rate r strongly depends on the presence of nonlinear KH waves. However, the total reconnected flux Φ is determined and limited by the longest wavelength KH wave in the simulation. Hall physics increases both the KH growth rate q and normalized reconnection rate r, which is consistent with *Nykyri and Otto*'s [2004] results. The difference between dawn and dusk is minor in the simulation, which is contrary to *Huba*'s [1994] result. Note, that at the actual magnetopause, the density ratio between magnetosheath and magnetosphere is close to 10 ($\delta\rho = 0.82$), which is the value used by *Huba* [1994]. However, he used an overly large Hall parameter $l = 6$, which is not applicable to the Earth's magnetopause and may exaggerate the asymmetry. Therefore, the problem of a significant dawn-dusk asymmetry caused by Hall physics requires a realistic density ratio and Hall parameter, which will be part of my future work.

Chapter 6
Interaction Between Magnetic Reconnection and Kelvin-Helmholtz Instability for Southward IMF Conditions: Reconnection Type Perturbation

6.1 Introduction

A critical problem of magnetospheric physics is the plasma transport from the solar wind into the Earth's magnetosphere. Magnetic reconnection and viscous interaction are suggested as the two basic mechanisms for transport at the magnetospheric boundary [*Dungey*, 1961; *Axford*, 1964]. Fast magnetic reconnection generally requires large anti-parallel magnetic field components, which is satisfied at the equatorial magnetospheric boundary for southward interplanetary magnetic field (IMF) conditions. A central property of magnetic reconnection is the breakdown of the so called "frozen-in" condition by localized dissipation in the diffusion region, which changes the topology of the magnetic field lines and allows solar wind plasma access to the magnetosphere. A first stationary magnetic reconnection model was proposed by *Sweet* [1958] and *Parker* [1957], and later was modified by *Petschek* [1964] to account for the anticipated fast time scales observed in space plasmas. Theoretical analysis and numerical simulation show that a typical fast reconnection rate is about 0.1 [*Birn et al.*, 2001]. For northward IMF conditions, magnetic reconnection is expected to occur close to the geomagnetic cusp regions [*Adamson et al.*, 2012].

Close to the Earth's magnetopause, a large shear flow always exists due to the shocked solar wind streaming past the Earth's magnetosphere. The shear flow renders this boundary potentially unstable to the Kelvin-Helmholtz (KH) instability. Large scale nonlinear KH waves can generate a significant exchange of momentum across a physical boundary, thereby introducing a viscous interaction in the plasma participating in this interaction. This process as well as an efficient transport of energy across the plasma boundary have been demonstrated by a number of two-dimensional MHD simulations [*Miura*, 1982, 1984, 1987, 1992, 1996; *Miura and Pritchett*, 1982]. However, as an ideal instability, the KH instability does not violate the "frozen-in"

condition, such that no plasma transport is associated with this momentum transport in ideal MHD. Nevertheless, more recent two- and three-dimensional simulations for northward IMF conditions have demonstrated the formation of very thin current layers in the nonlinear vortices of KH waves. In resistive MHD these current layers force magnetic reconnection to operate which allows the plasma to cross the magnetospheric boundary [*Nykyri and Otto*, 2001; *Otto and Fairfield*, 2000]. Observational evidence for nonlinear KH waves during the northward IMF conditions has been reported by different authors [*Fairfield et al.*, 2000; *Otto and Fairfield*, 2000; *Hasegawa et al.*, 2004]. Recently *Hwang et al.* [2011] presented some first in situ observations of nonlinearly developed KH waves during southward IMF. "The analysis reveals a mixture of less-developed and more-developed KH waves that shows inconsistent variations in scale size and the magnetic perturbations in the context of the expected evolution of KH structures" [*Hwang et al.*, 2011]. "A coherence analysis indicates that the observed KH waves for southward IMF appear to be irregular and intermittent" [*Hwang et al.*, 2011].

The configuration, a largely anti-parallel magnetic field with a perpendicular shear flow has been studied by various authors using two-dimensional numerical simulations of reconnection an KH waves [*La Belle-Hamer et al.*, 1995; *Chen*, 1997]. However, the assumed two-dimensional configuration in *La Belle-Hamer et al.* [1995] excludes the KH modes because their **k** vector is in the invariant direction. This is different in three dimensions, where magnetic reconnection and KH waves can operate simultaneously. In a system which is unstable to both KH modes and tearing modes (linear stage of magnetic reconnection), the dominant dynamic process depends on the growth rates of these two modes and the respective initial perturbations [*Chen*, 1997]. In the nonlinear stage, the interaction of these processes is an open question that depends on the primary instability process. This question can be approached from two different angels, namely by assuming conditions where (1) magnetic reconnection is the primary processes, and (2) KH modes represent the initial or primary process. Here I focus on the first condition.

Table 6.1: Simulation Normalization

Magnetic field B_0	20 nT
Number density n_0	$10\,\mathrm{cm}^{-3}$
Length scale L_0	640 km
Alfvén velocity V_A	$138\,\mathrm{km\cdot s}^{-1}$
Time T_A	4.6 s

6.2 Numerical Methods

This study uses the full set of the three-dimensional normalized resistive MHD and Hall MHD equations as introduced in Chapter 2. The values for the normalization of the simulation units are summarized in Table 6.1.

I present results from a series of selected simulation cases to study the interaction between magnetic reconnection and KH modes. The simulation domain is a volume with $|x| \le L_x = 30$, $|y| \le L_y = 20$, and $|z| \le L_z = 40$, and is resolved by using $103 \times 203 \times 103$ grid points with a non-uniform grid along the x and z directions. To sufficiently resolve the diffusion region, the best resolution is set to 0.1 and 0.2 in the x and z direction in the vicinity of the current layer where reconnection is triggered. The initial equilibrium is a one-dimensional modified Harries sheet given by

$$B_x = 0, \tag{6.1}$$

$$B_y = B_{y0}, \tag{6.2}$$

$$B_z = -B_{z0}\tanh(x), \tag{6.3}$$

$$V_x = 0, \tag{6.4}$$

$$V_y = -V_{y0}\tanh(x), \tag{6.5}$$

$$V_z = 0, \tag{6.6}$$

$$p = p_\infty + 1 - B^2, \tag{6.7}$$

$$\rho = \rho_0 + \delta\rho\tanh(x), \tag{6.8}$$

where $B_{z0} = 1$, $p_\infty = 0.25$, $\rho_0 = 1$, $\delta\rho = 0.1$, B_y is the guide field, and V_{y0} is the

initial shear flow magnitude. For convenience, I use the fast mode Mach number $M_f = V_{y0}/V_f$ to represent this speed, where $V_f = \sqrt{(B_{z0}^2 + \gamma p_\infty/2)/\rho_0} = 1.1$ is the average fast mode speed. Since the growth and evolution of KH waves strongly depends on the initial shear flow magnitude V_{y0}, which drives the instability, and on the magnetic field magnitude B_{y0} along the wave vector, which can stabilize the mode, I choose these in the range $M_f \in [0, 1]$ and $B_{y0} \in [0, 0.5]$. The reference case uses $B_{y0} = 0$, and $M_f = 0.5$. Figure 6.1 shows a sketch of the three-dimensional system, where magnetic shear, shear flow, and the source region for reconnection are indicated.
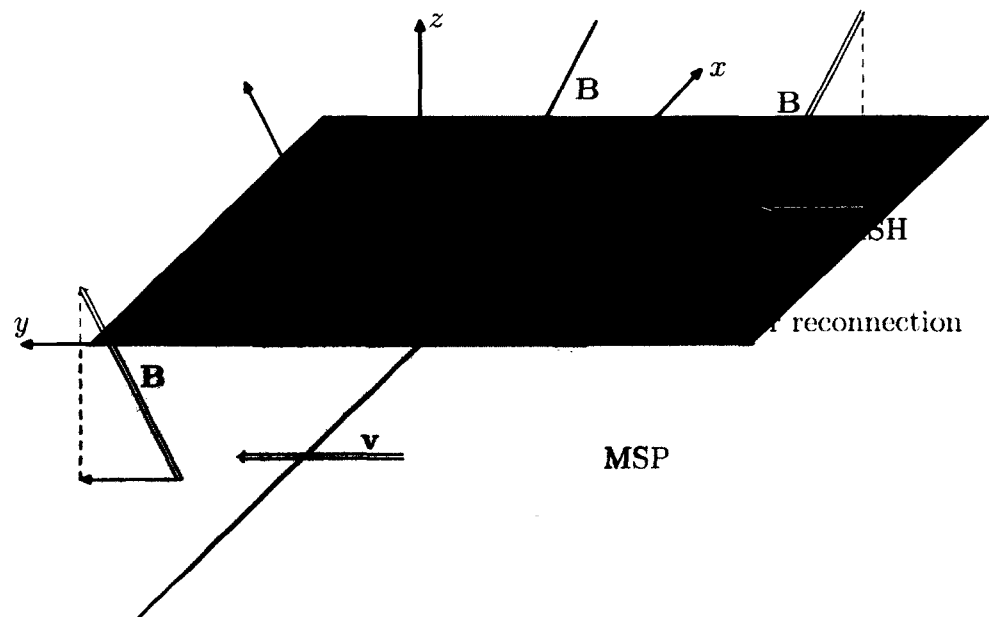
Figure 6.1: Sketch of the system geometry, where magnetic shear, shear flow, and the source region for reconnection are indicated.

In order to select magnetic reconnection as the primary process, reconnection is initiated in a source region by a magnetic perturbation which is chosen as

$$\delta \mathbf{B} = [\nabla A\,(x, z) \times \hat{\mathbf{e}}_y]\,f_2\,(y)\,, \tag{6.9}$$

where

$$A(x, z) = \delta B \cosh^{-2}(x) \cosh^{-2}(z/2),$$ (6.10)

and $\delta B = 0.5$. The function f_2 is given by

$$f_2(y) = \frac{1}{2} \tanh^{-1}\left(\frac{y_0}{d}\right)\left[\tanh\left(\frac{y + y_0}{d}\right) - \tanh\left(\frac{y - y_0}{d}\right)\right],$$ (6.11)

with $y_0 = 10$, and $d = 2$ and is chosen to localize the perturbation in the region where $y < |10|$. The relatively large magnetic perturbation is justified because large perturbations are common in the magnetosheath and a large perturbation accelerates the evolution of reconnection as the primary instability in this study.

The simulations use periodic boundary conditions along the y direction. Free boundary ($\partial_x = 0$) conditions are applied in the x direction. However, the simulation box is chosen sufficiently wide that boundary effects are negligible. An artificial friction term $-\nu(z)[\rho\mathbf{V} - \rho(0)\mathbf{V}(0)]$ is added on the right-hand side of the momentum equation, where $\rho(0)$, and $\mathbf{V}(0)$ are the initial plasma density and velocity, respectively. The friction coefficient is localized near the z boundary and is given by

$$\nu(z) = \frac{\nu_0}{2}\left[2 - \tanh\left(\frac{z + z_\nu}{dz_\nu}\right) + \tanh\left(\frac{z - z_\nu}{dz_\nu}\right)\right],$$ (6.12)

$\nu_0 = 1$, $z_\nu = 0.75L_z$, and $dz_\nu = 3$. This form of a friction term introduces a magnetic line tying on either side magnetopause close to the z boundaries to mimic the fact that the magnetosheath magnetic field lines are moving with the solar wind, and that magnetospheric magnetic field footprints stick to the Earth's ionosphere (i.e., at large distances from the equatorial plane).

The resistivity in the magnetosphere is almost zero. Therefore, the current density can assume in principle an arbitrarily high value. However, a large current density is equivalent to a large current carrier drift velocity $\mathbf{V}_d = \mathbf{V}_i - \mathbf{V}_e$, where $\mathbf{V}_i$ is ion velocity, and $\mathbf{V}_e$ is electron velocity. When the drift velocity $\mathbf{V}_d$ is faster than some typical value, such as the ion-acoustic speed, micro-instabilities lead to turbulence limiting a further increase of the drift velocity $\mathbf{V}_d$. This implies a loss of momentum of the current carriers which is equivalent to a resistivity. Thus, in my simulation,

a resistivity is switched on only when the drift velocity $|\mathbf{V}_d|$ is faster than a critical speed $v_c = \alpha c_s$, where $c_s = \sqrt{(\gamma p)/(2\rho)}$ is the ion-acoustic speed, and α is of order unity ($\alpha = \sqrt{4/\gamma}$) when the normalization length L_0 is of the order of the ion inertia scale. In reality α is determined by the onset conditions for current driven turbulence in a strong current. Since the exact choice has minor influence on the macroscopic dynamics, it is used in my model as a free parameter to adjust magnetic reconnection onset condition. In the simulation, three resistivity models are applied, which are given by:

$$\text{Model 1:} \quad \eta_1 = \eta_0 \sqrt{j^2 - j_c^2} H(j - j_c) + j_b, \tag{6.13}$$

$$\text{Model 2:} \quad \eta_2 = \eta_0 \sqrt{j - j_c} H(j - j_c) + j_b, \tag{6.14}$$

$$\text{Model 3:} \quad \eta_3 = \eta_0 \left(j^2 - j_c^2\right) H(j - j_c) + j_b, \tag{6.15}$$

where $\eta_0 = 0.05$, $H(x)$ represents a step function, $j_c = \rho v_c = \sqrt{2\rho p}$ the critical current electric density, and $j_b = 0.001$ a background resistivity. However, my results indicates that the overall dynamical properties are not sensitive to the specific resistivity model or the exact choice of the parameters in the model. Therefore, unless stated otherwise, I always use Model 1.

6.3 Simulation Results

6.3.1 Overall Dynamics

The reconnection rate is among the most important physical quantities to characterize the transport of magnetic flux at a magnetic boundary and it provides also insight into the plasma transport or plasma access from one side of the boundary to the other. To identify the reconnected (open) magnetic flux, field lines are traced from the top boundary ($z = L_z$). The open or reconnected field lines from the top boundary on the magnetosheath side ($x > 0$) extend toward the equatorial plane, and connect to the field lines on the magnetosphere side, which extend back to the top boundary because the field magnetospheric field has the opposite direction along z. Thus, all open field lines started from the top boundary on the magnetosheath side ($x > 0$)

have endpoints also at the top boundary on the magnetosphere side ($x < 0$). By integrating all of the positive (or negative) open flux (along z) at the top boundary, one can obtain the total reconnected flux

$$\Phi = \frac{1}{2} \int_{\text{open}} |B_z\,(x, y, L_z)|\,dx dy, \qquad (6.16)$$

where the integral is taken over the open flux at the top boundary. In order to compare with two-dimensional reconnection theory, this reconnection rate is normalized to the system size $2L_y$. Thus, the normalized reconnection rate r is defined by

$$r = \frac{1}{2L_y} \frac{d\Phi}{dt}. \qquad (6.17)$$

Figure 6.2 presents the reconnected magnetic flux Φ and the normalized reconnection rate r for different resistivity models. All other parameters are the same as for the reference case. The results demonstrate that magnetic reconnection is switched on at $t = 20$. The reconnected flux Φ increases with time and the simulation assumes the highest normalized reconnection rate of about 0.06 at $t = 100$. This is similar to the Petschek reconnection rate, and it is largely independent of the resistivity modes. However, the normalized reconnection rate drops when a certain amount of magnetic flux Φ (at about $t = 200$) has been reconnected, which indicates that the total mount of open flux is limited by the system.

Note, that the initial perturbation is not chosen to trigger the KH instability. However, the initial configuration is KH unstable, such that any fluctuation with a spectrum in y direction is expected to generate KH modes. Therefore, in the simulation both magnetic reconnection and KH modes operate simultaneously. The onset of magnetic reconnection changes the width of the shear flow, thus it changes the KHI onset condition. The nonlinear KH waves change in turn the width of the current layer, thereby changing conditions for magnetic reconnection. Figure 6.3 shows the magnetic field B_z component in the equatorial plane $z = 0$, for $t = 20$, 48, 90, 104, and 144 for the reference case. Initially, for this quasi-two-dimensional configuration, the source region for reconnection in the equatorial plane determines the location of
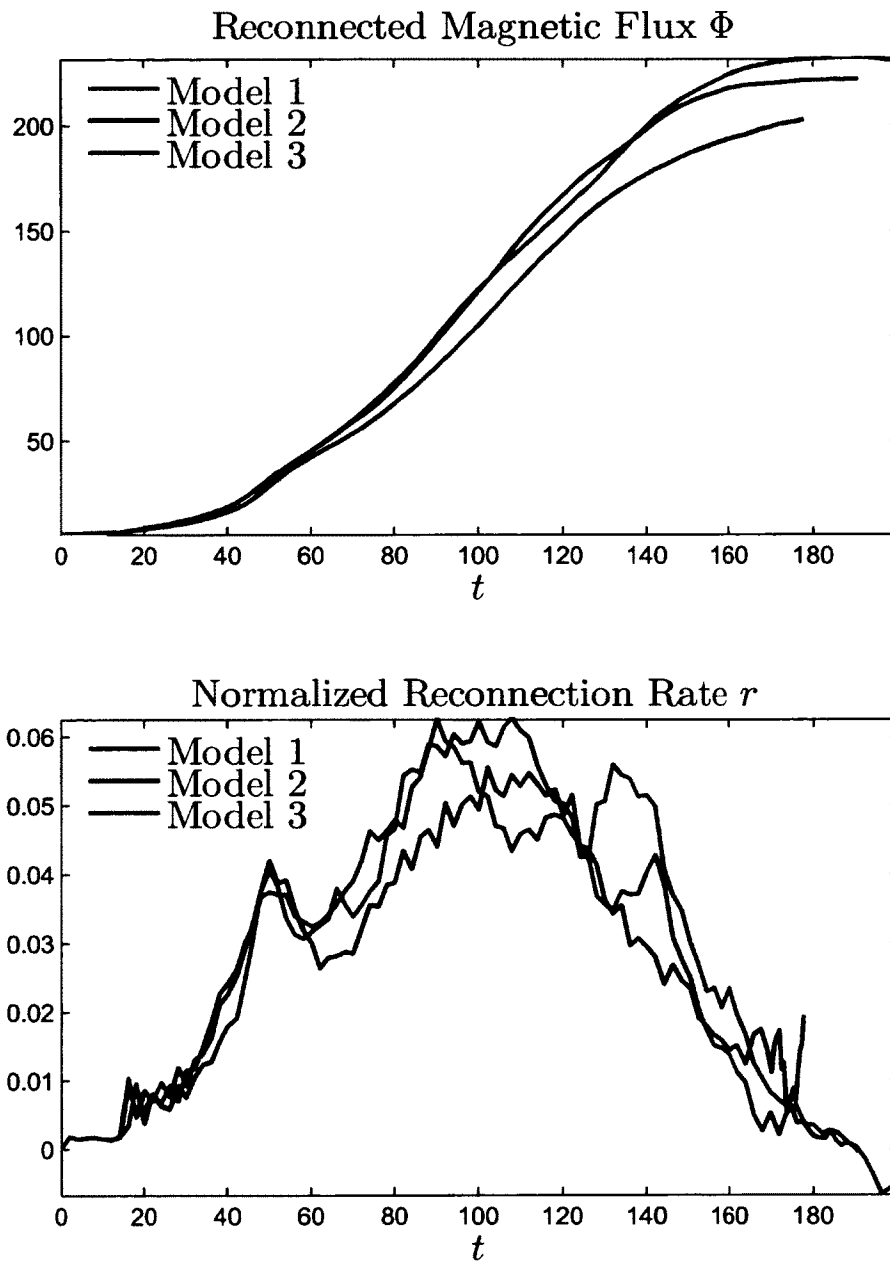
Figure 6.2: Reconnected magnetic flux Φ, and normalized reconnection rate r for the different resistivity models.

the initial diffusion region. The onset of reconnection for the initial conditions leads to the evolution of a thin current layer (diffusion region and attached outflow region) in a limited vicinity of the equatorial plane at $z = 0$ and with a finite extent $|y| \leq 10$ in the y direction. This thinning of the current sheet with the thinnest current sheet located at $z = 0$ is also a thinning of the shear flow layer, which changes the KH onset condition. As a result, the fastest growing KH waves are modes with short wavelength which are unstable only in the thin current sheet region and they are fully developed at $t = 48$. Initially there are six KH waves in the vicinity of the reconnection diffusion region, which corresponds to a KH wavelength of $l \approx 2$. These KH modes are the fastest growing waves, and their instability and growth are determined by the width of the thin shear flow layer [*Miura and Pritchett*, 1982]. Outside of the y range of the diffusion region $|y| > 10$, somewhat longer wavelength KH waves are the fastest growing modes. Their wavelength and growth are determined mostly by the original width of the shear flow layer, which has not been much effected by magnetic reconnection yet. However, the longer wavelength KH modes deform the current layer outside of initial diffusion region, with localized concentrations (thinning of current layer and thereby triggering the onset condition for magnetic reconnection). Thus, magnetic reconnection also starts to operate outside of the y range in which it has been originally triggered. Note, that the term diffusion region here is actually used in an average sense because the initial diffusion region is rapidly split into many small diffusion region parcels through the modulation of the current layer by the KH waves.

The evolution of KH waves from short to longer wavelength KH waves has also been observed by other numerical simulations (see summary in [*Miura*, 1995b]). This evolution is often considered as the coalescence instability. However, this is not likely the case in my simulation. Figure 6.3 illustrates that the longest wavelength KH mode already appears to be the dominant mode at $t = 90$, although shorter wavelength KH modes still exist. This indicates that the shorter wavelength KH modes are saturated and dissipated instead of undergoing coalescence. At $t = 144$, the longest wavelength mode is identical to the simulation box size in the y direction, which dissipates the
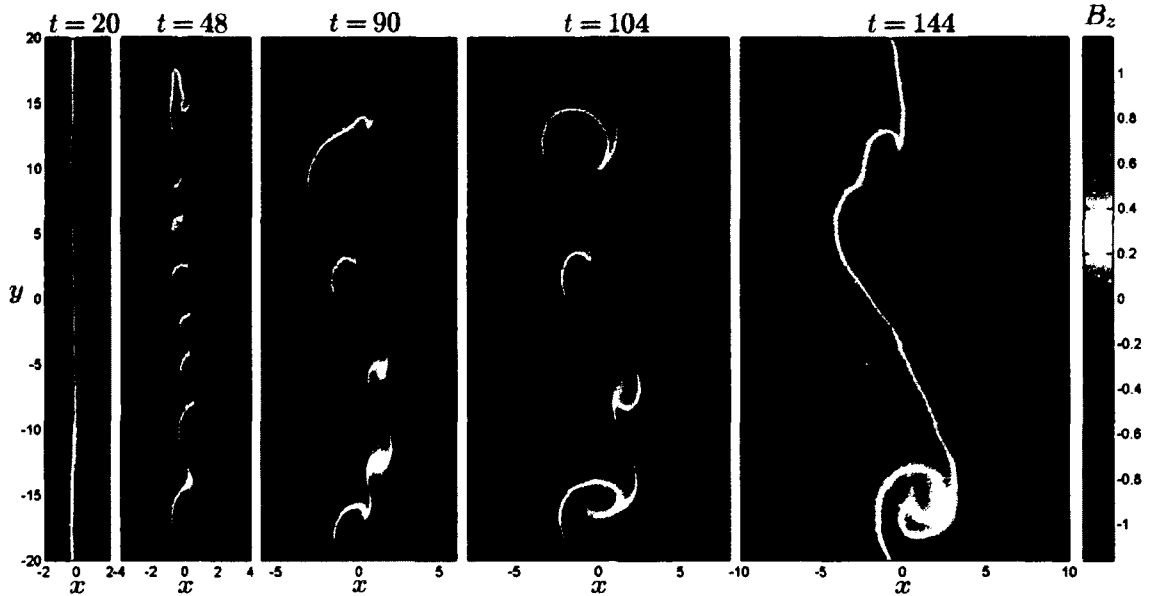
Figure 6.3: Magnetic field B_z component on the equatorial plane $z = 0$, when $t = 20$, 48, 90, 104, and 144 for the reference case. Black line is the contour line for $B_z = 0$.

current layer and thus suppresses magnetic reconnection.

Figure 6.4 shows magnetic field B_z component at $x = 0$, for $t = 20$, 48, 90, and 144 for the reference case, which illustrates the KH mode expansion along the z direction. At $t = 20$, the largest (but still linear) amplitude KH waves are observed close to the edge of the source region for reconnection. Multiple nonlinear KH waves with different wavelength appear at $t = 48$, showing and evolution to longer wavelength KH waves with increasing time, which is consistent with the previous analysis. The figure also demonstrates that these KH waves are localized from -20 to 20 along the z direction. Note, that the friction term is switched on at $|z| > 30$, thus friction is not likely to account for the localization. My interpretation is that the width of shear flow widens in the reconnection outflow region, and thereby switching off the KH modes (or only permitting very large wavelengths).

To illustrate the influence of KH mode on magnetic reconnection, I present the field-aligned electric potential difference $\Delta\phi$ for $t = 20$, 48, 90, 104, and 144 for the
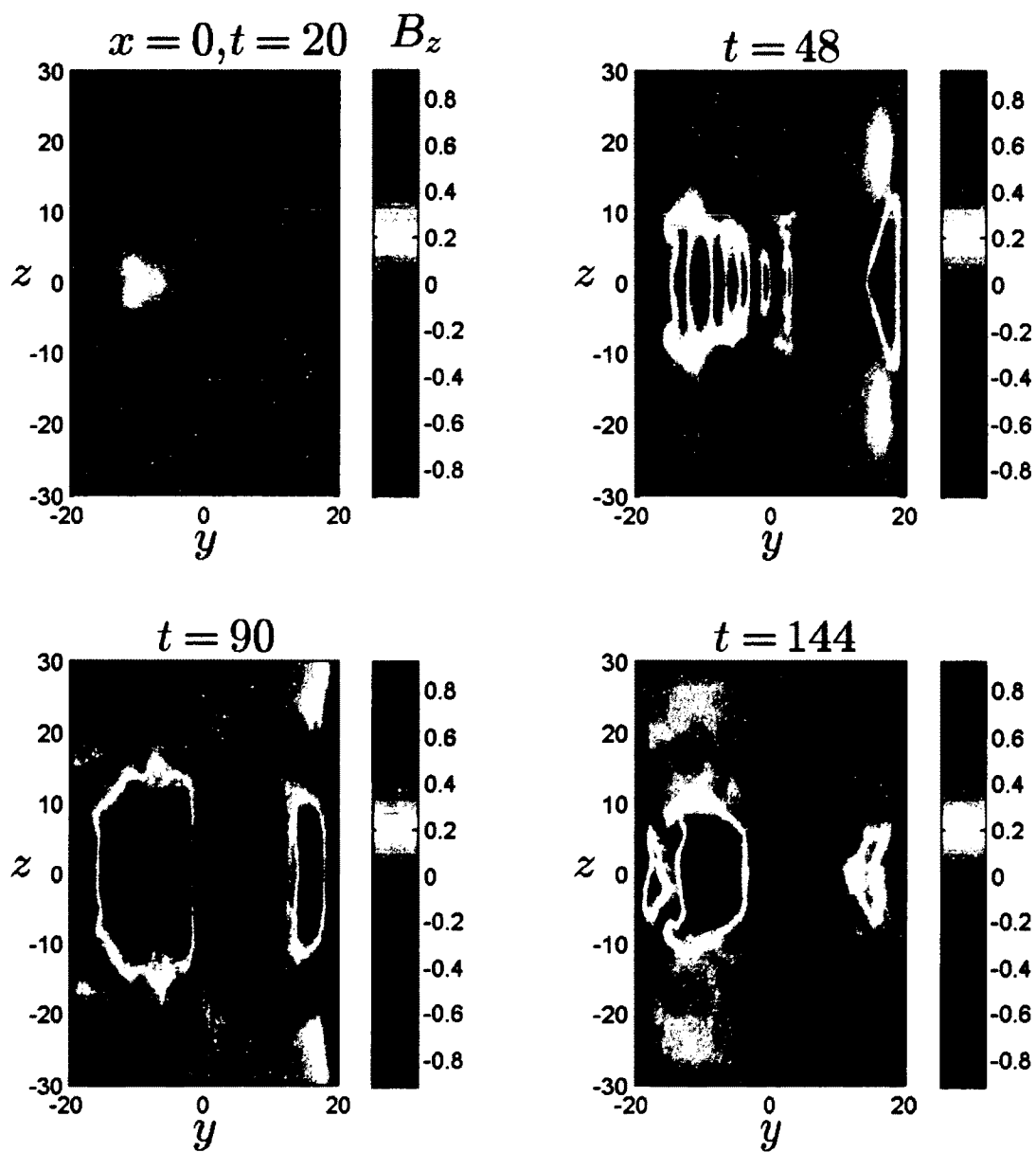
Figure 6.4: Magnetic field B_z component for $t = 20$, 48, 90, and 144 for the reference case in a cut at $x = 0$.

reference case in a cut at $z = 1$ close to the equatorial plane in Figure 6.5. The field-aligned electric potential difference is

$$\Delta\phi = \int E_{\|}ds, \tag{6.18}$$

where $E_{\|}$ is the parallel electric field component, and ds is an infinitesimal length along the magnetic field line [Hesse and Schindler, 1988]. Figure 5 shows the field aligned electric potential difference $\Delta\phi$ for open field lines at $z = 1$, where a nonzero value indicates that the field line at this location is going through the diffusion region, i.e., is undergoing magnetic reconnection. The range of the color-bar is limited to better represent the structure of the diffusion region. However, I also label the maximum (minimum) value at the top (bottom) of the color-bar as a reference. At $t = 20$, magnetic reconnection operates in the initial diffusion region and attached outflow regions with a small field-aligned electric potential difference $|\Delta\phi| < 0.05$. At $t = 48$, the diffusion region extends through the whole simulation box along the y direction, and its shape is strongly modified by the KH waves. At $t = 90$ and 104, the open flux region has the same shape of well-developed KH waves or vortices. The largest field-aligned electric potential difference $|\Delta\phi|$ appears along the spine of the KH waves instead of the vortex regions. Compared to $t = 104$, the largest field-aligned electric potential difference $|\Delta\phi|$ at $t = 144$ is much higher, which may indicates a field line passing the diffusion region several times due to the periodic boundary condition or numerical inaccuracy.

6.3.2 Influence of the Shear Flow Magnitude on Reconnection and KH Waves

The solar wind speed is a critical parameter for the evolution and of KH waves at the magnetospheric boundary. At 1 AU, the speed of the solar wind is usually around several hundred km/s. Depending on the location, the total velocity difference between solar wind plasma and the stagnant magnetospheric plasma varies from 0 at subsolar point to values close to the solar wind speed near the tailward flank boundary.
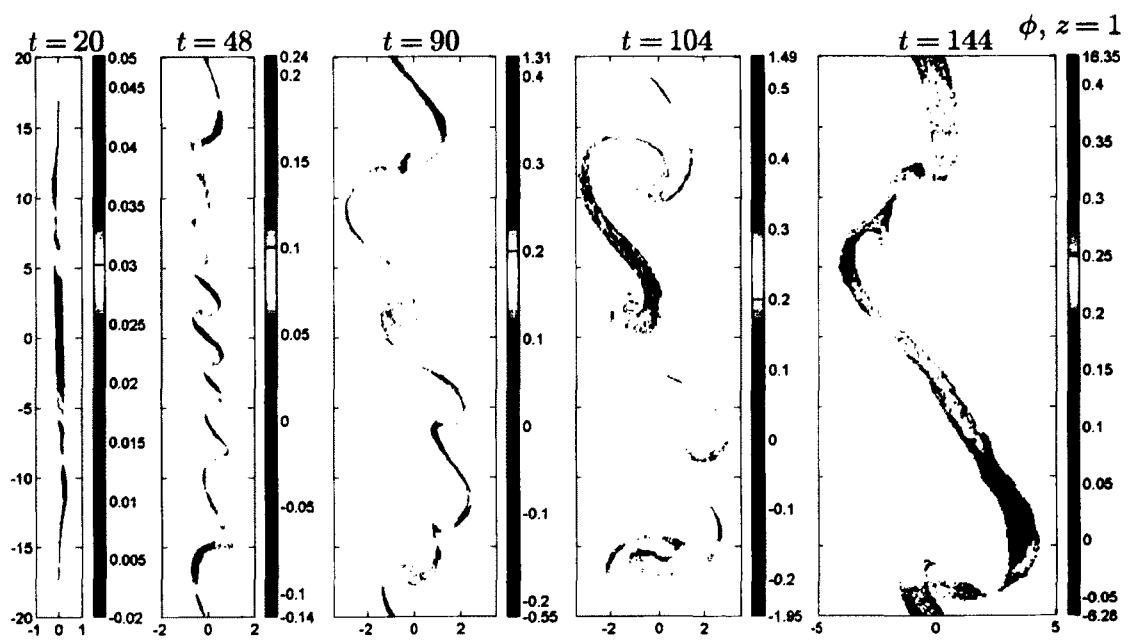
Figure 6.5: Field-aligned electric potential difference for $t = 20$, 48, 90, 104, and 144 for the reference case in a cut at $z = 1$ close to the equatorial plane.

Figure 6.6 shows the total reconnected magnetic flux Φ and normalized reconnection rate r for different initial shear flow magnitude V_{y0} varying from 0 to V_f. All other parameters are the same as for the reference case. For small shear flow $M_f \leq 0.3$, the reconnected magnetic flux Φ monotonously increases with time at a fairly constant normalized reconnection rate of 0.02 to 0.03, which indicates that a small shear flow has a minor influence on magnetic reconnection. The growth of KH modes increases with increasing shear flow magnitude. With the sufficiently large shear flow $M_f > 0.3$, well-developed KH modes significantly increase the normalized reconnection rate r. However, the total amount of reconnected magnetic flux Φ appears to be limited.

6.3.3 Influence of a Guide Field Component on Reconnection and KH Waves

At the dayside magnetopause, a guide field component is also present almost everywhere, which usually can be considered as an additional pressure in two-dimensional magnetic reconnection. However, this component is parallel to the **k** vector of the KH waves, which at larger values can stabilize the KH waves. Figure 6.7 shows the reconnected magnetic flux Φ, and normalized reconnection rate r for different initial guide field values B_{y0} varying from 0 to 0.5, where all other parameters are the same as for the reference case, and $B_{y0} = 0.54$ is the cut-off guide field for KH instability for the chosen shear flow with $M_f = 0.5$. The initial evolution of reconnected flux and normalized reconnection rate is similar for all cases. However, for $B_{y0} \leq 0.3$, the normalized reconnection rate r assumes a maximum of 0.06 around $t = 100$ and the reconnected flux Φ at about $t = 160$. In comparison, for larger $B_{y0} \geq 0.4$, magnetic reconnection assumes an intermediate maximum about $t = 60$ and starts to increase again around $t = 140$. A saturation is not apparent on the simulation time scale.

The frozen-in condition in combination with the shear flow in the y direction implies a drag of reconnected magnetic field line into opposite directions on the two sides of the outflow region, which generates a B_y component. This anti-symmetry of the B_y component is broken by the initial guide field component, which is basically
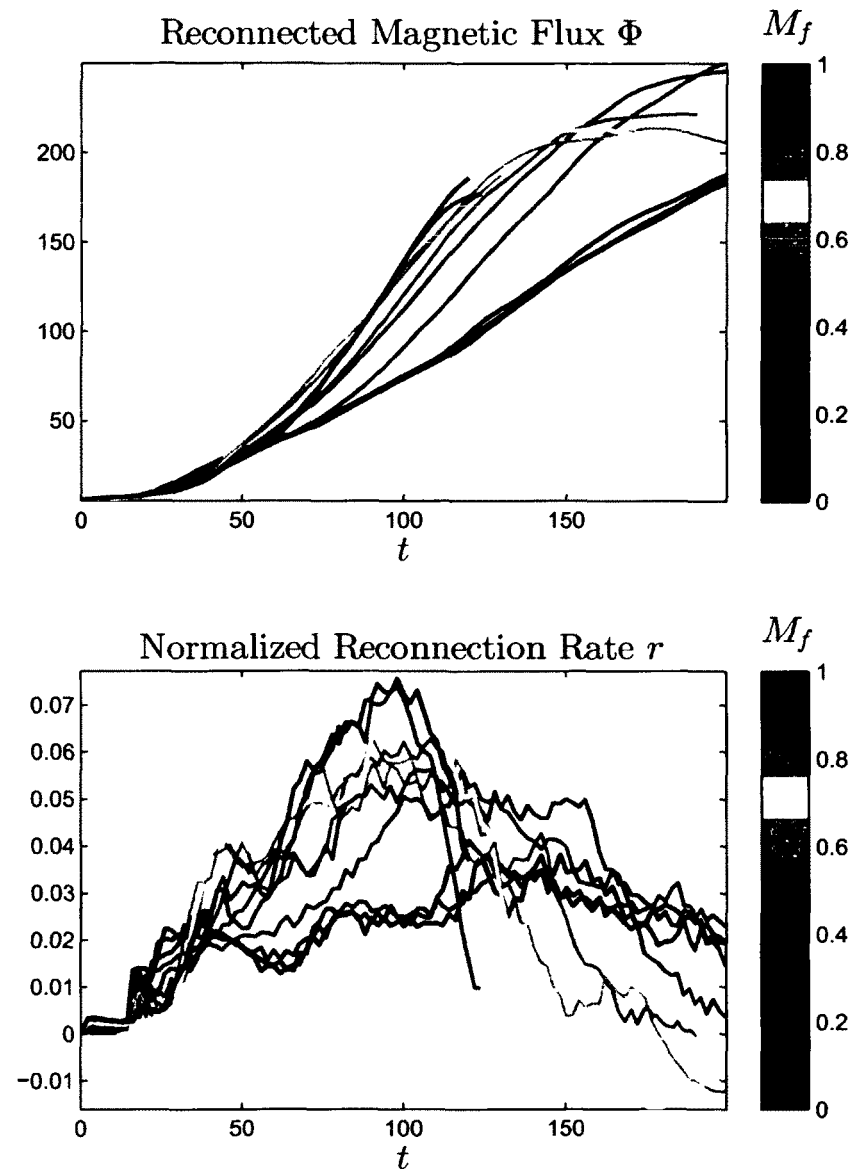
Figure 6.6: Reconnected magnetic flux Φ, and reconnection rate r for different initial speed of shear flow $M_f \in [0, 1]$.
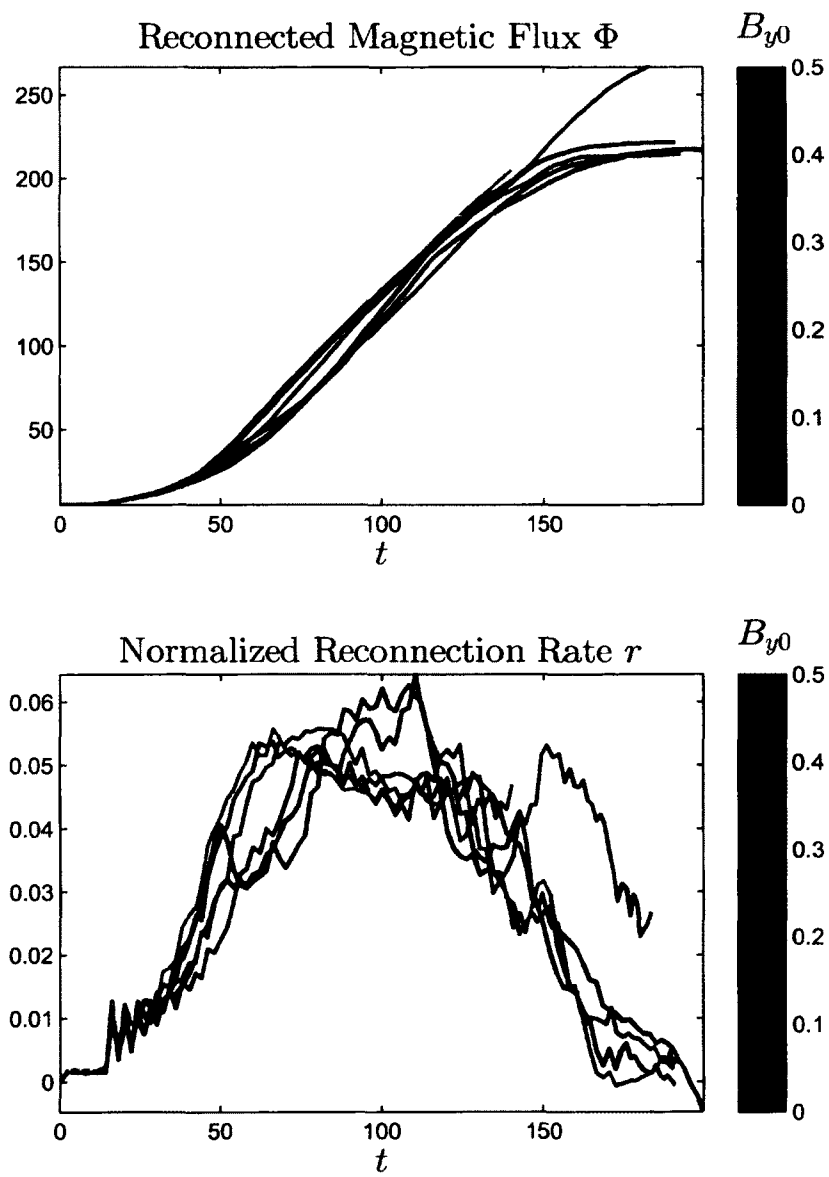
Figure 6.7: Reconnected magnetic flux Φ, and reconnection rate r for different guide field $B_{y0} \in [0, 0.5]$.

a two-dimensional effect and illustrated in Figure 6.8. The left panel shows the magnitude of the magnetic field B_y component in a cut at $y = 0$, at $t = 140$ for the $B_{y0} = 0.3$ case. In this configuration (which applies to the dawn side flank of the magnetosphere), the shear flow generates a positive B_y component in the northern hemisphere, and a negative B_y component in the southern hemisphere. Therefore, the initial positive guide field component increases the magnitude of B_y in the northern hemisphere, and decreases the magnitude of B_y in the southern hemisphere. Thus, the KH modes onset conditions are modified by this asymmetric magnetic field B_y component. The right panels in Figure 6.8 shows the magnetic field B_z component in the cut at $z = \pm 2.1$. It demonstrates that a long wavelength KH wave develops in the southern hemisphere, while KH modes are switched off in the northern hemisphere.

An interesting question is how this southern-northern hemispheric asymmetry affects ionospheric signatures? Figure 6.9 shows the field-aligned electric potential difference $\Delta\phi$ in cuts at top and bottom boundary, at $t = 140$ for the $B_{y0} = 0.3$ case. Although the total open flux is the same for both boundaries, the bottom boundary (the southern hemisphere) shows more vortex structures, which indicates that the guide field component in the IMF may lead to auroral spirals only in one hemisphere.

6.3.4   Influence of Hall Physics

The typical width of the magnetospheric boundary is about several ion inertia scales, and an onset condition for magnetic reconnection based on micro-turbulence requires a width of the current layer comparable or slightly smaller than the ion inertia scales. In this section, three selected cases are chosen to investigate effects caused by Hall physics. For computational reasons, a smaller simulation box ($L_y = 10$) is used in these three cases. The Hall term leads to the separation of the ion and electron velocity, and the frozen-in condition only applies to the electrons which carry most of the current in thin current sheets. Hall physics also generates faster two-dimensional magnetic reconnection [*Birn et al.*, 2001; *Otto*, 2001], and *Huba* [1994] demonstrated that the Hall term breaks the dawn-dusk symmetry. Therefore the first case with a
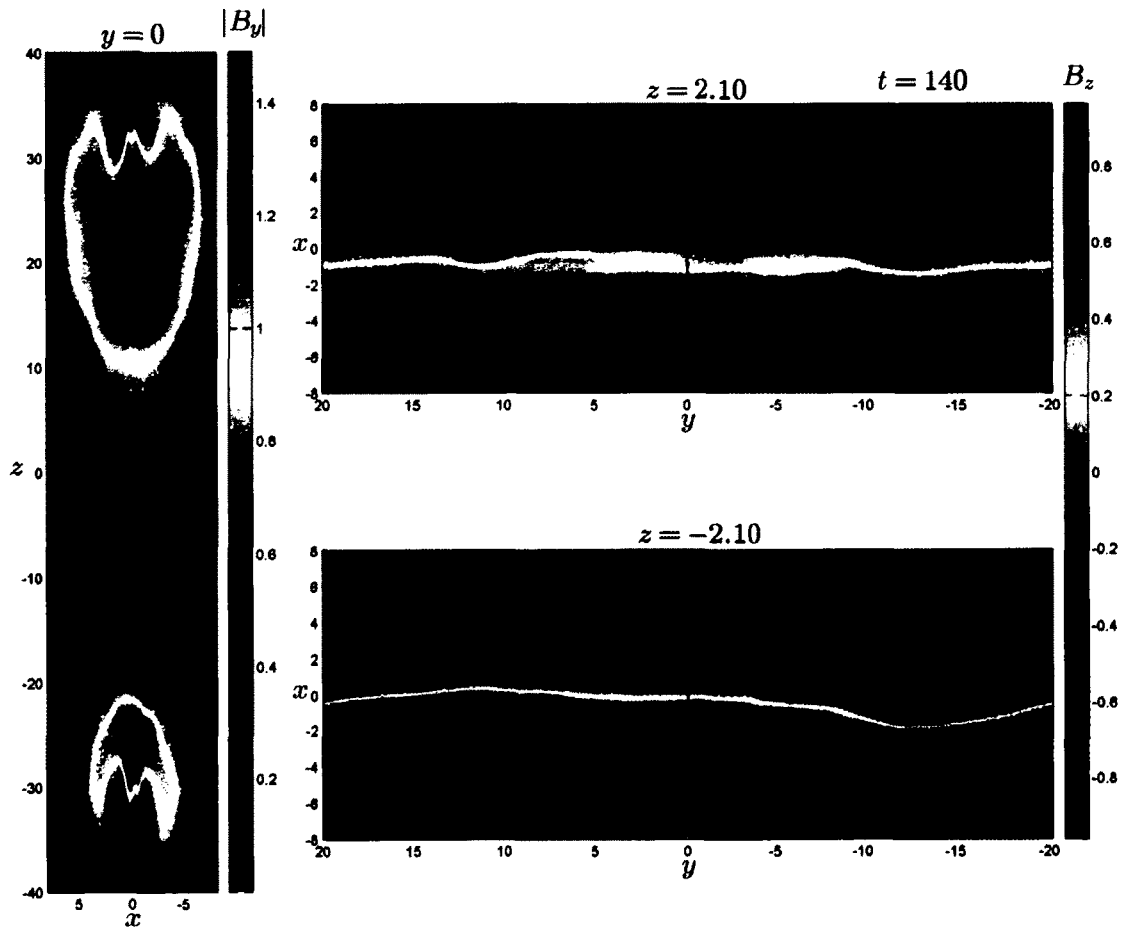
Figure 6.8: Magnitude of magnetic field B_y component (left panel) at the $y = 0$ plane, magnetic field B_z component (right panels) at $z = \pm 2.1$ plane, at $t = 140$ for $B_{y0} = 0.3$ case.
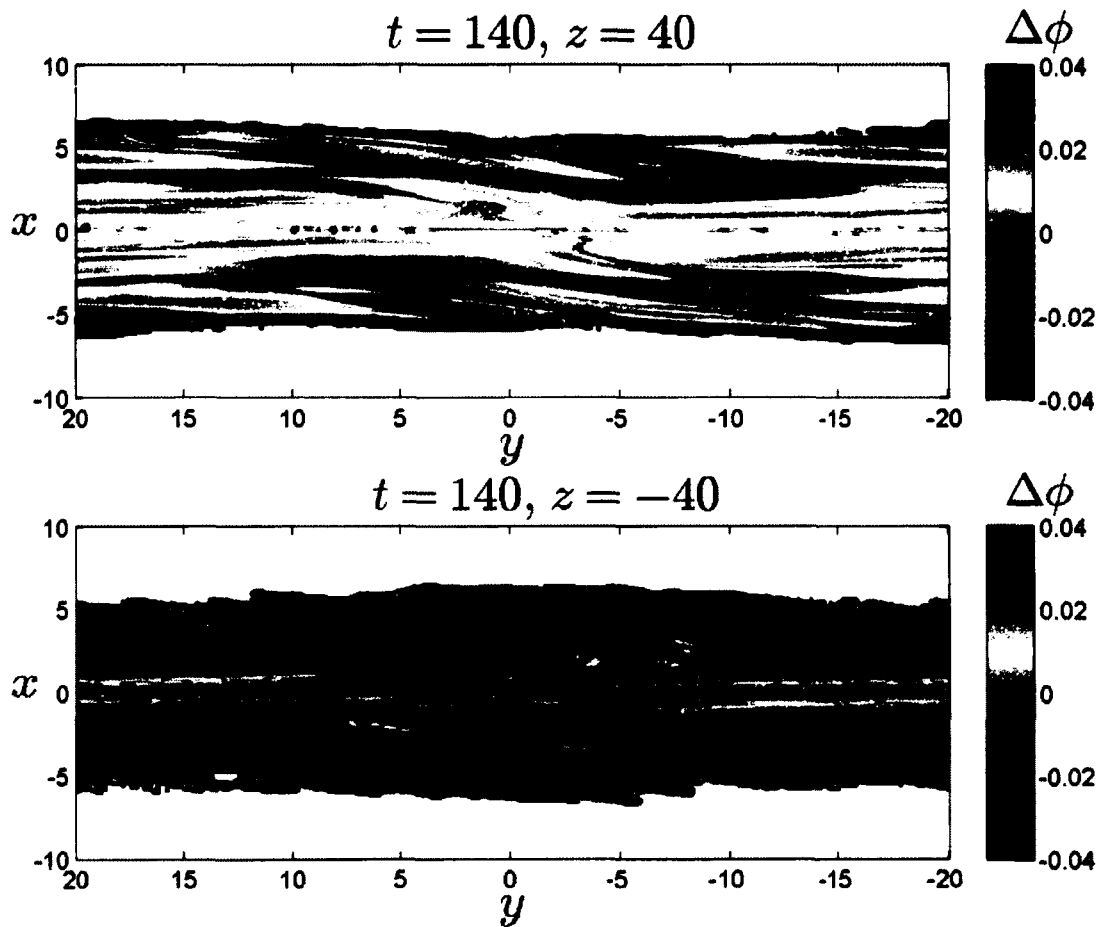
Figure 6.9: The field-aligned electric potential difference $\Delta\phi$ in a cut at top and bottom boundary, at $t = 140$ for $B_{y0} = 0.3$ case.

Hall parameter $l = 0.6$ represents the dawn side ($M_f = 0.5$), and the second case with $l = 0.6$ and $M_f = -0.5$ represents the dusk side. For comparison, the third case is the MHD case ($l = 0$, $M_f = 0.5$). All other parameters are the same as for the reference case. Figure 6.10 illustrates that Hall physics leads to a much higher normalized reconnection rate. This faster reconnection is likely caused by two main reasons. First, the electron dynamics in the diffusion region (whistler wave generation) cause a finite and much shorter length of this region. This implies a higher reconnection rate because this rate is determined by the width to length aspect ratio. This property is consistent with prior two-dimensional simulation results [*Birn et al.*, 2001; *Otto*, 2001]. Second, in the thin current sheet of the diffusion region the current is mainly along the y direction, and is carried mostly by electrons. Due to the electron frozen-in condition, much of the magnetic structure of the diffusion region is carried by the electron along the y direction against the current, such that the diffusion region expands fast with the electron motion. The second reason is important only when the width of current layer is thin, because this corresponds to large current density and fast electron motion. Figure 6.10 also indicates that the overall evolution does not show a significant dawn-dusk asymmetry, which contradicts somewhat *Huba*'s [1994] result, although *Huba* [1994] did only study the evolution of KH waves without an analysis of the reconnection rate. However, in the present simulation additional differences to *Huba*'s [1994] set up include a smaller Hall parameter, and a smaller density asymmetry.

6.4 Summary and Discussion

A realistic magnetospheric boundary for southward IMF conditions typically has large anti-parallel magnetic field components combined with a sufficient perpendicular shear flow. It is demonstrated that the perpendicular shear flow causes magnetic reconnection and KH modes to operate simultaneously. In this study, I assume that magnetic reconnection is the primary process. The results demonstrate that magnetic reconnection reduces the width of the shear flow and therefore switches on KH modes
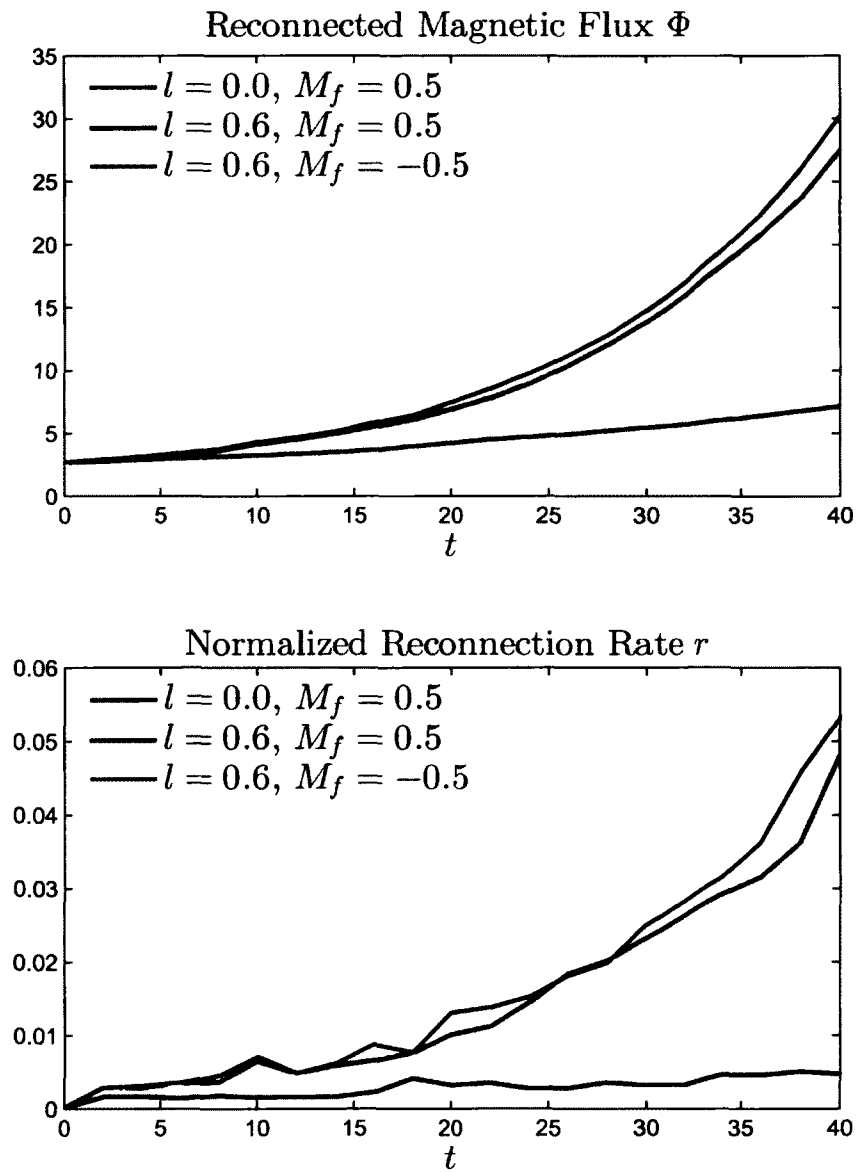
Figure 6.10: Reconnected magnetic flux Φ, and normalized reconnection rate r for Hall case.

initially with short wavelengths and large growth rate. Subsequently longer wavelengths waves develop during the evolution depending on the local width of the shear layer that is being modified by the reconnection process. This evolution of a range of different scale KH waves is consistent with *Hwang et al.*'s [2011] observational results. The evolution of KH waves from short to longer wavelength KH waves is caused by the lower growth rate and therefore slower evolution of longer wavelength modes. In this evolution shorter wavelength KH modes are saturated and dissipated instead of undergoing coalescence. These KH waves are localized along the z direction because reconnection causes a thin shear flow layer allowing short wavelength modes to grow. With increasing distance from the reconnection diffusion regions the width of shear flow widens in the outflow region, and thereby switching off KH growth (or only permitting large wavelengths).

The nonlinear KH waves deform the location and width of the current layer, which generates patchy reconnection and increases the normalized magnetic reconnection rate. The diffusion region extends through the whole simulation box along the y direction, and its shape is strongly modified by the KH waves. The fastest normalized reconnection rate r is proportional to the KH modes growth rate. Therefore, a larger initial shear flow value V_{y0} increases the normalized reconnection rate. This appears at first glance contradictory to the fact that the reconnection rate increases strongly only when KH waves approach a nonlinear amplitude. However, a faster growth rate implies that a nonlinear state is reached earlier, thereby explaining the relation between growth and reconnection rate. In this study, I have not examined a configuration with an initial shear flow value M_f larger than 1, which is KH stable for two-dimensional situations. However, KH modes may still operate at the boundary of the reconnection outflow region in three-dimensional configuration, which is an aspect of future work.

One of the most significant properties in the results is the limitation of the total amount of reconnected flux Φ by the longest possible KH waves. This is likely explained by the nonlinear saturation of KH waves at later times in their evolution,

which dissipates the current layer and thus turns off magnetic reconnection. For short wavelength modes this effect is reduced by the growth of longer waves during which current is again concentrated, however, once the longest possible wavelength waves undergo saturation, reconnection is strongly reduced. The longest unstable wavelengths are determined by the size of the unstable KH region along the z direction (i.e., some vicinity of the equatorial plane). Wavelengths larger than this size loose energy fast through Alfvén waves carrying energy efficiently away from the unstable region, thereby stabilizing long wavelength modes.

A sufficiently large guide field component B_{y0} also stabilizes the KH modes, and therefore magnetic reconnection operates at a slightly reduced and more constant normalized reconnection rate r. Interestingly, a relatively large guide field appears to remove the magnetic flux Φ limitation for reconnection. A possible reason for this is the partial stabilization which does not permit a nonlinear growth of the KH waves such the thin current layer is not anymore dissipated.

The frozen-in condition in combination with the shear flow in the y direction implies a drag of a reconnected magnetic field line into opposite directions on the two sides of the outflow region, thereby generating a B_y component of opposite sign in the northern and southern outflow regions. This anti-symmetry of the flow generated B_y component is broken by the initial guide field component, which is basically a two-dimensional effect. However, in three-dimensional configuration, this B_y component is parallel to the $\mathbf{k}$ vector of KH wave, which can stabilize the KH mode. Therefore, the asymmetric B_y component leads to different KH onset condition for southern-northern hemispheres, which may also change the auroral signatures of KH waves at the conjugate points.

In the presence of plasma flow, magnetic reconnection is also associated with the generation of field-aligned currents (FACs), which play a critical role in the coupling between the magnetosphere and ionosphere. Therefore, the coupling of KH modes and magnetic reconnection should also generate significant FAC. It is demonstrated that the FAC generated by a velocity shear is critical for the coupling of the KH waves
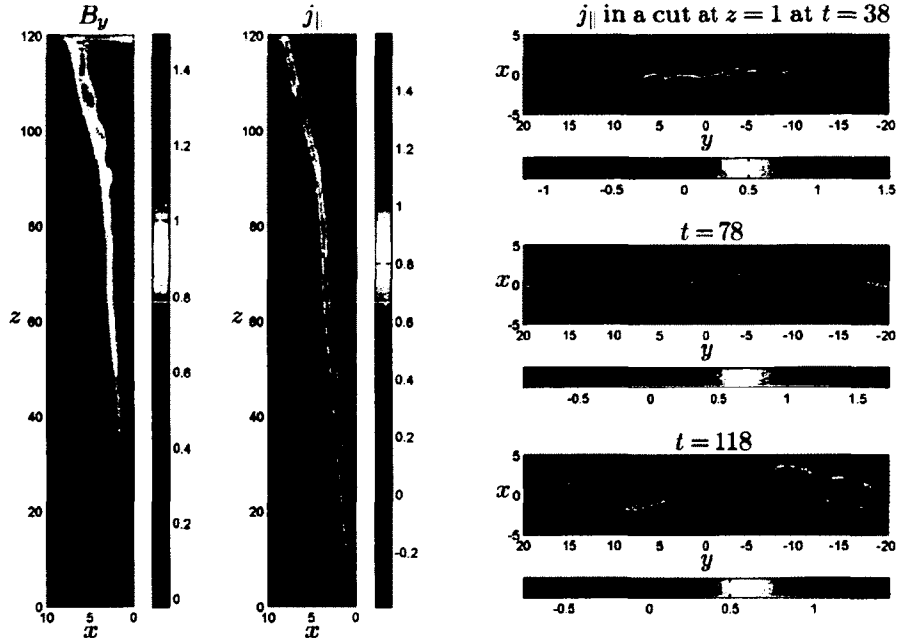
Figure 6.11: The left two panels show the magnetic field B_y component and FAC density $j_{||}$ from two-dimensional magnetic reconnection with a perpendicular shear flow. The right three panels present the FAC density $j_{||}$ in a cut at $z = 1$ at $t = 38$, 78, and 118 for the reference case.

and current sheet instabilities to the ionosphere [*Lysak and Song*, 1996]. The left two panels of Figure 6.11 present the magnetic field B_y component and FAC density $j_{||}$ in the xz plane from two-dimensional simulation ($y_0 = z_\nu = \infty$). It illustrates that the generation of B_y is directly associated with the FAC generation (see Chapter 4). In the three-dimensional configuration, this FAC structure is strongly modified by the KH waves, which is illustrated by the right three panels showing the FAC density $j_{||}$ in a cut at $z = 1$ at $t = 38$, 78, and 118 for the reference case.

The inclusion of Hall physics leads to the separation of the ion and electron velocity, and the frozen-in condition only applies to the electrons. The three-dimensional simulation results demonstrate that Hall physics leads to a faster normalized reconnection rate, which is consistent with similar two-dimensional results. This faster

reconnection rate has been attributed to the finite and much shorter length of the diffusion region caused by the electron dynamics in the diffusion region (whistler wave generation), which is a two-dimensional property. In addition there is a three-dimensional effect because much of the magnetic structure of the diffusion region is carried by the electron along the y direction against the current, due to the electron frozen-in condition. This leads to a fast expansion of the localized diffusion region into the third dimension and thus increases the total reconnection rate.

In this study I did not consider finite ion Larmor radius (FLR) effects and electron pressure gradient terms, which is comparable to the ion inertia scale. However, particularly FLR effects require ion kinetics and therefore hybrid-simulations. Another aspect of outstanding future work is the comparison between simulation and observation results, i.e., what are the typical observational signatures of KH modulated magnetic reconnection and do they agree with signatures typically associated with patchy magnetic reconnection such as magnetic flux transfer events.

Chapter 7
Summary and Discussion

It is widely believed that magnetic reconnection and Kelvin-Helmholtz (KH) instabilities play a crucial role for solar wind plasma access to the Earth's magnetosphere. Magnetic reconnection can change the magnetic topology and convert large amounts of magnetic energy into bulk kinetic and thermal energy. A typical property of the magnetospheric boundary is the presence of fast flow of the shocked solar wind plasma almost everywhere at the boundary. In the past, most of the plasma transport into the magnetosphere for southward IMF has been attributed entirely to magnetic reconnection. Only in the past decade or so has it been realized that KH modes can play a similarly important role for northward IMF by twisting the magnetic field and generating thin current sheets, thereby forcing magnetic reconnection to operate where the unperturbed boundary would not allow magnetic reconnection. Very few studies have considered the role of KH waves for southward IMF, and similarly few studies have considered the properties of magnetic reconnection in the presence of this fast flow even if KH waves are not present. This thesis focuses on two major unresolved problems of magnetic reconnection and, in the final chapters on the important and poorly understood question of the nonlinear interaction of KH waves and magnetic reconnection for large magnetic shear (southward IMF).

In recent years it has been realized that all of the magnetospheric plasma is strongly heated and rarefied compared to its origin, the shocked solar wind. Observations demonstrate that the plasma entropy is by 2 or 3 orders of magnitude higher in the magnetosphere than in the magnetosheath. This heating is not understood, and if reconnection is the dominant process for plasma entry, it is also a prime candidate for the strong nonadiabatic heating that must occur during the plasma entry. I have systematically examined this question for two-dimensional reconnection with MHD and Hall MHD studies in Chapter 3 and provide a summary and discussion of these result below in Section 7.1.

An important property of the magnetospheric boundary and the boundary pro-

cesses are their ionospheric signatures. The generation of such signatures is only possible if the boundary processes generate a current that is aligned with the magnetic field and connected into the ionosphere. A few studies have examined the generation of field-aligned current (FAC) by three-dimensional magnetic reconnection. However, the actual mechanisms for this generation appear more complicated than necessary. At least three basic mechanisms are proposed and examined in Chapter 4, operate already in two-dimensional reconnection, specifically the generation of FACs caused by the presence of a guide magnetic field, the presence of sheared plasma flow, and the inclusion of Hall physics into MHD. In fact, it is demonstrated that the basic physics responsible for the FAC generation is one-dimensional. A more concise discussion and summary is given in Section 7.2.

The actual interaction of reconnection and KH waves has been examined in Chapters 5 and 6. There the results on nonadiabatic heating and FAC generation provide important background information because the respective physics also operates in the reconnection-KH interaction in three dimensions. The results for this interaction are split into two chapters because the type of interaction depends on initial and boundary conditions which could select either the KH instability or magnetic reconnection as the primary process. The summary and discussion of these results is presented in Section 7.3.

7.1 Entropy and Magnetic Reconnection

Motivated by the observed strong nonadiabatic heating of magnetospheric plasma, it is demonstrated that such heating can be generated by magnetic reconnection only for the small inflow plasma beta conditions ($\beta \ll 1$) by using theoretical analysis and numerical simulation. In two-dimensional reconnection, nonadiabatic heating is mostly generated by slow shocks, which connect to the tiny diffusion region in Petschek's reconnection model. This diffusion region by itself is too small to affect plasma in a large volume of space. I also demonstrate that for the same inflow plasma beta values, simple Petschek reconnection can provide more nonadiabatic

heating than other configurations, i.e., in which a guide magnetic field component, a perpendicular shear flow, or an asymmetry of plasma density is present. In an ideal situation, I have generally shown that the entropy increase ratio of outflow to inflow regions has an upper limit of

$$\frac{S_o}{S_i} < 1 + \frac{1}{\beta}, \tag{7.1}$$

where my definition uses $S = p\rho^{-\gamma}$. At Earth's magnetosphere, the plasma entropy increases over 100 times when plasma enters the magnetosphere, which requires that the magnetosheath plasma beta is below 0.01. However, the typical magnetosheath plasma beta is about 0.1 to 1, which indicates that magnetic reconnection is not likely to provide enough nonadiabatic heating without the consideration of other plasma physical effects. Here I propose several possibilities which may resolve this issue in future work.

1. The entropy increase at magnetopause requires nonadiabatic heating in a large volume during the entry process. Any process which increases the size of the diffusion region to a large scale, would be more efficient to increase the plasma entropy in a larger volume. In fact, a simply way to realize such process may be a fast perpendicular shear flow that exceeds the fast mode speed. The physical interpretation is as following. It is illustrated in Chapter 4 that the outflow plasma satisfies the Walen relation

$$\Delta V = \pm \Delta V_A, \tag{7.2}$$

which implies that the super fast shear flow generates a large magnetic field (along the shear flow direction). This would surpass the magnetic field in the inflow region in a simplistic scaling such that the total pressure in the outflow region becomes larger than the inflow region. As a result, the diffusion region and the entire outflow region must expand to maintain the total pressure balance. However, this mechanism is applicable only when (1) the shear flow is not strongly modified by the KH mode, and (2) the width of diffusion region is on the ion inertia scale instead of the electron inertia scale. The first requirement

can be checked by using three-dimensional MHD simulation, and the second requirement needs comparison with the observational data.

2. The consideration of non-MHD micro-physics in the entry process is another possible way to increase nonadiabatic heating. It is demonstrated that the Hall physics does not change the Rankine-Hugoniot relations. Therefore, it is not likely to account for an additional entropy increase. In general, the omitted terms in the induction equation are on the ion or the electron inertia scale, which is too small to have any large volume effect. A possible candidate is the heat conduction term in the thermal pressure equation. Note, that Ohmic heating is the only nonadiabatic source in resistive MHD (the nonadiabatic heating in the shock can be equivalent to the Ohmic heating). However, the inclusion of heat conduction smoothes the temperature profile, which provides another possible irreversible process. Furthermore, heat conduction arises as the third moment of the integral of the Boltzmann equation, which is largest term among those neglected in the derivation of the MHD equations.

3. It may be, and there is some observational evidence to support this, that the typical magnetosheath plasma beta does not reflect the correct value should be used for the magnetic reconnection at the magnetopause. Observations indicate that the plasma beta close to the magnetospheric boundary is already reduced from its typical magnetosheath value in the so-called "plasma depletion region". This region forms as a result of the different transport of magnetic flux and plasma around a three-dimensional obstacle. Another possible cause for a reduction of the plasma beta is the strong modification of all plasma properties associated with nonlinear KH waves. If this reduction in the plasma beta (and density) is sufficient and systematic, reconnection may in fact be able to explain the nonadiabatic heating. This can be resolved by a further study of the KH-reconnection interaction and by comparison with observations close to the magnetospheric boundary.

The results on nonadiabatic heating apply very much to the three-dimensional interaction of KH waves and reconnection. However, my current results for this interaction do not demonstrate a significant nonadiabatic heating as discussed below.

7.2 FAC Generation Mechanism in Magnetic Reconnection

FACs are widely observed and they play an important role for magnetosphere-ionosphere coupling. Observational evidence also links magnetic reconnection signatures such as flux transfer events and bursty bulk flows to ionospheric signatures which requires the generation of FAC. However, the FAC generation mechanisms have only been examined by using three-dimensional configurations, while FAC can be efficiently generated in two- or even one-dimensional configurations. Therefore, this thesis provides a systematic study on generation of FAC by using one- and two-dimensional MHD and Hall MHD simulation. The main results are listed below.

Magnetic reconnection with a small guide field component leads to a strong generation of FAC, while a large guide field component leads largely to a redistribution of the initial FAC. The total amount of FAC associated with guide field reconnection is not sensitive to the magnetic guide field magnitude.

A perpendicular shear flow rotates the magnetic field in the outflow region, thereby generating FAC also in configurations where no FAC exists in the initial conditions. The reconnection layer for a perpendicular shear flow configuration is similar to the reconnection layer in the guide field case. Since there is no FAC in the initial state such currents are solely generated by the intermediate shock in the reconnection geometry. The total amount of FAC, $\int j_{\parallel}/B dx$, is very much independent of the initial shear flow for values equal to or larger than $0.2 V_A$. The amount of current into the ionosphere is generally larger for shear flow than for guide field configurations.

Hall MHD replaces the switch off shock by a standing whistler wave. The often-found bipolar B_z structure (also present for FAC), which extends all the way along the outflow region, is the primary part of this standing wave. The maximum $j_{\parallel}$ does not simply increase with the increasing Hall parameter, while the value of $\int j_{\parallel} dx$

increases with increasing Hall parameter. Based on a renormalization I demonstrated that the maximum of $j_\parallel$ should be inversely proportional to $l = \lambda_i/L_0$. This implies a decrease of this maximum with increasing l, which is well satisfied in my results for $\lambda_i > 0.4L_0$. Similarly the apparent increase of the integrals $\int j_\parallel dx$ and $\int jB^{-1}dx$ with increasing l is explained by a proper renormalization of the time scale. The increase of these integrals with time is caused by the contribution of the standing whistler waves and the expansion of the standing wave region in time. Both ions and electrons approximately satisfy the Walen relation, which demonstrates that the perturbation is close to Alfvénic.

I note that FAC can also be generated in other two-dimensional processes, e.g., KH mode, which is a topic of future work. A fundamental difficulty in understanding FAC generation is the lack of an evolutionary equation for FAC density. Associated with this question, one can ask whether we can derive a simple equation in the form of a continuity equation with source terms:

$$\frac{\partial j_\parallel}{\partial t} + \nabla \cdot \left(\mathbf{W} j_\parallel\right) = \text{FAC source}, \tag{7.3}$$

where $\mathbf{W}$ is the speed of FAC, which is not necessary be the bulk velocity or Alfvén velocity. In other words, is there any conservation law which is associated with the FAC.

I finally remark that the magnitude of the FAC generation is largest for Hall physics and for the inclusion of shear flow. In fact, both mechanisms are closely related because Hall physics introduces velocity shear for the electron fluid. The FAC obtained in the two-dimensional study surpasses the FAC generated by three-dimensional effects of localized magnetic reconnection significantly [*Ma and Lee*, 2001] and should be the dominant contribution to FAC generation also in three dimensions.

7.3 Interaction Between KH Instability and Magnetic Reconnection

A realistic three-dimensional configuration of Earth's magnetopause for southward IMF conditions includes large anti-parallel magnetic components with a fast perpendicular shear flow. In this thesis, I provide the first systematic study on the nonlinear

interaction between magnetic reconnection and KH modes in such configurations by using three-dimensional MHD and Hall MHD simulations. This interaction can depend on whether the KH instability or magnetic reconnection is the primary process. Therefore, the investigation of this interaction employs two different sets of initial conditions, one of which favors magnetic reconnection (Chapter 5) and the other KH waves (Chapter 6) as the primary process.

It is demonstrated that the nonlinear interaction plays a critical role for solar wind plasma access to the Earth's magnetosphere. Both magnetic reconnection and KH modes mutually change the other mode's onset conditions by changing the width of the transition layer, i.e., the current layer and the shear flow layer. Thus, the normalized magnetic reconnection rate is strongly increased by nonlinear KH waves, and the KH modes limit the total reconnected flux by dissipating the electric current when the largest wavelength mode becomes highly nonlinear. This is particularly remarkable because this interaction leads to fast reconnection with local rates that are at least equal to the Petschek rate of fast reconnection without invoking Hall physics.

A larger initial shear flow value increases the KH mode growth, thereby increasing the normalized magnetic reconnection rate. However, a large initial shear flow, which is close to the fast mode speed, will stabilize KH modes. A guide magnetic field along the shear flow direction can also partially stabilize KH modes by decreasing the KH growth rate and reducing the size of the KH vortex, and thereby decreasing the normalized magnetic reconnection rate. A sufficiently large guide field clearly switches off KH modes. Thus, magnetic reconnection operates at a constant lower reconnection rate, but the total reconnected magnetic flux is not limited. The presented results illustrate that the evolution of shorter to longer wavelength KH waves is caused by a diffusive decay of shorter wavelength modes and by the slower growth of longer wavelength modes which become dominant at later times. This is different from the frequently invoked mechanism of coalescence, which involves merging two smaller wavelength modes into one with twice the wavelength. I also demonstrated that the

diffusion region and the distribution of FACs are strongly modified by KH waves. The inclusion of Hall physics leads to somewhat faster normalized reconnection rates.

The above conclusions are independent on whether KH modes or magnetic reconnection is the primary process. In the real world the primary mode depends on the growth of these two processes and the respective initial perturbations. In this study, the condition in which KH modes are the primary process allows to examine a single KH mode interaction with magnetic reconnection. Due to the finite width of the shear flow layer, compressibility, and the three-dimensional localization, the KH growth rate in the simulation is slower than it is for a two-dimensional infinitely thin, and incompressible boundary. For magnetic reconnection as the primary process condition, my results show varying wavelengths and growth of KH modes and are consistent with the observational results. It is also demonstrated that the presence of a guide magnetic field breaks the hemispheric symmetry, which is expected to have an influence on the ionosphere signatures.

This study did not consider finite ion Larmor radius effect nor electron pressure gradient term, which is comparable to the ion inertia scale. Finite ion Larmor radius effects require a kinetic treatment of the ion dynamics by using hybrid-simulations. Another aspect for outstanding future work is the comparison between simulation and observation results, i.e., what are the typical observational signatures of KH modulated magnetic reconnection and do they agree with signatures typically associated with patchy magnetic reconnection, such as magnetic flux transfer events.

In the interaction between KH waves and reconnection I have not observed significant nonadiabatic heating. This is expected because the simulations use a plasma beta of order unity. A systematic study of this heating is left for a future investigation because it would require a proper consideration of the asymmetry and plasma properties on the two sides of the boundary and is outside of the scope of this initial study of basic properties of the interaction of KH waves and magnetic reconnection.

Overall, my results provide new insight into important properties of the plasma transport from the solar wind into the magnetosphere. Specifically, important new

results are obtained on the topics of nonadiabatic heating during the plasma entry, the generation of FAC by magnetic reconnection, and on the nonlinear interaction of KH waves and magnetic reconnection for large magnetic shear.

Bibliography

Adamson, E., A. Otto, and K. Nykyri (2012), 3-D mesoscale MHD simulations of magnetospheric cusp-like configurations: cusp diamagnetic cavities and boundary structure, *Annales Geophysicae*, *30*, 325–341, doi:10.5194/angeo-30-325-2012.

Axford, W. I. (1964), Viscous interaction between the solar wind and the earth's magnetosphere, *Planetary and Space Science*, *12*, 45.

Birk, G. T., H. Wiechen, and A. Otto (1999), Magnetic Field Amplification in M82 Winds Caused by Kelvin-Helmholtz Modes, *The Astrophysical Journal*, *518*, 177–182, doi:10.1086/307273.

Birn, J., and M. Hesse (1996), Details of current disruption and diversion in simulations of magnetotail dynamics, *Journal of Geophysical Research*, *101*, 15,345–15,358, doi:10.1029/96JA00887.

Birn, J., and E. Priest (2007), *Reconnection of Magnetic Fields: Magnetohydrodynamics and Collisionless Theory and Observations*, ESA SP- 285 Vol. 2, Cambridge University Press.

Birn, J., et al. (2001), Geospace Environmental Modeling (GEM) magnetic reconnection challenge, *Journal of Geophysical Research*, *106*, 3715–3720, doi:10.1029/1999JA900449.

Birn, J., J. Raeder, Y. L. Wang, R. A. Wolf, and M. Hesse (2004), On the propagation of bubbles in the geomagnetic tail, *Annales Geophysicae*, *22*(5), 1773–1786, doi:10.5194/angeo-22-1773-2004.

Birn, J., M. Hesse, and K. Schindler (2006), Entropy conservation in simulations of magnetic reconnection, *Physics of Plasmas*, *13*(9), 092,117, doi:10.1063/1.2349440.

Birn, J., M. Hesse, K. Schindler, and S. Zaharia (2009), Role of entropy in magnetotail dynamics, *Journal of Geophysical Research (Space Physics)*, *114*, A00D03, doi:10.1029/2008JA014015.

Borovsky, J. E., and T. E. Cayton (2011), Entropy mapping of the outer electron radiation belt between the magnetotail and geosynchronous orbit, *Journal of Geophysical Research (Space Physics)*, *116*, A06216, doi:10.1029/2011JA016470.

Burgess, D., E. Möbius, and M. Scholer (2012), Ion Acceleration at the Earth's Bow Shock, *Space Science Reviews*, p. 50, doi:10.1007/s11214-012-9901-5.

Chandrasekhar, S. (1961), *Hydrodynamic and Hydromagnetic Stability*, The International Series of Monographs on Physics, Dover Publ.

Chen, Q. (1997), Two- and Three-Dimensional Study of the Kelvin-Helmholtz Instability, Magnetic Reconnection and Their Mutual Interaction at the Magnetospheric Boundary, Ph.D. thesis, UNIVERSITY OF ALASKA FAIRBANKS.

Chen, Q., A. Otto, and L. C. Lee (1997), Tearing instability, Kelvin-Helmholtz instability, and magnetic reconnection, *Journal of Geophysical Research*, *102*, 151–162, doi:10.1029/96JA03144.

Courant, R., K. Friedrichs, and H. Lewy (1967), On the Partial Difference Equations of Mathematical Physics, *IBM Journal of Research and Development*, *11*, 215–234, doi:10.1147/rd.112.0215.

Cowley, S. W. H., and M. Lockwood (1992), Excitation and decay of solar wind-driven flows in the magnetosphere-ionosphere system, *Annales Geophysicae*, *10*, 103–115.

Dungey, J. W. (1961), Interplanetary Magnetic Field and the Auroral Zones, *Physical Review Letters*, *6*, 47–48, doi:10.1103/PhysRevLett.6.47.

Fairfield, D. H., A. Otto, T. Mukai, S. Kokubun, R. P. Lepping, J. T. Steinberg, A. J. Lazarus, and T. Yamamoto (2000), Geotail observations of the Kelvin-Helmholtz instability at the equatorial magnetotail boundary for parallel northward fields, *Journal of Geophysical Research*, *105*, 21,159–21,174, doi:10.1029/1999JA000316.

Foullon, C., E. Verwichte, V. M. Nakariakov, K. Nykyri, and C. J. Farrugia (2011), Magnetic Kelvin-Helmholtz Instability at the Sun, *729*, L8, doi:10.1088/2041-8205/729/1/L8.

Fujimoto, M., T. Terasawa, and T. Mukai (1997), The Cold-Dense Plasma Sheet: A GEOTAIL Perspective, *Space Science Reviews*, *80*, 325–339, doi:10.1023/A:1004934306623.

Giovanelli, R. G. (1946), A Theory of Chromospheric Flares, *Nature*, *158*, 81–82, doi:10.1038/158081a0.

Giovanelli, R. G. (1947), Magnetic and Electric Phenomena in the Sun's Atmosphere associated with Sunspots, *Monthly Notices of the Royal Astronomical Society*, *107*, 338.

Hasegawa, H., M. Fujimoto, T.-D. Phan, H. Rème, A. Balogh, M. W. Dunlop, C. Hashimoto, and R. TanDokoro (2004), Transport of solar wind into Earth's magnetosphere through rolled-up Kelvin-Helmholtz vortices, *Nature*, *430*, 755–758, doi:10.1038/nature02799.

Hesse, M., and K. Schindler (1988), A theoretical foundation of general magnetic reconnection, *Journal of Geophysical Research*, *93*, 5559–5567, doi:10.1029/JA093iA06p05559.

Huba, J., U. S. O. of Naval Research, and N. R. L. (U.S.) (2006), *NRL Plasma Formulary*, NRL publication, Naval Research Laboratory.

Huba, J. D. (1994), Hall dynamics of the Kelvin-Helmholtz instability, *Physical Review Letters*, *72*, 2033.

Hwang, K.-J., M. M. Kuznetsova, F. Sahraoui, M. L. Goldstein, E. Lee, and G. K. Parks (2011), Kelvin-Helmholtz waves under southward interplanetary magnetic field, *Journal of Geophysical Research*, *116*, A08210, doi:10.1029/2011JA016596.

Kallenrode, M. (2004), *Space Physics: An Introduction to Plasmas and Particles in the Heliosphere and Magnetospheres*, Advanced Texts in Physics, Springer.

Kivelson, M. G., and C. T. Russell (1995), *Introduction to Space Physics*.

Krall, N. A., A. W. Trivelpiece, and K. R. Symon (1974), Principles of Plasma Physics, *IEEE Transactions on Plasma Science*, *2*, 196–196, doi:10.1109/TPS.1974.4316834.

La Belle-Hamer, A. L., A. Otto, and L. C. Lee (1995), Magnetic reconnection in the presence of sheared flow and density asymmetry: Applications to the Earth's magnetopause, *Journal of Geophysical Research*, *100*, 11,875, doi:10.1029/94JA00969.

Le, G., J. A. Slavin, and R. J. Strangeway (2010), Space Technology 5 observations of the imbalance of regions 1 and 2 field-aligned currents and its implication to the cross-polar cap Pedersen currents, *Journal of Geophysical Research*, *115*, A07202, doi:10.1029/2009JA014979.

Lee, L.-C. (1986), Magnetic flux transfer at the earth's magnetopause, in *Solar Wind Magnetosphere Coupling, Astrophysics and Space Science Library*, vol. 126, edited by Y. Kamide and J. A. Slavin, pp. 297–314.

Lifshitz, E., and L. Pitaevskii (1981), *Physical kinetics*, Course of theoretical physics, Butterworth-Heinemann.

Lin, Y., and L. C. Lee (1993), Structure of Reconnection Layers in the Magnetosphere, *Space Science Reviews*, *65*, 59–179, doi:10.1007/BF00749762.

Lin, Y., and L. C. Lee (1999), Reconnection layers in two-dimensional magnetohydrodynamics and comparison with the one-dimensional Riemann problem, *Physics of Plasmas*, *6*, 3131–3146, doi:10.1063/1.873553.

Lysak, R. L., and Y. Song (1996), Coupling of Kelvin-Helmholtz and current sheet instabilities to the ionosphere: A dynamic theory of auroral spirals, *Journal of Geophysical Research*, *101*, 15,411–15,422, doi:10.1029/96JA00521.

Ma, Z. W., and A. Bhattacharjee (2001), Hall magnetohydrodynamic reconnection: The Geospace Environment Modeling challenge, *Journal of Geophysical Research*, *106*, 3773–3782, doi:10.1029/1999JA001004.

Ma, Z. W., and L. C. Lee (1999), A simulation study of generation of field-aligned currents and Alfvén waves by three-dimensional magnetic reconnection, *Journal of Geophysical Research*, *104*, 10,177–10,190, doi:10.1029/1999JA900083.

Ma, Z. W., and L. C. Lee (2001), Hall effects on the generation of field-aligned currents in three-dimensional magnetic reconnection, *Journal of Geophysical Research*, *106*, 25,951–25,960, doi:10.1029/2000JA000290.

Ma, Z. W., L. C. Lee, and A. Otto (1995), Generation of field-aligned currents and Alfvén waves by 3D magnetic reconnection, *Geophysical Research Letters*, *22*, 1737–1740, doi:10.1029/95GL01430.

Marchaudon, A., J.-C. Cerisier, R. A. Greenwald, and G. J. Sofko (2004), Electrodynamics of a flux transfer event: Experimental test of the Southwood model, *Geophysical Research Letters*, *31*, L09809, doi:10.1029/2004GL019922.

Marchaudon, A., J.-C. Cerisier, M. W. Dunlop, F. Pitout, J.-M. Bosqued, and A. N. Fazakerley (2009), Shape, size, velocity and field-aligned currents of dayside plasma injections: a multi-altitude study, *Annales Geophysicae*, *27*, 1251–1266, doi:10.5194/angeo-27-1251-2009.

Miura, A. (1982), Nonlinear evolution of the magnetohydrodynamic Kelvin-Helmholtz instability, *Physical Review Letters*, *49*, 779.

Miura, A. (1984), Anomalous transport by magnetohydrodynamic Kelvin-Helmholtz instabilities in the solar wind-magnetosphere interaction, *Journal of Geophysical Research*, *89*, 801–818, doi:10.1029/JA089iA02p00801.

Miura, A. (1987), Simulation of the Kelvin-Helmholtz instability at the magnetospheric boundary, *Journal of Geophysical Research*, *92*, 3195.

Miura, A. (1992), Kelvin-Helmholtz instability at the magnetospheric boundary - Dependence on the magnetosheath sonic Mach number, *Journal of Geophysical Research*, *97*, 10,655, doi:10.1029/92JA00791.

Miura, A. (1995a), Dependence of the magnetopause Kelvin-Helmholtz instability on the orientation of the magnetosheath magnetic field, *Geophysical Research Letters*, *22*, 2993–2996, doi:10.1029/95GL02793.

Miura, A. (1995b), Kelvin-Helmholtz Instability at the Magnetopause: Computer Simulations, in *Washington DC American Geophysical Union Geophysical Monograph Series*, *Washington DC American Geophysical Union Geophysical Monograph Series*, vol. 90, edited by P. Song, B. U. O. Sonnerup, and M. F. Thomsen, p. 285.

Miura, A. (1996), Stabilization of the kelvin-helmholtz instability by the transverse magnetic field in the magnetosphere-ionosphere coupling system, *Geophysical Research Letters*, *23*, 761.

Miura, A., and P. L. Pritchett (1982), Nonlocal stability analysis of the MHD Kelvin-Helmholtz instability in a compressible plasma, *Journal of Geophysical Research*, *87*, 7431–7444, doi:10.1029/JA087iA09p07431.

Nakamura, T. K. M., and M. Fujimoto (2008), Magnetic effects on the coalescence of kelvin-helmholtz vortices, *Physical Review Letters*, *101*, 165,002, doi:10.1103/PhysRevLett.101.165002.

Nakamura, T. K. M., M. Fujimoto, and A. Otto (2006), Magnetic reconnection induced by weak Kelvin-Helmholtz instability and the formation of the low-latitude boundary layer, *Geophysical Research Letters*, *33*, 14,106–+, doi:10.1029/2006GL026318.

Nakamura, T. K. M., M. Fujimoto, and A. Otto (2008), Structure of an MHD-scale Kelvin-Helmholtz vortex: Two-dimensional two-fluid simulations including finite

electron inertial effects, *Journal of Geophysical Research*, *113*, A09204, doi:10.1029/2007JA012803.

Nykyri, K., and A. Otto (2001), Plasma transport at the magnetospheric boundary due to reconnection in Kelvin-Helmholtz vortices, *Geophysical Research Letters*, *28*, 3565–3568, doi:10.1029/2001GL013239.

Nykyri, K., and A. Otto (2004), Influence of the Hall term on KH instability and reconnection inside KH vortices, *Annales Geophysicae*, *22*, 935–949, doi:10.5194/angeo-22-935-2004.

Otto, A. (1990), 3D resistive MHD computations of magnetospheric physics, *Computer Physics Communications*, *59*, 185–195, doi:10.1016/0010-4655(90)90168-Z.

Otto, A. (1999), Three-Dimensional Magnetic Reconnection in Astrophysical Plasmas - MHD Approach, *Astrophysics and Space Science*, *264*, 17–24.

Otto, A. (2001), Geospace Environment Modeling (GEM) magnetic reconnection challenge: MHD and Hall MHD-constant and current dependent resistivity models, *Journal of Geophysical Research*, *106*, 3751–3758, doi:10.1029/1999JA001005.

Otto, A. (2008), Three-Dimensional Simulation of Kelvin-Helmholtz Modes at the Magnetospheric Boundary, *AGU Spring Meeting Abstracts*, p. A2.

Otto, A. (2010), Magnetospheric physics lecture notes, http://how.gi.alaska.edu/ao/.

Otto, A. (2012), Adavanced plasma physics lecture notes, http://how.gi.alaska.edu/ao/adv_plasma/.

Otto, A., and D. H. Fairfield (2000), Kelvin-Helmholtz instability at the magnetotail boundary: MHD simulation and comparison with Geotail observations, *Journal of Geophysical Research*, *105*, 21,175–21,190, doi:10.1029/1999JA000312.

Otto, A., J. Büchner, and B. Nikutowski (2007), Force-free magnetic field extrapolation for MHD boundary conditions in simulations of the solar atmosphere, *468*, 313–321, doi:10.1051/0004-6361:20054495.

Parker, E. N. (1957), Sweet's Mechanism for Merging Magnetic Fields in Conducting Fluids, *Journal of Geophysical Research*, *62*, 509–520, doi:10.1029/JZ062i004p00509.

Parker, E. N. (1958), Dynamics of the Interplanetary Gas and Magnetic Fields., *Astrophysical Journal*, *128*, 664, doi:10.1086/146579.

Petschek, H. E. (1964), Magnetic Field Annihilation, *NASA Special Publication*, *50*, 425.

Pu, Z.-Y., and M. G. Kivelson (1983), Kelvin-helmholtz instability at the magnetopause. i - solution for compressible plasmas. ii - energy flux into the magnetosphere, *Journal of Geophysical Research*, *88*, 841–861.

Russell, C. T., and R. C. Elphic (1978), Initial ISEE magnetometer results - Magnetopause observations, *Space Science Reviews*, *22*, 681–715, doi:10.1007/BF00212619.

Saunders, M. A., C. T. Russell, and N. Sckopke (1984), Flux transfer events - Scale size and interior structure, *Geophysical Research Letters*, *11*, 131–134, doi:10.1029/GL011i002p00131.

Scholer, M., and R. A. Treumann (1997), The Low-Latitude Boundary Layer at the Flanks of the Magnetopause, *Space Science Reviews*, *80*, 341–367, doi:10.1023/A:1004986323461.

Sibeck, D. G., et al. (1999), Chapter 5-Plasma Transfer Processes at the Magnetopause, *Space Science Reviews*, *88*, 207–283, doi:10.1023/A:1005255801425.

Southwood, D. J. (1987), The ionospheric signature of flux transfer events, *Journal of Geophysical Research*, *92*, 3207–3213, doi:10.1029/JA092iA04p03207.

Sun, X., Y. Lin, and X. Wang (2005), Structure of reconnection layer with a shear flow perpendicular to the antiparallel magnetic field component, *Physics of Plasmas*, *12*(1), 012,305, doi:10.1063/1.1826096.

Sweet, P. A. (1958), The Neutral Point Theory of Solar Flares, in *Electromagnetic Phenomena in Cosmical Physics, IAU Symposium*, vol. 6, edited by B. Lehnert, p. 123.

Takagi, K., C. Hashimoto, H. Hasegawa, M. Fujimoto, and R. TanDokoro (2006), Kelvin-Helmholtz instability in a magnetotail flank-like geometry: Three-dimensional MHD simulations, *Journal of Geophysical Research*, *111*, A08202, doi: 10.1029/2006JA011631.

Vasyliunas, V. M. (1984), Fundamentals of current description, in *Washington DC American Geophysical Union Geophysical Monograph Series, Washington DC American Geophysical Union Geophysical Monograph Series*, vol. 28, edited by T. A. Potemra, pp. 63–66, doi:10.1029/GM028p0063.

Wang, C.-P., L. R. Lyons, T. Nagai, J. M. Weygand, and R. W. McEntire (2007), Sources, transport, and distributions of plasma sheet ions and electrons and dependences on interplanetary parameters under northward interplanetary magnetic field, *Journal of Geophysical Research (Space Physics)*, *112*, A10224, doi: 10.1029/2007JA012522.

Wu, C. C. (1986), Kelvin-Helmholtz instability at the magnetopause boundary, *Journal of Geophysical Research*, *91*, 3042–3060, doi:10.1029/JA091iA03p03042.

Yamade, Y., M. Fujimoto, N. Yokokawa, and M. S. Nakamura (2000), Field-aligned currents generated in magnetotail reconnection: 3D Hall-MHD simulations, *Geophysical Research Letters*, *27*, 1091, doi:10.1029/1999GL003688.

Yong, S., and L. C. Lee (1990), Structure of the reconnection layer at the dayside magnetopause, *Planetary and Space Science*, *38*, 437–458, doi:10.1016/0032-0633(90)90109-4.

Zenitani, S., and T. Miyoshi (2011), Magnetohydrodynamic structure of a plasmoid in fast reconnection in low-beta plasmas, *Physics of Plasmas*, *18*(2), 022,105, doi:10.1063/1.3554655.